OPTIMIZATION AND APPLICATION OF STIRLING ENGINE FOR WASTE HEAT RECOVERY FROM A HEAVY-DUTY TRUCK ENGINE

by

Metin Güven

B.S., Mechanical Engineering, Boğaziçi University, 2000

M.S., Automotive Engineering, Boğaziçi University, 2006

Submitted to the Institute for Graduate Studies in
Science and Engineering in partial fulfillment of
the requirements for the degree of
Doctor of Philosophy

Graduate Program in Mechanical Engineering

Boğaziçi University

2023

OPTIMIZATION AND APPLICATION OF STIRLING ENGINE FOR WASTE HEAT RECOVERY FROM A HEAVY-DUTY TRUCK ENGINE

APPROVED BY:

DATE OF APPROVAL: 03.04.2023

ACKNOWLEDGEMENTS

First and foremost, I am extremely grateful to my supervisor, Prof. Günay Anlaş and Prof. Hasan Bedir, for their invaluable advice, continuous support, and patience during my Ph.D. study. Their immense knowledge and plentiful experience have encouraged me in all the time of my academic research. I would also like to thank Prof. Erhan Aksoylu, Assoc. Prof. Veysel Alkan, and Assist. Prof. Murat Çakan for their technical support on my study. Finally, I would like to express my gratitude to my parents, wife, and daughter. Without their tremendous understanding and encouragement over the past few years, it would be impossible for me to complete my study.

ABSTRACT

OPTIMIZATION AND APPLICATION OF STIRLING ENGINE FOR WASTE HEAT RECOVERY FROM A HEAVY-DUTY TRUCK ENGINE

In this thesis, the use of the Stirling engine for recovery of waste heat from a heavy-duty truck diesel engine is studied in detail: First, the maximum theoretical non-dimensional shaft work for three types of Stirling engines is calculated, and out from the three types are compared by optimizing selected parameters in the shaft work equation using a first-order analysis. The results show that the Beta-type Stirling engine is more effective than the Alpha and Gamma types with higher power density. Results are then used for a preliminary design of the waste heat recovery (WHR) system from the exhaust gases of a commercial truck. Calculations carried out with exhaust gas temperatures measured on-road tests show that the WHR system can provide 1% of internal combustion engine (ICE) power output, corresponding to 3 kW, offering about 0.4% reduction in fuel consumption. Second, a dynamic analysis is performed on the Beta-type engine using a second-order analysis, considering size constraints. Four Beta-type Stirling engines that use the exhaust gas recirculation (EGR) cooler or the tailpipe as a heat source are simulated. The dynamic analysis shows that the Stirling engine WHR system does not generate a reasonable power output because of the low heat transfer rate from the truck's exhaust gas. Therefore, it does not appear feasible for use in commercial vehicle applications.

ÖZET

AĞIR VASITA MOTORUNDAN ATIK ISININ GERİ KAZANIMI İÇİN STİRLİNG MOTORUNUN OPTİMİZASYONU VE UYGULAMASI

Bu tezde, ağır vasıtaların dizel motorundaki atık ısının geri kazanımı için Stirling motorunun kullanımı detaylı olarak çalışılmaktadır: İlk olarak, birinci derece analiz yöntemi kullanılarak üç tip Stirling motorunun seçilen parametreleri için maksimum teorik boyutsuz şaft işi hesaplanarak karşılaştırılmaktadır. Sonuçlar, Beta tipi Stirling motorunun daha yüksek güç yoğunluğu sayesinde, Alfa ve Gamma tiplerinden daha verimli olduğunu göstermektedir. Sonuçlar ticari aracın egzoz gazındaki atık ısının geri kazanımında kullanılacak sistemin ön tasarımında kullanılmaktadır. Yol testinde ölçülen egzoz gazı sıcaklıkları ile yapılan hesaplamalar, atık ısı geri kazanımı sisteminin içten yanmalı motorun gücünün %1'ine karşılık gelen 3 kW kadar güç çıkışı, buna bağlı olarak %0.4 kadar yakıt tüketiminde düşüş sağladığını göstermektedir. İkinci olarak, Beta tipi motoru için atık ısı geri kazanımı sisteminin dinamik analizi, ikinci derece analiz yöntemi ile, boyut kısıtlarını göz önünde bulundurarak yapılmaktadır. Egzoz gazı devridaimi soğutucusunu veya egzoz çıkış borusunu ısı kaynağı olarak kullanan, farklı dört Stirling motoru simüle edilmektedir. Dinamik analiz, kamyon egzoz gazının düşük ısı transfer oranı sebebiyle, Stirling motorlu atık ısı kazanımı sisteminin makul derecede güç üretemediğini ve ticari araç uygulamalarında kullanım için elverişli olmadığını göstermektedir.

TABLE OF CONTENTS

ACKNOWLEDGEMENTS . . . iii
ABSTRACT . . . iv
ÖZET . . . v
LIST OF FIGURES . . . viii
LIST OF TABLES . . . xi
LIST OF SYMBOLS . . . xii
LIST OF ACRONYMS/ABBREVIATIONS . . . xv
1. INTRODUCTION . . . 1
2. STIRLING ENGINE . . . 10
3. HEAVY-DUTY TRUCK ENGINE DATA . . . 12
4. SELECTION OF APPROPRIATE STIRLING ENGINE TYPE . . . 17
4.1. Indicated Work and its Non-dimensionalization . . . 17
4.2. Shaft Work and Parameters to be Optimized . . . 25
4.3. Parameter Optimization . . . 26
4.4. Comparison of Work Outputs and System Characteristics of Engines . 30
5. PARAMETRIC STUDY OF BETA-TYPE STIRLING ENGINE WITH SECOND ORDER ANALYSIS . . . 36
5.1. Layout of WHR System . . . 36
5.2. Parametrization of WHR System . . . 37
5.3. Work and Power Equations . . . 40
5.4. Governing Equations for Calculating Work Output . . . 42
5.4.1. Continuity Equation . . . 43
5.4.2. Momentum Equation . . . 44
5.4.3. Energy Equation . . . 45
5.5. Output Variables and ODE's . . . 46
5.6. Design Premises and Assumptions . . . 48
5.6.1. Preliminary Analysis . . . 51
6. APPLICATION OF THE WHR SYSTEM TO A TRUCK . . . 54
6.1. Preliminary Analysis of Beta-Type Stirling Engine for WHR System . . 54

6.2. Application of the Second Order Analysis 55
6.2.1. Stirling Engine Configurations 57
6.2.2. Performance of the WHR System 57
7. SUMMARY & CONCLUSIONS 62
REFERENCES 65
APPENDIX A: KINEMATIC ANALYSIS 71
A.1. Position Analysis of the Mechanism 71
A.2. Velocity Analysis of the Mechanism 75
A.3. Acceleration Analysis of the Mechanism 75
APPENDIX B: KINETIC ANALYSIS 77
APPENDIX C: GOVERNING EQUATIONS 80
C.1. Continuity Equation 80
C.1.1. Expansion Volume 80
C.1.2. Compression Volume 81
C.1.3. Regenerator Volume 82
C.2. Momentum Equation 83
C.2.1. Regenerator Volume 83
C.3. Energy Equation 84
C.3.1. Expansion Volume 84
C.3.2. Compression Volume 85
C.3.3. Regenerator Volume 87

LIST OF FIGURES

Figure 1.1. Total heat recovery efficiency and specific work of bottoming cycles vs. T_{max} [10]. 4

Figure 1.2. Waste heat recovery on a heavy-duty truck. 9

Figure 2.1. Types of Stirling engines. 11

Figure 3.1. Data of OM470 engine. 12

Figure 3.2. Heavy-duty truck engine layout with WHR system. 14

Figure 4.1. Definition of volume ratios. 18

Figure 4.2. Optimum Ω and κ for max. $\bar{W}_{ind}$, at $T_c/T_h = 0.3, \chi = 0.1$, (i) M1, (ii) M2. 22

Figure 4.3. Optimum Ω for max. $\bar{W}_{ind}$, at various T_c/T_h and χ, (i) M1, (ii) M2. 23

Figure 4.4. Optimum κ for max. $\bar{W}_{ind}$, at various T_c/T_h and χ, (i) M1, (ii) M2. 24

Figure 4.5. Forced work illustrated on P-V diagram. 26

Figure 4.6. Optimum Ω and Λ_{hs} vs. τ for maximum $\bar{W}_{shaft}$, ideal (dotted line) and feasible (solid line) cases. 29

Figure 4.7. Maximum $\bar{W}_{shaft}$ vs. τ at different E, ideal (dotted line) and feasible (solid line) cases. 31

Figure 4.8. W_{rat} vs. τ at various E. 32

Figure 4.9. Comparison of P-V diagrams, $E = 0.8$, $\tau = 1.76$. 35

Figure 5.1. Layout of Beta-type Stirling engine. 36

Figure 5.2. Kinematic parameters of Beta-type Stirling engine. 37

Figure 5.3. Kinematic equations. 38

Figure 5.4. Torque on the crankshaft due to pressure difference on the pistons. 41

Figure 5.5. Governing equations. 42

Figure 5.6. Continuity equations. 43

Figure 5.7. Momentum equations. 44

Figure 5.8. Energy equations. 45

Figure 5.9. Ordinary differential equations. 47

Figure 5.10. Effect of pressure and engine speed on piston torque. 50

Figure 5.11. Temperature and pressure range of working fluid. 53

Figure 5.12. Convective heat transfer coefficient, h_{cv}, for tube flow @50m/s. . . 53

Figure 6.1. Layout of the heat exchangers used in the EGR option. 56

Figure 6.2. Engine speed vs. time, the EGR option. 57

Figure 6.3. Temperature vs time, C500, the EGR option. 59

Figure 6.4. P-V diagrams. 61

Figure 6.5. Power piston torque diagrams. 61

Figure A.1. The links and the joints in the mechanism. 72

Figure A.2. The position parameters and the vectors in the vector loop equations. 72

Figure B.1. Free-body diagram of the mechanism. 77

Figure B.2. Forces in x-direction acting on the pistons. 79

LIST OF TABLES

Table 1.1. Engine energy balance [7]. 2

Table 3.1. Technical data of OM470 engine, on highway Euro VI truck. 13

Table 3.2. ICE power and exhaust gas temperature at various operation points. 16

Table 4.1. Design output for the WHR system for W_{shaft} = 112.5 J, E = $0.8, \tau = 1.76$, feasible case. 34

Table 5.1. Non-dimensional parameters. 38

Table 5.2. Torque equations. 41

Table 5.3. Preliminary analysis results. 52

Table 5.4. Hot and cold source fluid properties. 52

Table 6.1. Power output of Beta-type WHR system at various operation points. 55

Table 6.2. Specifications of the configurations. 58

Table 6.3. Output of the configurations. 60

LIST OF SYMBOLS

A	Cylinder cross-section area
$c_{..}$	Specific heat capacity
c_P	Specific heat capacity at constant pressure
c_V	Specific heat capacity at constant volume
$d_{..}$	Diameter
E	Mechanical effectiveness
$F_{..}$	Force
g	Gravitational acceleration
h_{cv}	Convective heat transfer coefficient
$I_{..}$	Moment of inertia
k	Thermal conductivity
KC_1	First kinematic constraint
KC_2	Second kinematic constraint
$L_{..}$	Length
$m_{..}$	Mass
$N_{..}$	Number of tubes
$n_{..}$	Engine speed
$\tilde{n}$	Normal vector
$P_{..}$	Pressure
$\mathcal{P}_{..}$	Power
$\dot{Q}_{..}$	Heat transfer rate
R	Gas constant
$r_{..}$	Moment arm
$T_{..}$	Temperature
$\mathcal{T}_{..}$	Torque
t	Time
t_{tube}	Tube thickness
$U_{..}$	Overall heat transfer coefficient

u_f	Flow velocity
$V_{..}$	Volume
$W_{..}$	Work output
$\dot{W}_{..}$	Work rate
$\bar{W}_{..}$	Non-dimensional work output
$x_{..}$	Displacement
$\dot{x}_{..}$	Velocity
$\ddot{x}_{..}$	Acceleration

Greek symbols

$\alpha_{..}$	Angular acceleration
$\beta_{..}$	Rod angle
η	Theoretical thermal efficiency
$\Theta_{..}$	Crank angle
$\Lambda_{..}$	Volume ratio
μ	Dynamic viscosity
ν	Kinematic viscosity
π	Pi number
$\rho_{..}$	Density
τ	Temperature ratio, T_{sh}/T_{sc}
$\phi_{..}$	Diameter ratio, $D../L_{sys}$
$\varphi_{..}$	Length ratio, $L../L_{sys}$
$\Phi_{..}$	Position ratio, $X../L_{sys}$
$\omega_{..}$	Angular velocity
Ω	Phase angle

Subscripts

amp	Amplitude
atm	Atmospheric
$aver$	Average
c	Compression control volume
cd	Compression dead control volume
cf	Interface compression and regenerator control volumes

$cool$	Cooler
cr	Crank shaft
cs	Compression swept control volume
cyl	Cylinder
d	Displacer piston
$d\#$	Displacer piston rod
$dead$	Dead control volume
fly	Flywheel
h	Expansion control volume
hd	Expansion dead control volume
$heat$	Heater
hf	Interface expansion and regenerator control volumes
hs	Expansion swept control volume
i	Initial
ind	Indicated
$mean$	Mean
ol	Overlap
p	Power piston
$p\#$	Power piston rod
r	Regenerator control volume
rat	Ratio
reg	Regenerator block
sc	Cold source
sh	Hot source
sw	Swept control volume
sys	System
tot	Total
use	Useful
x	X-direction

LIST OF ACRONYMS/ABBREVIATIONS

ATS	After-Treatment System
cs	Control Surface
cv	Control Volume
dof	Degree of Freedom
EGR	Exhaust Gas Re-circulation
ICE	Internal Combustion Engine
ODE	Ordinary Differential Equation
ORC	Organic Rankine Cycle
vol	Volume
WHR	Waste Heat Recovery

1. INTRODUCTION

The energy use in transportation has doubled in the past thirty years, and it is expected to be doubled again by the year 2050 [1]. Currently, heavy-duty trucks are used in 17% of the world's transportation [2]; emission regulations require commercial vehicle manufacturers to develop cleaner engines. As a result, engine technology has improved performance, emissions, and fuel efficiency in the past four decades [3]. However, the commercial vehicle industry still has to find ways to decrease fuel costs as demanded by the market.

Despite the expectations of a decrease in fuel consumption with the Euro VI engine introduction, challenges due to emission regulations increased fuel consumption. The new Mercedes-Benz Actros truck with Euro V engine consumes 7% less than its predecessor. For the same truck with a Euro VI engine, on the other hand, this benefit decreases to 5% [4]. Such challenges increased studies on engine downsizing and hybrid engines, vehicle aerodynamics, weight reduction, and waste heat recovery [3].

Conversely, regulations on CO_2 emissions force vehicle manufacturers to bring zero-emission vehicles on the road by 2030. Manufacturers invest in developing zero-emission technologies, such as battery and fuel-cell electric vehicles. But the range of an electric vehicle is a serious challenge in heavy-duty transportation: for example, eActros, the electric truck introduced by Mercedes-Benz in September 2022, offers a range of up to 500 kilometers with three battery packs [5]. A fuel cell truck powered by liquid or gas hydrogen is expected to reach a maximum of 1000 kilometers. A diesel truck has a range of up to 5000 kilometers. An insufficient network of battery charging stations and uncertainty about hydrogen storage, supply, and safety are the challenges to be handled. In addition, the manufacturers do not have experience maintaining and servicing new components (e.g., high-voltage components, electric motors, etc.). As a result, the internal combustion engine (ICE) will likely continue to be widely used on commercial vehicles in the next few decades.

ICEs waste approximately 60% of the fuel energy, mostly in terms of heat rejected to the environment, some of which could be recovered. Douadi et al. [6] reviewed the studies on waste heat recovery (WHR) methods, such as bottoming cycles, thermoelectric generators, and electric turbo-compounding, and concluded that the fuel economy of a compression ignition engine could be significantly improved by using innovative WHR systems.

Heat from an ICE is transferred to the surroundings through exhaust gases and cooling; Table 1.1 shows the energy balance for a typical heavy-duty diesel engine [7]. Tabulated values show that exhaust gas recirculation (EGR) and tailpipe are the most promising sources that could be used for waste heat recovery (WHR). However, several technologies can be employed to recover waste heat, and selecting an appropriate technology depends on the temperature of the heat source used.

Table 1.1. Engine energy balance [7].

Energy Flow Path	% of Total Fuel Energy	Temperature (^{o}C)
Mechanical Energy (Shaft Work)	40-42	N/A
Exhaust Energy	19-21	400
Coolant Energy	17-19	90
EGR Cooler Energy	10-12	540
Charge Air Cooler Energy	8-10	170
Other (Radiant)	1-3	varies

Temperatures of EGR flow and exhaust gases of a heavy-duty truck are in the range of 200-500 ^{o}C; according to Paanu et al. [8], Rankine, Brayton (Joule) and Stirling cycles are the most compatible bottoming cycles in this temperature range. There is an increasing interest in the use of Rankine cycles [9]. Bianchi and De Pascale [10] compared the efficiency and specific work outputs of Organic Rankine (ORC), Stirling, and Inverted Brayton cycles. WHR efficiency and specific work output plots in Figure 1.1 show that ORC performs the best when low-temperature heat sources

are used, the critical factor being the organic fluid used. Each organic fluid has a maximum performance only in a limited temperature range. For example, benzene has a maximum efficiency of only 300-350 ^{o}C. Therefore, using an ORC to recover heat from an ICE with a wide source-temperature range is unsuitable.

A Stirling cycle's efficiency and specific work output change is significantly less than ORC for a given temperature range, which is an advantage for a wide temperature range WHR system. The simplicity of a WHR system is another important factor for heavy-duty truck applications; a successful WHR application should not add complexity to the truck's maintenance. Temperature protection of working fluid and lubricant in the ORC system is another challenging issue. The typical working fluid ethanol decomposition temperature is above 300 ^{o}C, and lubricant is above 250 ^{o}C. A Stirling engine is also advantageous from this point of view because it does not require components such as a turbine and pump, which add more maintenance. Stirling engine's simplicity and compact design, high thermal efficiency, similar performance for a broad range of hot source temperatures, and silent operation are why it is proposed as a valuable alternative to ORC for a WHR system on a vehicle. Cullen and McGovern [11] investigated the feasibility of utilizing a Stirling cycle engine as an exhaust gas waste heat recovery device for an Otto cycle internal combustion engine (ICE). They claimed that it was feasible in principle to generate approximately a further 30% useful power in addition to that created by the ICE by using a Stirling cycle engine to capture waste heat expelled from the ICE exhaust gases over the complete range of engine operating speeds. Liu et al. [12] evaluated the Stirling engine in a vehicle-mounted exhaust heat recovery system with an ideal adiabatic analysis. As a result, they increased the system's efficiency by about 59%, optimizing their design's heater, cooler, and regenerator units. Alfarawi et al. [13] developed a Beta-type Stirling engine for passenger cars by CFD investigation. They claimed that from a hot source with 850 K and a cold source with 450 K, it is possible to generate a power output of 1.5-2 kW at an ideal thermal efficiency of 40% and engine overall weight of 11-14 kg.

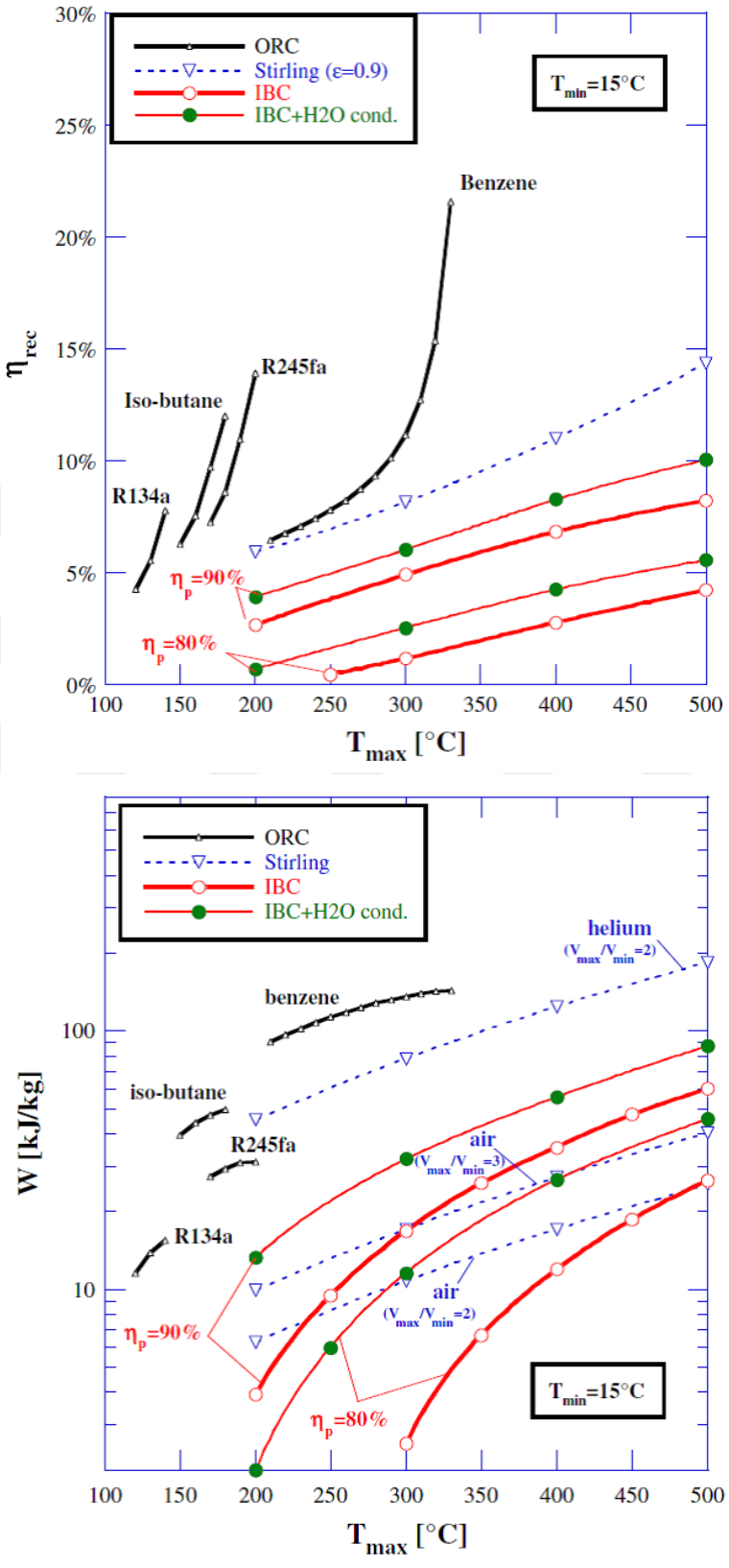


Figure 1.1. Total heat recovery efficiency and specific work of bottoming cycles vs. T_{max} [10].

Catapano et al. [14] worked on a two-cylinder Gamma-type Stirling engine for WHR from the exhaust gas of a small ICE (16 kW) experimentally and numerically. Under full load conditions of the ICE and at an exhaust gas temperature of about 830 K, they calculated a maximum output of 350 W, corresponding to roughly 2% of the power generated by the ICE. In their study, the engines operated in a laboratory environment without any constraint on the size of the heat exchangers.

Theoretical models for analyzing the Stirling engine are divided into first-, second- and third-order models [15, 16]. First-order design models, for which Schmidt theory is widely used, are more suitable for preliminary system analysis and to predict a machine's power output and efficiency only by the heater and cooler temperatures, the engine displacement, and the speed. Derivation of indicated work by Schmidt theory was explained by Hirata [17] for three types of engines. Second-order design models are used to estimate the power output and heat input using various identifiable loss terms and heat losses. Third-order design models compute the complex processes of a Stirling engine, considering all losses. Computational fluid dynamic simulations are examples of this model. Optimization of the Stirling engine has been studied analytically and with numerical simulations in several papers. Senft [18] applied Schmidt theory for the optimization of engine parameters for Gamma-type engines. Cheng & Yang [19] extended the study of Senft for all three types of engines. Bert et al. [20] validated a zero-dimensional finite-time thermodynamic model with experimental data of a Gamma-type engine, to use the model for optimizing the kinematic of a Stirling engine. Toghyani et al. performed multi-objective optimization on GPU-3 Stirling engine, a Beta-type engine developed by General Motors, firstly with second-order analysis [21], and then with third-order analysis [22]. They chose four decision variables: the temperature of the heat source, stroke, mean effective pressure, and the engine frequency to increase the efficiency and output power and reduce the pressure drop. CAE analysis of Hiang et al. [23] on Alpha-type engines shows that phase angle is a significant geometrical parameter affecting Stirling engines' performance. Araoz et al. [24] analyzed a Gamma-type engine with a second-order model, to integrate the thermodynamics and the thermal and mechanical interactions that influence the engine

performance of kinematic Stirling engines. The study of Ni et al. [25] provides a comprehensive understanding of the influence mechanism of rotary speed, pressure, and working gas (helium and nitrogen) in the view of heat/power losses for Beta-type engine performance. According to their study, maximum shaft power can be achieved with helium. Alfarawi et al. [26] investigated the effect of phase angle, gas type, regenerator matrix type, and dead volume on a Gamma-type engine's performance by reconfiguring non-ideal adiabatic analysis and validated against experimental measurements. They also presented the feasibility of utilizing liquid nitrogen to maximize the shaft power. Li et al. [27] performed an analysis based on the finite speed thermodynamics and isothermal methods for irreversible processes in solar-powered Gamma-type Stirling engines to highlight the impact of losses on provided mechanical power and its performance. Ahmadi et al. [28] conducted a finite speed thermodynamic analysis study for the GPU-3 Stirling engine. The effects of heat source temperature, regenerating effectiveness, volume ratio, piston stroke as well as rotational speed are included in the analysis. In addition, they calculated maximum output power at the optimal rotational speed, which was calculated considering pressure losses in the Stirling engine. Almajri et al. [29] carried out a parametric study with a CFD model, to investigate the effects of various design parameters and operating conditions such as regenerator porosity, charge pressure, matrix wire diameter, dead volume, and hot/cold ends temperatures on Alpha-type engine. Xiao et al. [30] presented a CFD analysis of Beta-type. Stirling engine. The geometric parameters of heat exchangers, including heater and cooler tube diameters and lengths, regenerator size, matrix mesh, and wire diameter, were considered to maximize thermal efficiency, output power, and minimize flow resistance power loss in the Stirling engine. In addition, they achieved an increase of 2% in thermal efficiency by reducing dead volumes in the system. Shendage et al. [31] presented a second-order cyclic analysis for investigating the effect of the overlapping volume displaced by the piston and displacer within the cylinder. Abuelyamen et al. [32] performed a parametric study on a Beta-type engine with three parameters; initial charge pressure, thermal boundary condition, and three different types of working fluids (air, He, and H2). The results include comparing the amount of heat transfer, power output, and thermal efficiency. It was found that the best engine performance is achieved

when H2 gas is used as the working fluid. Moreover, results revealed that power output and efficiency were maximized at different charge pressure values. Cheng & Chen [33] studied the influence of the variables, including charged pressure, heating temperature, regenerator porosity, engine rotation speed, number of heating pipes, and working fluid on the power output of a Beta-type engine. Cheng & Yang [34] presented the importance of pressure drops and mechanical loss in a Beta-type engine and modified the non-ideal adiabatic theoretical model. They claimed that with their modified model verified with performance measurements, the shaft power was found to be predicted accurately. Aksoy et al. [35] analyzed a Beta-type engine for different heater temperatures and system pressure, and they obtained optimum system input for their design within the given range. Cinar et al. [36] performed a similar analysis to Aksoy's [35] for an Alpha-type engine. Additionally, they analyzed the effect of the working fluid by comparing air and helium.

The optimization studies mentioned above were done for a specific engine type. Kirkley [37] and Walker [38] investigated three types of Stirling engines by comparing the indicated work and presented optimum values of parameters on design charts. To obtain higher indicated work, Walker [38] presented an optimal combination of phase angle and swept volume ratio. In both of the studies, they have taken the indicated work W_{ind} as the target work output to be maximized. However, Senft [39, 40] claimed that maximum W_{ind} does not ensure maximum shaft work W_{shaft}, as W_{shaft} is not a simple multiple of W_{ind}. Senft [39] derived an equation for W_{shaft} by considering mechanism effectiveness and investigated optimum parameters for maximizing W_{shaft} for Gamma-type Stirling engines with a non-dimensional method [18]. Cheng and Yang [19] extended the work of Senft to Alpha and Beta type Stirling engines with a new non-dimensional method to predict optimum values of the parameters more accurately. Their study became a basis for other studies on the optimization of Beta-type Stirling engine [41, 42]. However, using mRT, as suggested by Cheng and Yang, may result in inconsistency since some of the parametric terms in the work equation are eliminated during non-dimensionalization; this will be explained in Section 4.1.

This thesis presents the analysis for a WHR system with a Stirling engine on a heavy-duty diesel engine (Figure 1.2). In Chapter 2, the working principle and the types of Stirling engine is described. In Chapter 3, the heavy-duty diesel engine data and the layout are given with two possible assembly options for the WHR system. In Chapter 4, the maximum theoretical shaft work per unit volume is investigated using first-order analysis for three Stirling engine types, Alpha, Beta, and Gamma, to identify the most suitable engine type. The theoretical shaft work per unit volume is maximized by optimizing parameters in the work equation with a new non-dimensionalization method. The sizing of three types of Stirling engines is performed for a target of 3 kW mechanical power output, using the optimum parameters values for corresponding commercial truck engine data. According to the first-order analysis results, the Beta-type Stirling engine is the best choice for the WHR system. In Chapter 5, the second-order analysis (transient analysis) of the Beta-type Stirling engine is performed. The system's power output is obtained by calculating heat transfer from the exhaust gas and the cooling water in the heat exchangers. The governing equations with non-dimensional parameters are listed for calculating work and power outputs, and the design premises are defined. In Chapter 6, the performance of the WHR system is evaluated by comparing the power outputs of different Stirling engine configurations. The efficiency and the power output obtained with the second-order analysis are substantially lower than the first-order analysis.

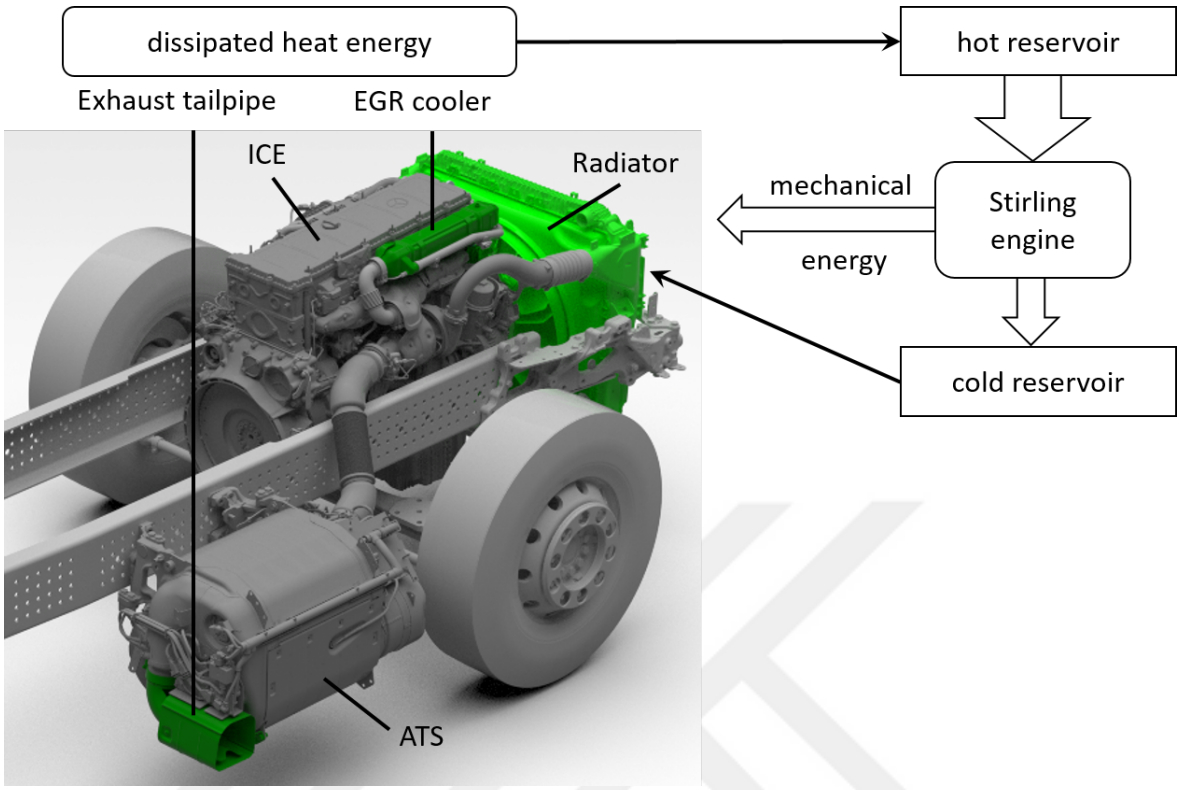


Figure 1.2. Waste heat recovery on a heavy-duty truck.

2. STIRLING ENGINE

A Stirling engine is a heat engine that operates in a closed cycle between two heat reservoirs. Wang et al. [43] reviewed four types of Stirling engines, kinetic, thermoacoustic, free-piston, and liquid piston types, for heat recovery. They concluded that kinetic and thermoacoustic Stirling engines are the most advantageous regarding the power scale, conversion efficiency, and costs. Due to the well-known technology and capability of coupling conversion devices for either mechanical or electric energy, there is a high interest in kinetic Stirling engines. The engine consists of three main parts: the hot volume, the cold volume, and the regenerator. A gaseous working fluid (mostly air) moves between the hot and the cold volumes during expansion and compression. Heat is transferred to the working fluid through a heat exchanger in the hot volume. Heated working fluid expands and pushes the power piston. The regenerator, which has a porous structure, absorbs some of the heat of the working fluid during expansion as the gas moves from the hot volume to the cold volume. The power piston moves in the opposite direction during compression, and the working fluid is compressed. While passing toward the hot volume, the cooled working fluid absorbs the stored heat in the regenerator. The power and the displacer pistons move with a phase difference determined by the crank mechanism. The hot and cold volumes consist of two sub-volumes. The region where the pistons move is called swept volume, and the clearance of the cylinders and tubes between cylinders is called dead volume. Figure 2.1 shows these sub-volumes in a Stirling engine.

The location of the hot and cold volumes determines the engine type. Figure 2.1 shows three main Stirling engine types. Alpha-type has two separate cylinders for the hot and cold volumes. In a Beta-type engine, the hot and cold volumes are located in one cylinder and separated by a displacer. The displacer is connected to the crank mechanism to support the working fluid transfer between the hot and cold volumes. Gamma-type engine, which is similar to Beta-type, has a cold volume and compression piston in a shifted cylinder.

The theoretical thermal efficiency of a Stirling cycle is the same as that of the Carnot cycle and is given as $\eta = 1 - T_c \,/\, T_h$.

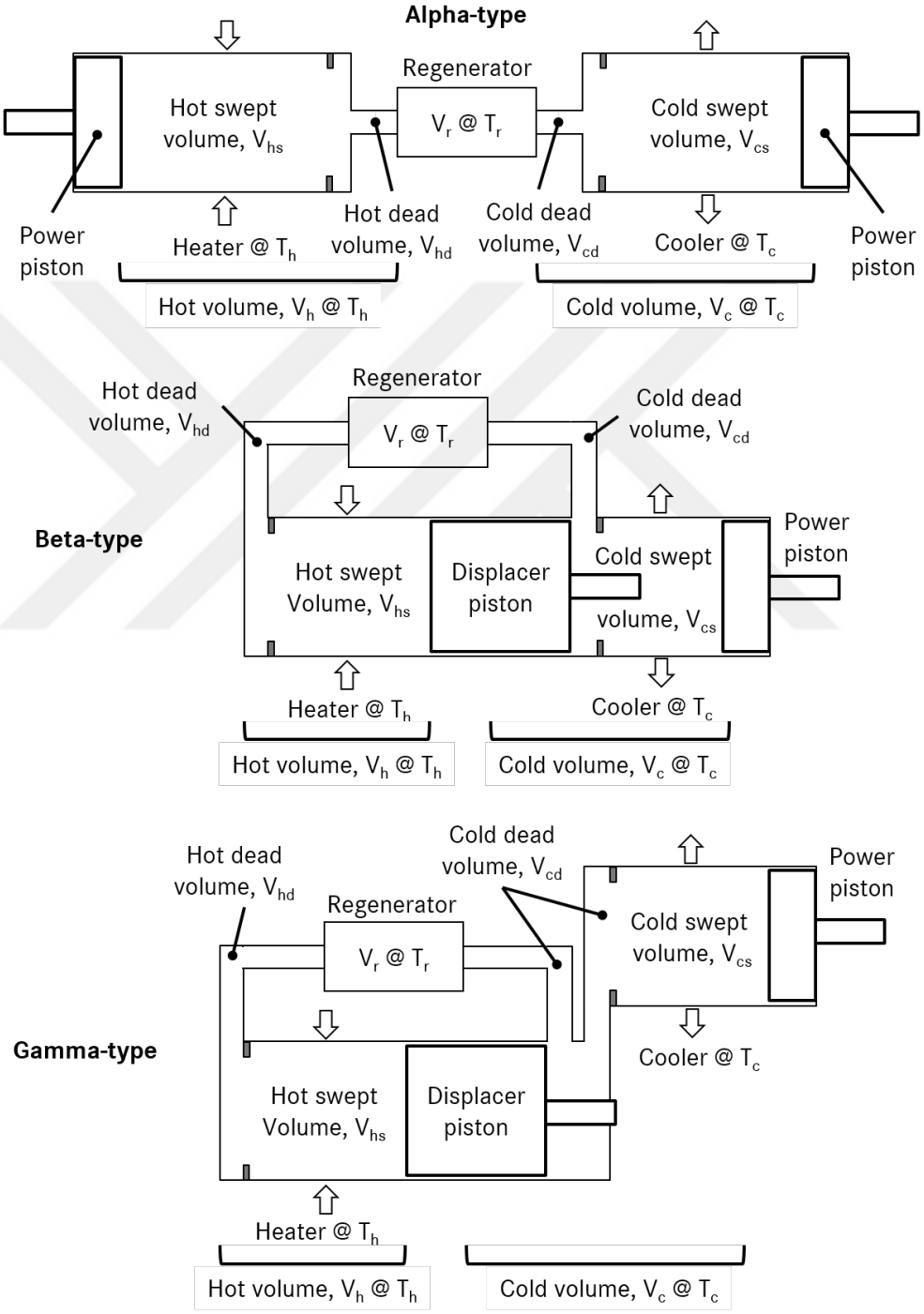


Figure 2.1. Types of Stirling engines.

3. HEAVY-DUTY TRUCK ENGINE DATA

Application of WHR system is investigated for a typical on-road tractor, Mercedes-Benz Actros with OM470 engine, the data of which is given in Figure 3.1 and Table 3.1.

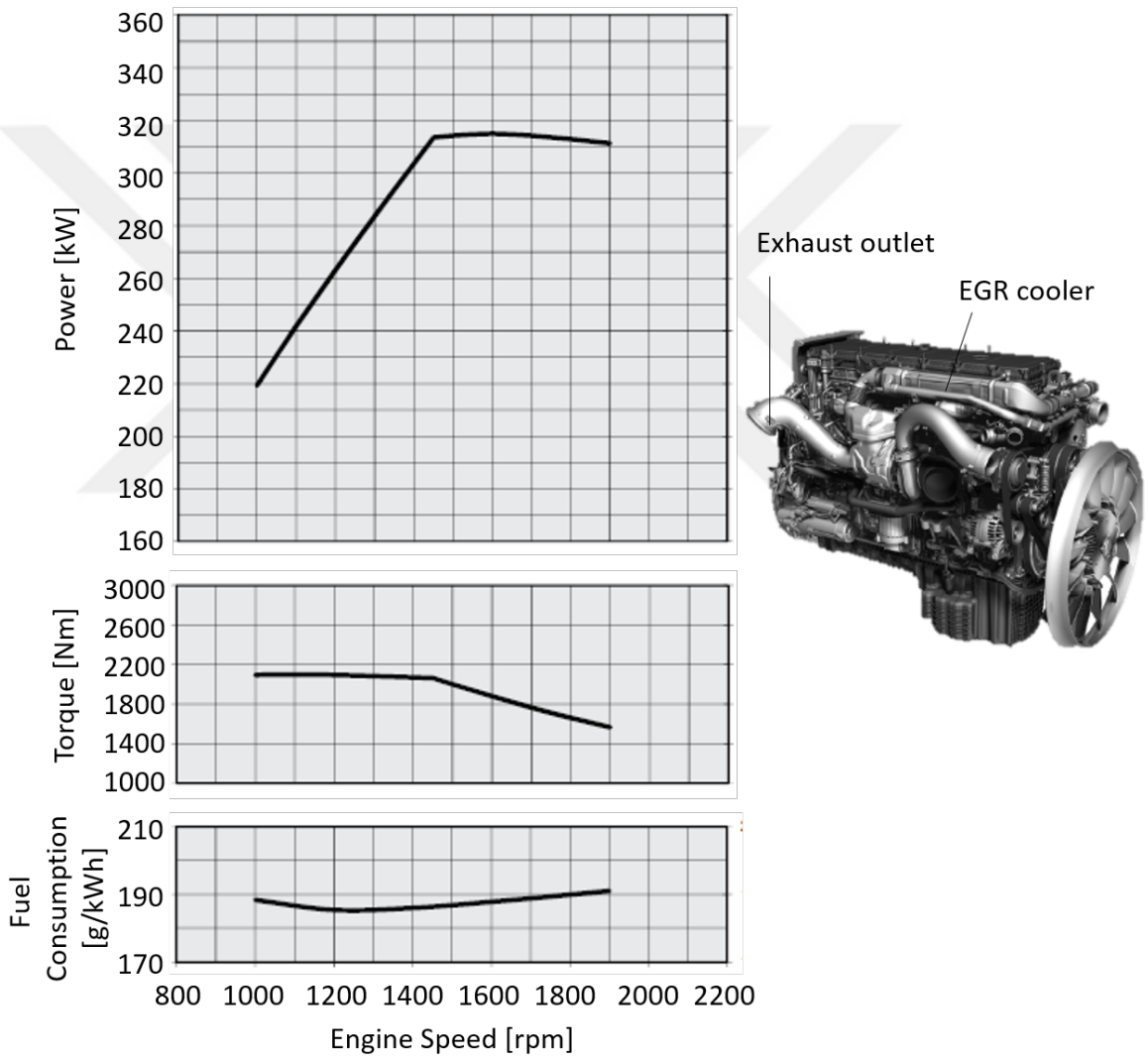


Figure 3.1. Data of OM470 engine.

Table 3.1. Technical data of OM470 engine, on highway Euro VI truck.

General Data	
No. of Cylinders	6
Displacement	10700 cm^3
Bore/Stroke	125 mm/145 mm
Compression ratio	18.5
Power, Torque	
Rated Power at Engine Speed 1600 rpm	315 kW
Torque, max. from Engine Speed 1100 rpm	2100 Nm
Mean Effective Pressure, at Maximum Torque / at Rated Power	2471 kPa / 2208 kPa
Engine Speed, Low Idle Speed, Standard / Maximum no Load Speed	500 rpm / 2260 rpm
Engine Speed, Lowest Speed for Continuous Operating	1000 rpm
Coolant System	
Heat Rejection, at Rated Power	156 kW
Coolant Temperature, max.	383 K
Temperature Difference between Engine Inlet and Outlet, max.	282 K
Charge Air System	
Charge Air Pressure (Overpr., stat.) after Turbocharger, at Rated Power	230 kPa
Pressure Drop Charge Air System at Rated Power, max.	9.5 kPa
Charge Air Temperature after Turbocharger, at Rated Power / maximum	468 K / 473 K
Heat Rejection at Rated Power, min.	55 kW
Fuel System	
Fuel Consumption (Diesel Fuel), at Rated Power	187 g/kWh
Fuel Consumption (Diesel Fuel), at Full Load, min.	185 g/kWh
Exhaust System	
Exhaust Gas Mass / Volume, at Rated Power	365 g/s / 39 m^3/min
Exhaust Gas Temperature, at Rated Power / maximum	673 K / 843 K
Exhaust Back Pressure (stat.), at Rated Power	10 kPa
Engine Brake	
Brake Power, at max. Permissible Brake Speed, Standard	270 kW
Brake Power, at max. Permissible Brake Speed, High Performance	325 kW
Drag Power at max. Permissible Brake Speed	53 kW
Brake Speed max. Permissible	2300 rpm

Heat sources on the heavy-duty truck are illustrated in Figure 3.2, with temperature range and thermal power. According to the data, three primary waste heat sources are engine coolant, charge air, and exhaust gas. Among these sources, the engine coolant's thermal power is high, but the source temperature is low. Likewise, charge air has a moderate source temperature, but its thermal power is also low. Finally, the exhaust gas's thermal power and source temperature are high. As a result, exhaust gas is chosen as the source of waste heat in this application. Two possible positions of the WHR system are highlighted in Figure 3.2.

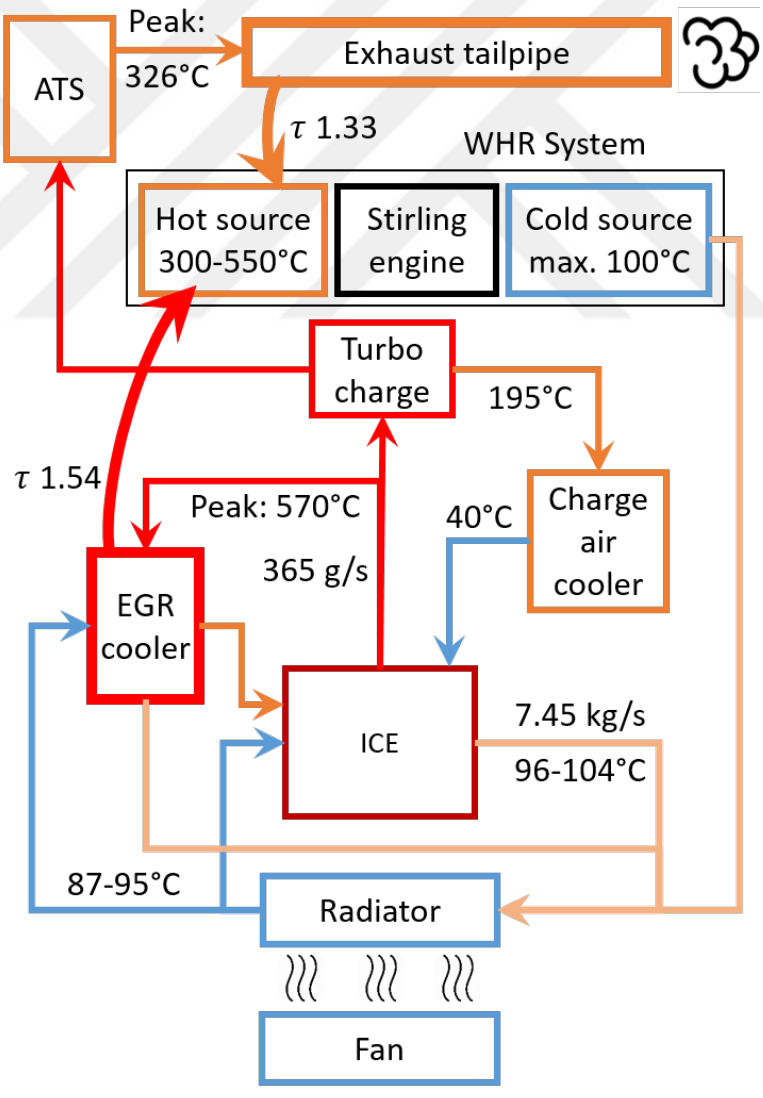


Figure 3.2. Heavy-duty truck engine layout with WHR system.

The first option is placing the WHR system close to the exhaust gas recirculation (EGR) system, where a higher exhaust gas temperature is reached. The exhaust gas can be cooled in two steps. The first step is absorbing the heat by the WHR system, which can be located instead of the current EGR cooler. The second step is cooling the exhaust gas to its target temperature with a smaller cooler between the WHR system and the ICE inlet. Using current exhaust and cooling lines with adaptation is an essential advantage of this option. About 30 % of exhaust gas is directed to the EGR system, corresponding to a mass rate of 0.11 kg/s. Assuming the temperature difference between the exhaust gas inlet and outlet, $\Delta T_{exhaust}$ to be at most 100 K, the possible heat rate from the exhaust gas is 12.6 kW. That means this is the maximum heat input for the Stirling engine. On the cooler side, less than 5 % of cooling water (total mass rate 7.45 kg/s) is sufficient for removing excess heat from the working fluid. The first option's temperature ratio, τ, can be derived from ICE data, given for rated power. At rated power, τ is calculated as 1.54 due to outlet temperatures of 573 K for the exhaust gas and 373 K for the cooling water (average value from Figure 3.2). The theoretical thermal efficiency of the case at rated power is 35 %. At maximum outlet temperatures of 743 K for the exhaust gas and 383 K for the cooling water, the limit for τ is 1.94.

The second option is to place the system close to the tailpipe not to disturb the after-treatment system's function (ATS). During the road test of an equipped truck on a highway, the exhaust gas temperature range was measured as 529-599 K (Table 3.2). The weighted average of this temperature range is calculated to be 567 K. Furthermore, on a bench test that simulates the worst case for a long ride up to a mountain, the exhaust gas temperature reaches 705 K. Despite the moderate temperature level, a disadvantage of this option is the necessity of an additional cooling system or extension of the existing ICE cooling lines. About 70 % of exhaust gas is thrown out through the tailpipe, corresponding to a mass rate of 0.26 kg/s. Assuming the temperature difference between exhaust gas inlet and outlet, $\Delta T_{exhaust}$ to be at most 70 K, the maximum heat input for this option is 20.5 kW. With the average outlet temperature of 373 K for the cooling water, the temperature ratio τ is 1.33, and the theoretical thermal efficiency is 25 %.

Table 3.2. ICE power and exhaust gas temperature at various operation points.

Operation Point (OP)	Road Measurements					Bench Test
	1	2	3	4	5	
Weighting of OP	18%	6%	16%	38%	22%	-
ICE Torque [Nm]	900	400	1400	1900	1900	1600
ICE rpm [U/min]	1300	1300	1300	1300	1600	1900
ICE Power [kW]	122.5	54.5	190.6	258.7	318.3	318.3
Exhaust Temp. [K]	529	552	557	573	599	705

4. SELECTION OF APPROPRIATE STIRLING ENGINE TYPE

In this chapter, first-order analysis with the Schmidt method [17] is carried out to compare the work output of Alpha, Beta, and Gamma-type engines. Engine parameters are optimized with a new non-dimensionalization approach to the work equation. In section 4.1, the indicated work equation is derived for each Stirling engine type. Two methods for defining non-dimensional work are presented, and the work equation is non-dimensionalized. The shaft work equation is derived in section 4.2, and its parameters are defined. Parameters are optimized in section 4.3, and the comparisons of work outputs and system characteristics of Alpha, Beta, and Gamma type engines are given in section 4.4.

4.1. Indicated Work and its Non-dimensionalization

The Schmidt method assumes that the working fluid is an ideal gas. The cycle comprises isothermal expansion, compression, and isobaric heat exchange processes. The pressure is uniform in the engine, and hot and cold-swept volumes change sinusoidally. The hot and cold dead volumes are at temperatures T_h and T_c, respectively, with a perfect regeneration process. The indicated work of a Stirling cycle is given as:

$$W_{ind} = \oint P \, dV \ . \tag{4.1}$$

The total volume, V_{tot}, is a function of the crank angle θ and the phase angle Ω, and is the sum of the hot (V_h), the cold (V_c), and the regenerator (V_r) volumes:

$$V_{tot}(\theta, \Omega) = V_h(\theta) + V_c(\theta, \Omega) + V_r \ . \tag{4.2}$$

The hot and cold volumes consist of swept (V_{hs} and V_{cs}) and dead (V_{hd} and V_{cd}) volumes. The dead volumes are constant during the cycle, with swept volumes varying with the movement of the crank mechanism. The cold cylinder piston follows the hot cylinder piston with a phase angle difference Ω. The hot and cold volume equations are written for the position of the hot cylinder piston as follows:

$$V_h(\theta) = V_{hs}(\theta) + V_{hd} \ , \tag{4.3}$$

$$V_c(\theta, \Omega) = V_{cs}(\theta, \Omega) + V_{cd} \ . \tag{4.4}$$

The volume ratios defined in Figure 4.1 are used in the analysis. The overlap volume, V_{ol}, is nonzero only for the Beta-type.

$$\Lambda_{sw} = V_{sw} \ / \ V_{tot}$$

$$\Lambda_{dead} = V_{dead} \ / \ (V_{sw} - V_{ol})$$

$$\Lambda_r = V_r \ / \ (V_{sw} - V_{ol})$$

$$\Lambda_{hs} = V_{hs} \ / \ V_{sw}$$

$$\Lambda_{cs} = 1 - \Lambda_{hs} = V_{cs} \ / \ V_{sw}$$

$$\Lambda_{hd} = V_{hd} \ / \ V_{dead}$$

$$\Lambda_{cd} = 1 - \Lambda_{hd} = V_{cd} \ / \ V_{dead}$$

$$\Lambda_{ol} = V_{ol} \ / \ V_{sw} = 0.5 - \left[\frac{\Lambda_{hs}^2 - \Lambda_{hs}}{2} (1 + cos\Omega) + 0.25 \right]^{1/2}$$

Figure 4.1. Definition of volume ratios.

The hot and cold volumes are written in terms of the total volume V_{tot}, and the volume ratios are as follows;

$$V_h = V_{tot}\ \Lambda_{sw} \left[\frac{1 - cos(\theta)}{2}\ \Lambda_{hs} + \Lambda_{dead}\ \Lambda_{hd} \right] , \tag{4.5}$$

$$V_{c,Alpha} = V_{tot}\ \Lambda_{sw} \left[\frac{1 - cos(\theta - \Omega)}{2}\ (1 - \Lambda_{hs}) + \Lambda_{dead}\ (1 - \Lambda_{hd}) \right] , \tag{4.6}$$

$$\begin{aligned} V_{c,Beta} = {} & V_{tot}\ \Lambda_{sw} \left[\frac{1 - cos(\theta - \Omega)}{2}\ (1 - \Lambda_{hs}) + \frac{1 + cos\theta}{2}\ \Lambda_{hs} \right] \\ & + V_{tot}\ \Lambda_{sw}\ [\ \Lambda_{dead}\ (1 - \Lambda_{hd}) - R_{vol}\ ] , \end{aligned} \tag{4.7}$$

$$\begin{aligned} V_{c,Gamma} = {} & V_{tot}\ \Lambda_{sw} \left[\frac{1 - cos(\theta - \Omega)}{2}\ (1 - \Lambda_{hs}) + \frac{1 + cos\theta}{2}\ \Lambda_{hs} \right] \\ & + V_{tot}\ \Lambda_{sw}\ \Lambda_{dead}\ (1 - \Lambda_{hd}) \ . \end{aligned} \tag{4.8}$$

The work equation (Equation 4.1) can be rewritten in the following form;

$$W_{ind} = \int_0^{2\pi} P\ \frac{\partial V}{\partial \theta}\ d\theta \, , \tag{4.9}$$

where,

$$\left(\frac{\partial V}{\partial \theta} \right)_{Alpha} = V_{tot}\ \Lambda_{sw} \left[\frac{\sin\theta}{2}\ \Lambda_{hs} + \frac{\sin(\theta - \Omega)}{2} (1 - \Lambda_{hs}) \right] , \tag{4.10}$$

$$\left(\frac{\partial V}{\partial \theta} \right)_{Beta} = \left(\frac{\partial V}{\partial \theta} \right)_{Gamma} = V_{tot}\ \Lambda_{sw}\ \frac{\sin(\theta - \Omega)}{2} (1 - \Lambda_{hs}) \, . \tag{4.11}$$

Pressure P is obtained from the ideal gas equation. Evaluating the integral in Equation 4.9, W_{ind} is obtained as follows;

$$W_{ind} = P_{mean}\ V_{tot}\ \pi\ (\tau - 1)(\Lambda_{hs} - \Lambda_{hs}^2)\ \Lambda_{sw}\ G\ \sin\Omega \, , \tag{4.12}$$

where, $G = (S - \sqrt{S^2 - H})/H$. The terms S and H for each engine type are;

$$
\begin{aligned}
S_{Alpha} &= (\Lambda_{hs} + 2\ \Lambda_{dead}\ \Lambda_{hd})(1-\tau) + \tau(1 + 2\Lambda_{dead}) + \frac{2\tau \ln(\tau)}{\tau - 1}\Lambda_r\ , \\
H_{Alpha} &= (\Lambda_{hs}^2 + 2\tau(\Lambda_{hs} - \Lambda_{hs}^2)\ cos\Omega + \tau^2(1-\Lambda_{hs})^2\ , \\
S_{Beta} &= \Lambda_{hs} + \tau + \left[2\Lambda_{dead}\ \Lambda_{hd}(1-\tau) + 2\tau\ \Lambda_{dead} + \frac{2\tau \ln(\tau)}{\tau - 1}\Lambda_r\right](1 - \Lambda_{ol}) - 2\tau\ \Lambda_{ol}\ , \\
H_{Beta} &= 2\tau\ \Lambda_{hs}(\tau\Lambda_{hs} - \Lambda_{hs} - \tau)(1 + cos\Omega) + \Lambda_{hs}^2 + \tau^2 + 2\tau\ \Lambda_{hs}\ cos\Omega\ , \\
S_{Gamma} &= \Lambda_{hs} + \tau + 2\Lambda_{dead}\ \Lambda_{hd}(1-\tau) + 2\tau\ \Lambda_{dead} + \frac{2\tau \ln(\tau)}{\tau - 1}\Lambda_r\ , \\
H_{Gamma} &= 2\tau\ \Lambda_{hs}(\tau\Lambda_{hs} - \Lambda_{hs} - \tau)(1 + cos\Omega) + \Lambda_{hs}^2 + \tau^2 + 2\tau\ \Lambda_{hs}\ cos\Omega\ .
\end{aligned}
$$

In the studies of Senft [18] and Cheng and Yang [19], parameters' optimum values are calculated from a non-dimensional work equation. To non-dimensionalize, Senft [18] divides the work equation by $P_{mean}V_{hs}$. However, using sub-volumes may result in omitting some geometrical parameters from the work equation. For example, when hot swept volume V_{hs} is chosen, the non-dimensional work becomes directly proportional to swept volume ratio $\kappa = V_{cs}/V_{hs}$ [18]. This proportionality means that the maximum non-dimensional indicated work is obtained when $\kappa \to \infty$; therefore, no optimum value for κ can be found. Cheng and Yang used mRT_h to non-dimensionalize instead of $P_{mean}V_{hs}$, and their choice yields another ambiguity. To better understand the shortcomings of both Senft and Cheng and Yang's, two different non-dimensionalizations, namely division by $P_{mean}V_{tot}$ in Method 1 ($M1$), and by mRT_h in Method 2 ($M2$) are proposed as shown below:

$$(M1): \qquad \bar{W}_{ind} = \frac{\oint P\ dV}{P_{mean}\ V_{tot}}\ , \tag{4.13}$$

$$(M2): \qquad \bar{W}_{ind} = \frac{\oint P\ dV}{m\ R\ T_h}\ . \tag{4.14}$$

$M1$ and $M2$ are used to determine optimum parameter values for maximum work output. Results are compared to those of Senft [18] and Cheng and Yang [19]. Figure 4.2 shows how $\bar{W}_i$ changes as a function of phase angle Ω and swept volume ratio κ. The figures are plotted using $M1$ and $M2$ with temperature ratio $T_c/T_h = 0.3$, and volume ratio $\chi = 0.1$ employed by Cheng and Yang for all three engine types, where χ is the ratio V_{dead}/V_{hs} [18]. Optimum Ω and κ values that maximize $\bar{W}_{ind}$ are shown on the plots. For Alpha-type, optimum κ values are close, but there is a significant difference in the optimum Ω values. For the Beta-type, the difference between optimum κ values becomes larger; the difference between optimum Ω values is also significant, and optimum Ω for $M2$ is close to 0^o. For the Gamma-type, the difference between optimum κ values is the largest; optimum κ calculated using $M2$ is about 3.

When $M1$ is used, the Beta-type has the most considerable work output, $\bar{W}_{ind}$, and the Gamma-type has the smallest. Results of $M2$ give the same value for Alpha and Beta types under given conditions. Again, the Gamma type has the lowest value, like in the case of $M1$, but this time the difference between Gamma and other types is more significant.

In Figure 4.3, the optimum phase angle Ω range is given for various temperature ratios T_c/T_h and dead volume ratios χ. The optimum Ω range using $M1$ for all three types is smaller than that calculated using $M2$, especially for Alpha and Beta types. The curves for $\chi = 0$ represent the ideal case, in which the dead volume and regenerator volume are taken as zero. Perfect regeneration and no loss at the ideal case result in the highest theoretical work output for a specified temperature ratio. $\bar{W}_{ind}$ and W_{ind} calculated with the optimum values of $M1$ in Figure 4.3, for the ideal case, is more significant than any other case, as expected. $\bar{W}_{ind}$ calculated with the optimum values of $M2$, for the ideal case, is also higher than any other case. However, the corresponding dimensional work W_{ind} is almost zero. Such a misleading result means optimum Ω values obtained with $M2$ are inaccurate. In Figure 4.4, the optimum swept volume ratio κ range is given for various temperature ratios T_c/T_h and dead volume ratios χ. As shown in Figure 4.3, the optimum κ range using $M1$ for all three types is smaller than the ones calculated using $M2$. The optimum κ values reach 6 with $M2$, for Alpha

and Beta types and 8 for Gamma-type at low-temperature ratios. These values are much higher than Stirling engine applications, where κ is taken close to 1 [41].

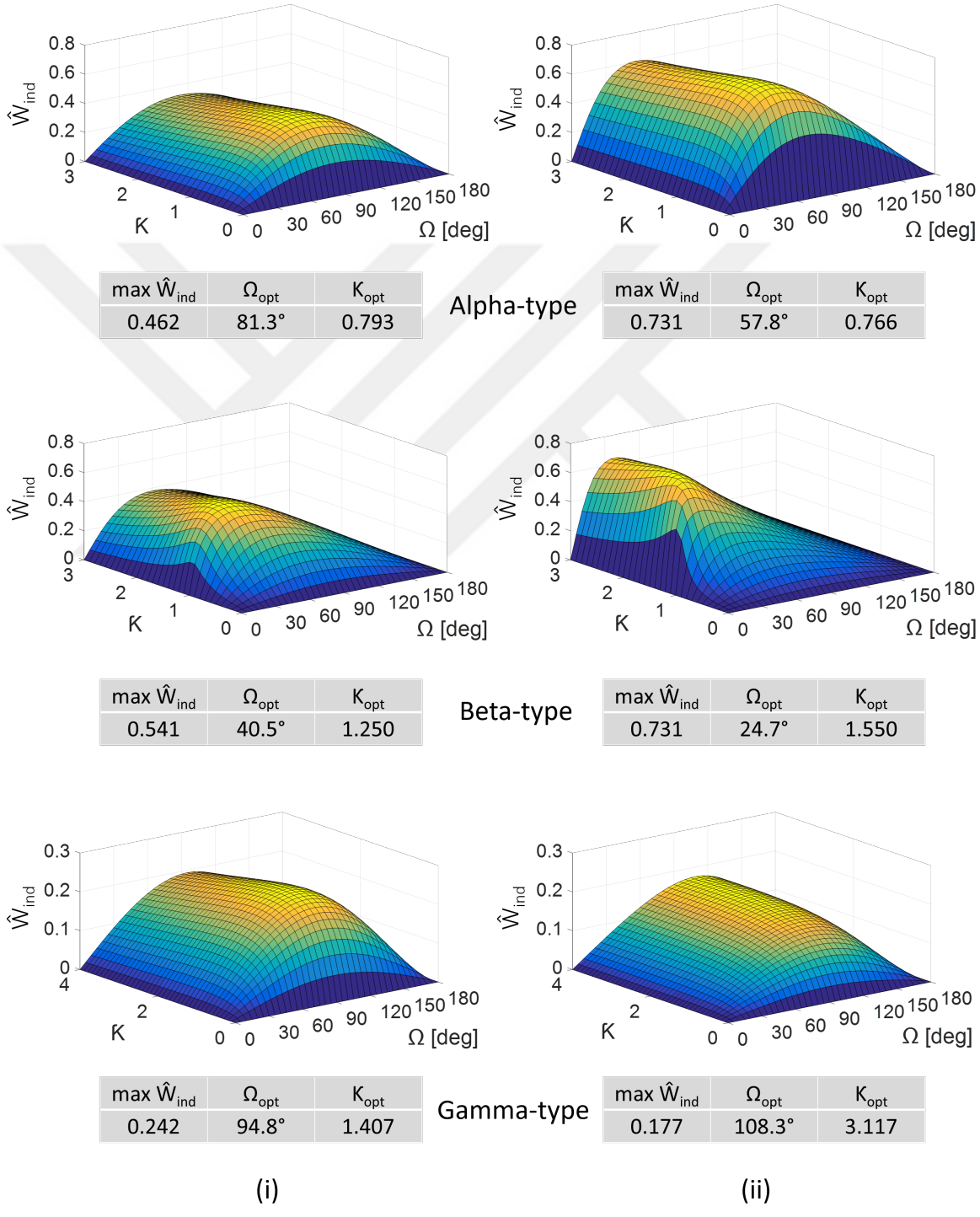


Figure 4.2. Optimum Ω and κ for max. $\bar{W}_{ind}$, at $T_c/T_h = 0.3, \chi = 0.1$, (i) M1, (ii) M2.

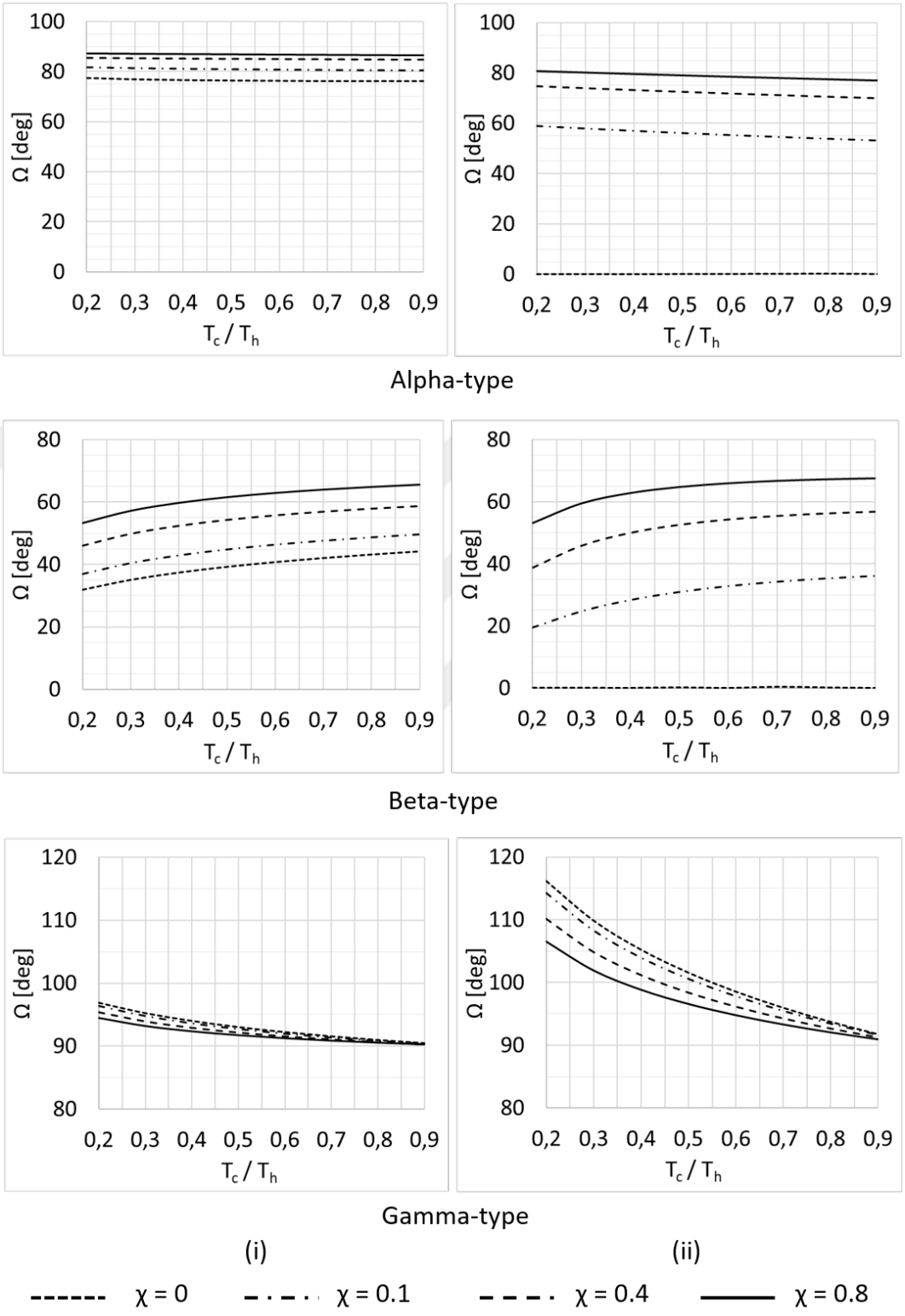


Figure 4.3. Optimum Ω for max. $\bar{W}_{ind}$, at various T_c/T_h and χ, (i) M1, (ii) M2.

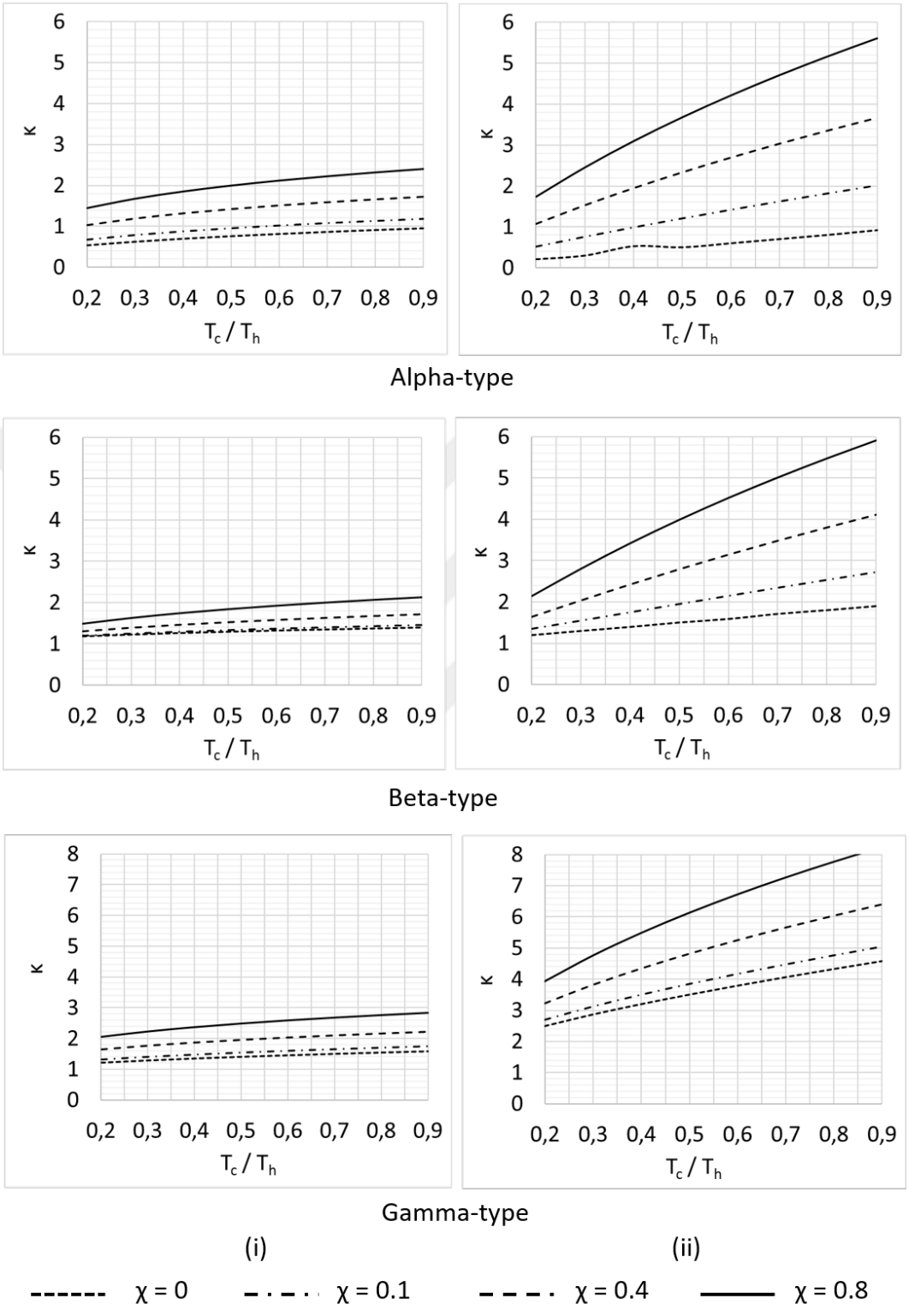


Figure 4.4. Optimum κ for max. $\bar{W}_{ind}$, at various T_c/T_h and χ, (i) M1, (ii) M2.

As the WHR system works with varying hot source temperatures, it would be more appropriate to use P_{mean} and total volume, V_{tot} as design inputs instead of m and T_h (mechanical design and packaging limit the total volume and system pressure for an application to a commercial truck). Therefore, in this thesis, $M1$, Equation 4.13, is chosen, and the non-dimensional indicated work is written as shown below:

$$\frac{W_{ind}}{P_{mean}\, V_{tot}} = \pi\, (\tau - 1)(\Lambda_{hs} - \Lambda_{hs}^2)\, \Lambda_{sw}\, G\, \sin\Omega\,. \tag{4.15}$$

4.2. Shaft Work and Parameters to be Optimized

Senft [18] found that the shaft work, W_{shaft}, is not defined only by the mechanism's characteristics but also by the shape of the cycle and the external or buffer space pressure. He derived an equation for W_{shaft} as given below by considering a constant mechanism effectiveness E $(0 \leq E \leq 1)$:

$$\bar{W}_{shaft} = E\, \bar{W}_{ind} - \left(\frac{1}{E} - E\right) \frac{W_{forced}}{P_{mean}\, V_{tot}}\,. \tag{4.16}$$

W_{forced} is the forced work due to buffer pressure, which corresponds to the shaded area on the P-V diagram (Figure 4.5), and is given by,

$$W_{forced} = \frac{1}{2}\left(\oint |(P - P_{mean} dV)| - W_{ind}\right). \tag{4.17}$$

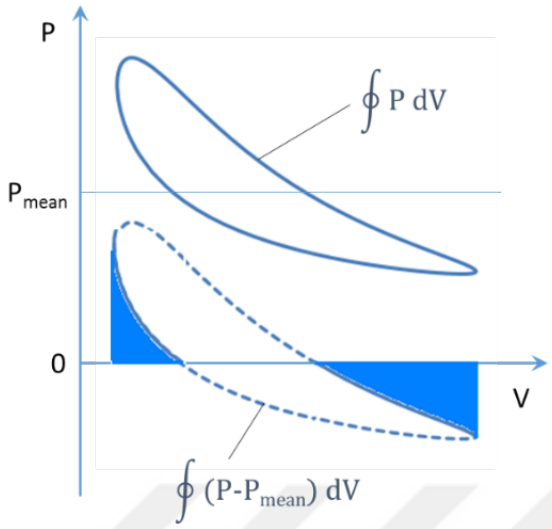


Figure 4.5. Forced work illustrated on P-V diagram.

4.3. Parameter Optimization

This section uses the Lagrange multipliers technique to evaluate Stirling engine types by comparing their maximum theoretical non-dimensional shaft work. The parameter ranges are defined as inequality constraints. The set of equations of an optimization problem is given below, and the minimization tool of Matlab *fmincon* is used in the calculations;

$$L = \bar{W}_{shaft} + \sum_{i=1}^{9} \lambda_i \left(g_i + s_i^2\right) , \tag{4.18}$$

where g_i terms are given as follows;

$$g_1 = \tau - 1 , \qquad g_2 = \Lambda_{dead} , \qquad g_3 = \Lambda_r ,$$
$$g_4 = \Omega , \qquad g_5 = \pi - \Omega , \qquad g_6 = \Lambda_{hs} ,$$
$$g_7 = 1 - \Lambda_{hs} , \qquad g_8 = \Lambda_{hd} , \qquad g_9 = 1 - \Lambda_{hd} .$$

As the Stirling engine works with a temperature difference, parameter τ should be greater than one without an upper bound. Lower bounds of the dead (Λ_{dead}) and regenerator (Λ_r) volume ratios are zero, which means there is no dead or regenerator volume in the engine. In the other extreme case, where the system consists of only dead or regenerator volume (without any swept volume), the ratios Λ_{dead} and Λ_r become infinity. The lower bounds for the ratio of hot swept volume to swept volume (Λ_{hs}) and hot dead volume to dead volume (Λ_{hd}) are zero, and the upper bounds for both are one. The phase angle (Ω) changes between 0 and π. Inspection of Equation 4.18 shows that the higher the temperature difference is, the more work generated. Although a system without dead and regenerator volumes yields the highest work output (optimum values of Λ_{dead} and Λ_r are zero), such a system is impossible. The optimum value calculated for Λ_{hd} is 1, which means the dead volume on the cold side is zero. Since zero cold dead volume is not achievable realistically, this result is interpreted as the regenerator should be put as close as possible to the cold source.

The optimum values for Λ_{hs} and Ω are investigated for two cases: the ideal and the feasible cases. In the ideal case, the dead and the regenerator volumes are zero. On the other hand, in the feasible case, the ratios of the dead and the regenerator volumes to the swept volume are arbitrarily defined to be 0.2. Therefore, the effect of Λ_{hd} on the non-dimensional work output is negligible compared to the other dead volume ratios. So Λ_{hd} is taken to be 0.5, which means cold and hot dead volumes are equal in the following analyses. Although the maximum hot source temperature of engine WHR is around 500 ^{o}C, the upper limit for hot temperature is 1000 ^{o}C. The cold source temperature is taken as the ambient temperature. As a result, the range of τ in the calculations is defined between 1 and 5.

The optimum values of Ω and Λ_{hs} for maximum $\bar{W}_{shaft}$, corresponding to the ideal (dashed line) and the feasible (solid line) cases vs. τ are shown in Figure 4.6. These optimum values are obtained by maximizing Equation 4.16 for a range of mechanism effectiveness E between 0.7 and 1. For any values of Λ_{dead} and Λ_r between 0 and 0.2, the optimum values of Ω and Λ_{hs} lay between the dashed and solid lines. For $E = 1$, shaft work is equal to indicated work. The optimum value of phase angle Ω for Alpha,

Beta, and Gamma types are between 76-88^o, 32-53^o, and 90-97^o, respectively. The Beta-type optimum phase angle is affected the most by changes in τ while that of the Alpha-type is affected the least. The optimum values of Λ_{hs} for the Beta and Gamma types are less sensitive to τ than those of the Alpha type. Also, they are less sensitive to changes in Λ_{dead} and Λ_r for $\tau > 3$. When the cold swept volume is larger than the hot one, the maximum $\bar{W}_{shaft}$ can be obtained for the Beta and Gamma types. Λ_{hs} range for these types is close to each other; for the Beta between 0.42-0.48, and the Gamma between 0.39-0.47. For the Alpha-type, the hot-swept volume should be larger than the cold-swept volume, and the range should be 0.51-0.65. For $E < 1$, the optimum phase angle Ω distribution of Alpha and Beta types is completely different from the $E = 1$ case. For example, while the optimum Ω of Alpha-type is less than 90^o for $E = 1$, it exceeds 90^o for the given E range. Also, optimum Ω does not change significantly for the whole range of τ for $E = 1$, but optimum Ω increases significantly for $\tau < 2$. Beta-type shows the same behavior for the low-temperature range. For $\tau > 2$, optimum Ω of Beta-type is in the range of 30-50^o for both cases and all E values. The optimum Ω distribution for Gamma-type shows behavior similar to the $E = 1$ case. However, the optimum values for $E < 1$ are mostly less than 90^o, while for $E = 1$, they are more than 90^o. Swept volume ratio Λ_{hs} curves in Figure 4.6 show the distribution of Λ_{hs} is entirely different from the $E = 1$ case for Beta and Gamma types, while Alpha-type has similar behavior. While the optimum Λ_{hs} at $E = 1$ case for Beta and Gamma types is less than 0.5, it exceeds 0.5 as the E value decreases. A value higher than 0.5 means maximum $\bar{W}_{shaft}$ can be obtained with a larger hot swept volume than a cold one. The increase in Λ_{hs} is significant for $\tau < 2$. For Alpha-type, change in optimum Λ_{hs} value as E decreases can be considered constant. In all cases, maximum $\bar{W}_{shaft}$ can be obtained with a larger hot swept volume than a cold one for Alpha-type.

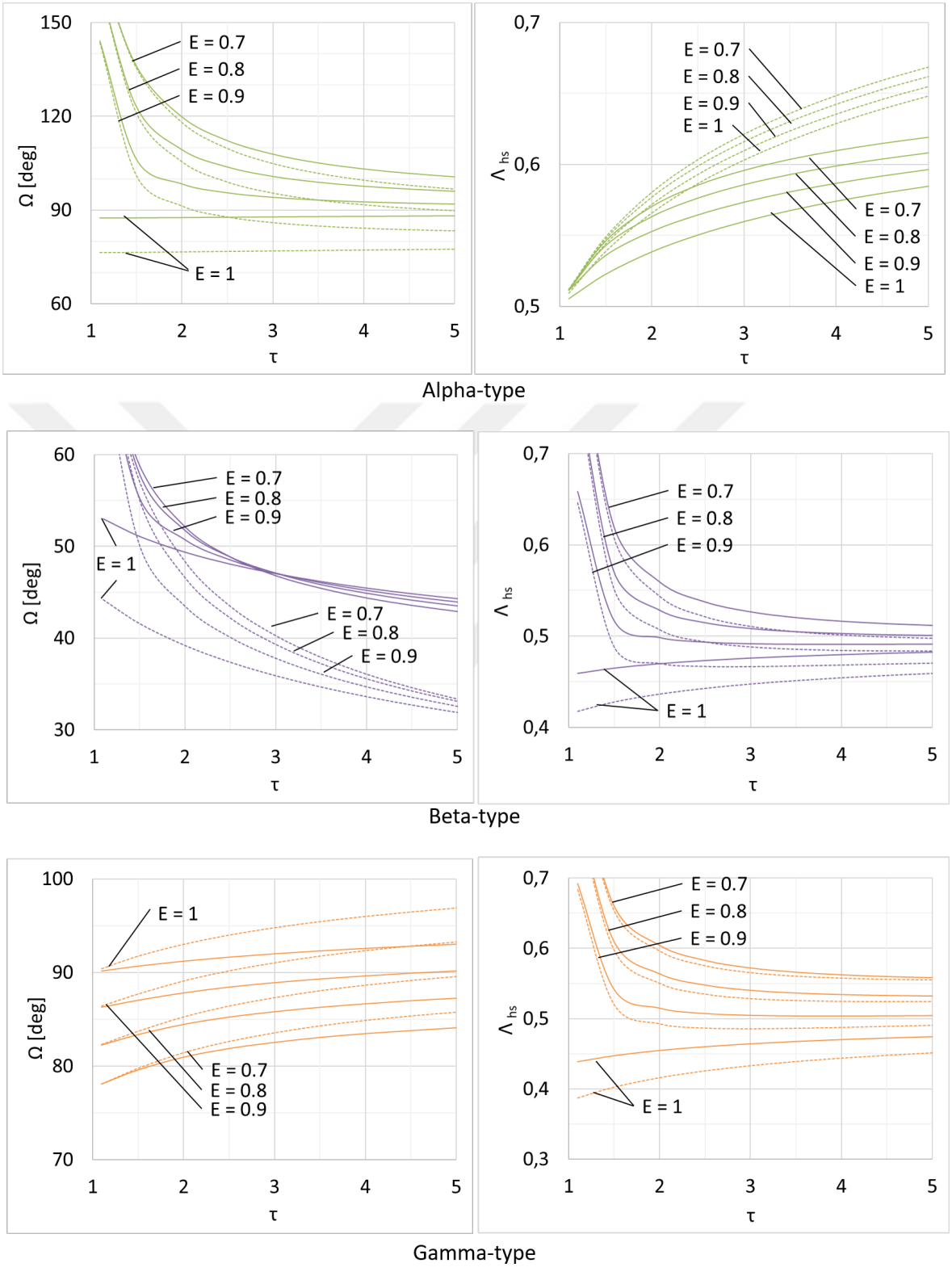


Figure 4.6. Optimum Ω and Λ_{hs} vs. τ for maximum $\bar{W}_{shaft}$, ideal (dotted line) and feasible (solid line) cases.

4.4. Comparison of Work Outputs and System Characteristics of Engines

Maximum theoretical $\bar{W}_{shaft}$ and corresponding $\bar{W}_{ind}$ and $\bar{W}_{forced}$ are calculated using optimum phase angles and swept volume ratios. For all engine types at different E, $\bar{W}_{ind}$ is not sensitive to changes in optimum parameters, particularly for the feasible case. $\bar{W}_{forced}$ does not alter for all types when $\tau > 2$. Lower E values lead to lower $\bar{W}_{forced}$ within the system. For $E < 1$, the Alpha-type has the highest $\bar{W}_{forced}$, and the Gamma-type has the lowest.

In Figure 4.7, $\bar{W}_{shaft}$ is plotted as a function of τ at different E for the ideal and the feasible cases. In the ideal case, E strongly affects $\bar{W}_{shaft}$. In the feasible case, since $\bar{W}_{ind}$ and $\bar{W}_{forced}$ are less affected by E, the effect of E becomes less dominant. The comparison of $\bar{W}_{shaft}$ shows that the Beta-type has the highest $\bar{W}_{shaft}$, while the Gamma-type has the lowest. $\bar{W}_{shaft}$ of the Beta-type is about 34% greater than the Alpha-type for $\tau = 5$ at the feasible case. With decreasing τ, the difference increases to 120% for $E = 0.7$. $\bar{W}_{shaft}$ of the Beta-type is about 110% higher than the Gamma-type for $\tau = 5$ at the feasible case. With decreasing τ, the difference decreases to 23% for $E = 0.7$. The advantage of the Beta-type comes from its overlap volume. Overlap volume increases the swept volume ratio, Λ_{sw}, to about 1.5 in the ideal case (which is 1.0 for the other types) and to about 1.0 in the feasible case (which is 0.7 for the other types). The work ratio W_{rat} is defined as W_{shaft}/W_{ind}. Senft [18] called W_{rat} as the mechanical efficiency of the cycle. Figure 4.8a compares W_{rat} for all engine types at different E values and the feasible case. The mechanical efficiency of Beta and Gamma types are close to each other. For $\tau < 2$, the efficiency of the Beta-type is slightly higher than the Gamma-type. The Alpha-type has the lowest efficiency up to $\tau = 3.5$. However, after this point, the efficiency reaches the level of the Gamma type. Figure 4.8b shows the mechanical efficiency of the Beta-type for the ideal and the feasible cases. The efficiency of the ideal case is lower than the feasible case, which is also true for the other engine types. However, the average difference is only 3% for Alpha and Beta types and 1% for the Gamma-type. There is only a negligible difference between the mechanical efficiency of the ideal and the feasible cases. Therefore, the mechanical efficiency of the ideal case can be taken as the basis for design.

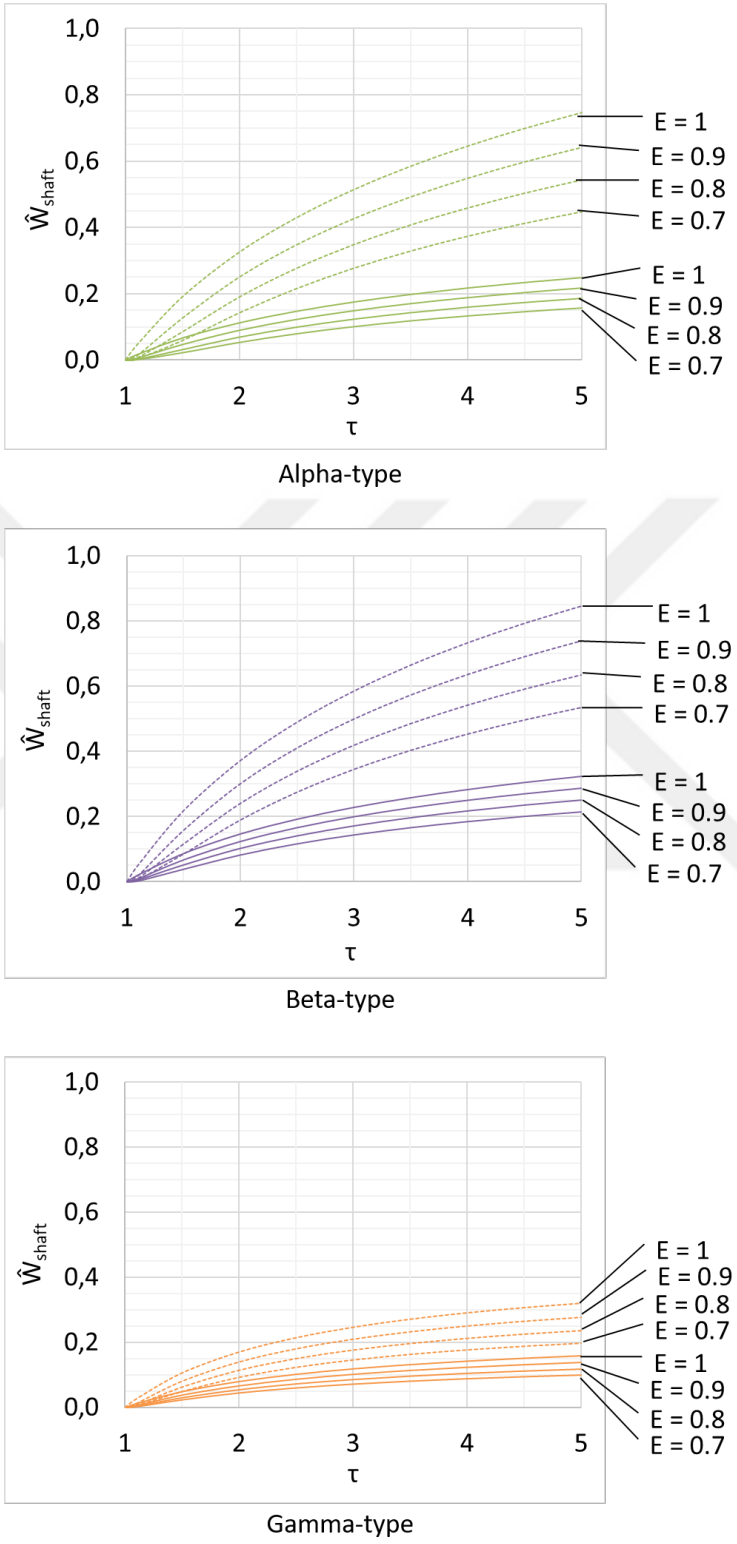
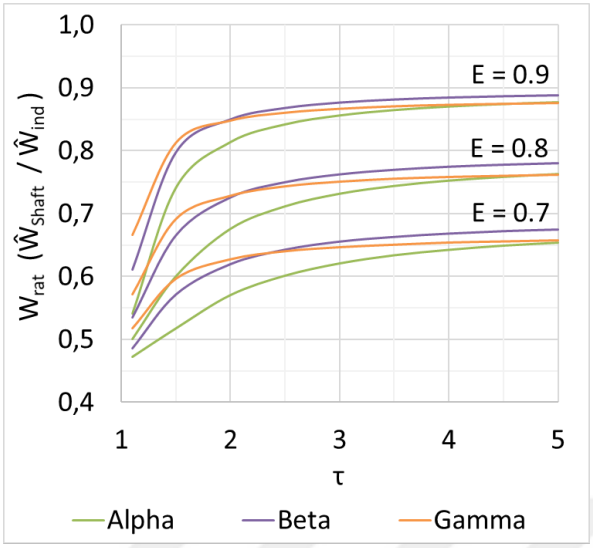
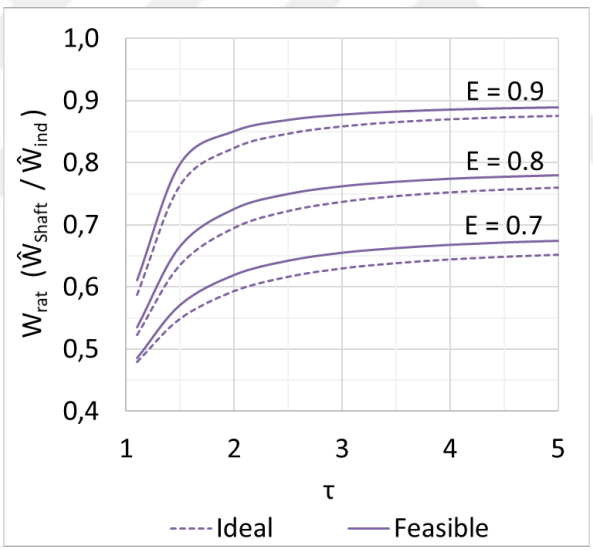


Figure 4.7. Maximum $\bar{W}_{shaft}$ vs. τ at different E, ideal (dotted line) and feasible (solid line) cases.



All types, feasible case



Beta-type, ideal and feasible cases

Figure 4.8. W_{rat} vs. τ at various E.

The ratio of maximum pressure (P_{max}) to P_{mean} is given as,

$$\frac{P_{max}}{P_{mean}} = \sqrt{\frac{S+\sqrt{H}}{S-\sqrt{H}}} = \frac{P_{mean}}{P_{min}}\,, \tag{4.19}$$

moreover, the ratio of P_{max} to P_{min} in the cycle is defined as follows,

$$P_{rat} = \frac{P_{max}}{P_{min}} = \left(\frac{P_{max}}{P_{mean}}\right)^2 = \frac{S+\sqrt{H}}{S-\sqrt{H}}\,. \tag{4.20}$$

Calculations show that the Alpha-type has the highest pressure ratio P_{rat}, while the Gamma-type has the smallest. Therefore especially for the Alpha-type, high pressures could cause durability and sealing problems. For the feasible case and the studied τ range, an average P_{rat} of 2.5 is found for the Alpha and the Beta types and 2.2 for the Gamma type. The decrease in P_{rat} by reducing mechanism effectiveness is significant in the ideal case, which explains the reduction of $\bar{W}_{shaft}$. In the feasible case, P_{rat} decreases at an average of 10% for the Alpha-type and about 7% for Beta and Gamma types for each decrease of E by 0.1.

The volume of the WHR system is important for diesel engine applications because there is a severe limitation in the packaging of engine parts. To achieve the same work output using the same P_{mean}, the least volume is needed in the case of the Beta-type. Furthermore, the Beta-type is the most suitable Stirling engine for WHR application due to its highest non-dimensional work output and moderate pressure ratio. The Alpha-type is the second suitable one; although the non-dimensional work is closer to the Beta-type, larger total volume and higher pressure ratio are its disadvantages. The Gamma-type has significantly lower non-dimensional work and needs greater volume, which means that the Gamma-type would not be feasible for a WHR system on a truck.

Stirling engine configurations are created (Alpha, Beta, and Gamma) with optimum parameters for the feasible case with $\tau = 1.76$ and mechanical effectiveness $E = 0.8$. For the given temperature ratio, the theoretical efficiency is 0.43. In the design process, the working fluid is selected as helium and P_{mean} as 405 kPa. The Stirling engine operation speed is 1600 rpm, close to the ICE's operation speed at the rated power. A 3 kW power output at this operation speed corresponds to a shaft work of W_{shaft}=112.5 J for the cycle. Using the optimum values from Figure 4.6 for the operating temperature ratio and the given engine data, the sizes of the three types of engines are determined, and the results are tabulated for $E = 0.8$ in Table 4.1.

Table 4.1. Design output for the WHR system for $W_{shaft} = 112.5$ J, $E = 0.8, \tau = 1.76$, feasible case.

Design output	Alpha-type	Beta-type	Gamma-type
Phase angle Ω [deg]	114.3	54.1	84.0
Swept volume ratio Λ_{hs}	0.555	0.542	0.580
Total volume V_{tot} [cm^3]	5294	3525	6369
Swept volume V_{sw} [cm^3]	3781	3448	4549
Hot swept volume V_{hs} [cm^3]	2097	1870	2637
Cold swept volume V_{cs} [cm^3]	1684	1578	1912
Overlap volume V_{ol} [cm^3]	-	930	-
Volume ratio V_{max}/V_{min}	1.88	1.81	1.43
Min. pressure P_{min} [kPa]	293.8	295.6	317.4
Max. pressure P_{max} [kPa]	558.7	555.1	517.1
Pressure ratio P_{rat}	1.90	1.88	1.63
Mass of working fluid $m_{tot}[g]$	1.49	1.21	2.59
Indicated work W_{ind} [J]	174	159.8	157.8
Forced work W_{forced} [J]	59.4	34.1	30.5
Work ratio W_{rat}	0.65	0.70	0.71

The smallest engine which meets the target output is the Beta-type engine with a total volume of 3525 cm^3. The Alpha-type engine needs a total volume of 5294 cm^3, while the Gamma-type engine needs 6369 cm^3. Maximum pressure in the system is about 560 kPa for Alpha and Beta types and 517 kPa for Gamma-type (P_{mean} = 405 kPa). Alpha-type has the highest forced work, W_{forced}, which results in the lowest work ratio, W_{rat}, of 65%. For Beta and Gamma types, W_{rat} is calculated as 70% and 71%, respectively. Figure 4.9 compares P-V diagrams for each engine type. All engines are sized to give the same shaft work in a cycle.

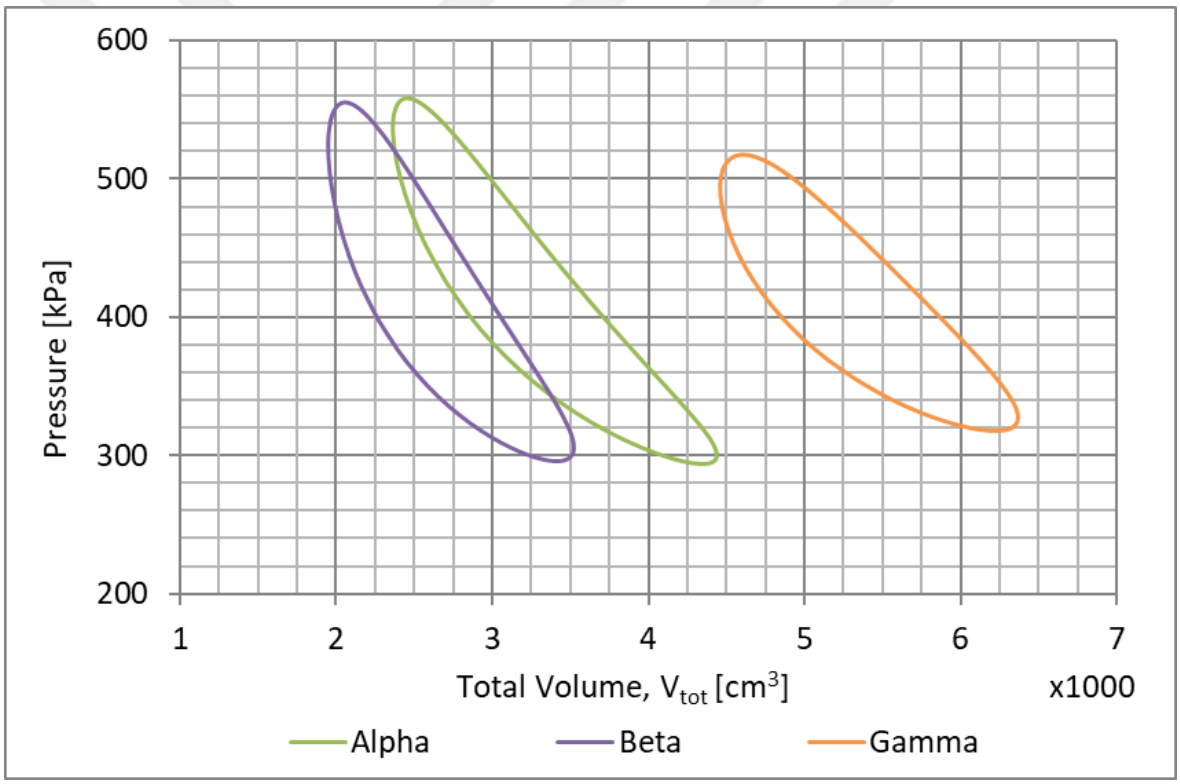


Figure 4.9. Comparison of P-V diagrams, $E = 0.8$, $\tau = 1.76$.

5. PARAMETRIC STUDY OF BETA-TYPE STIRLING ENGINE WITH SECOND ORDER ANALYSIS

First-order analysis of the WHR system shows Beta-type Stirling engine is the right choice. This chapter presents the parameters and governing equations used for the second-order analysis (transient analysis) to estimate power output within specified packaging constraints.

5.1. Layout of WHR System

Second-order analysis needs time-dependent calculation of the system characteristics, which requires considering the crank mechanism for calculating the system's heating and cooling performance and the pistons' inertial effects. In Figure 5.1, the layout of the WHR system is shown with the addition of piston rods to the control volumes, analyzed in the previous chapter.

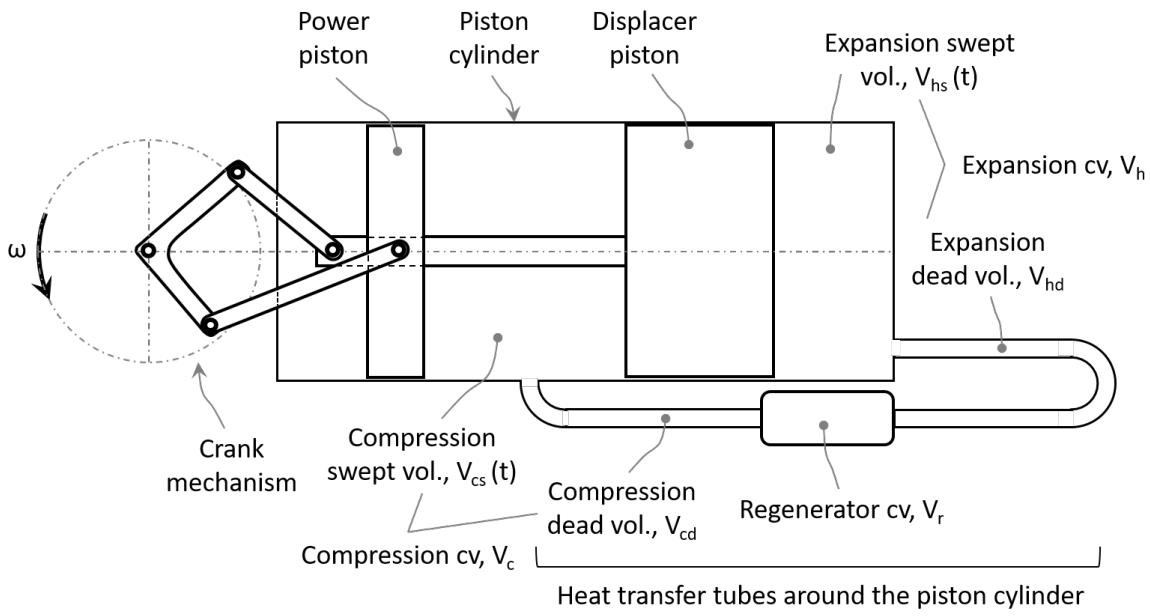


Figure 5.1. Layout of Beta-type Stirling engine.

5.2. Parametrization of WHR System

Kinematic parameters of the WHR system are shown in Figure 5.2, in terms of the length of the control volumes and the piston rods and the thickness and position of the pistons. Kinematic analysis of the mechanism is presented in Appendix A. The equations for the system length, L_{sys}, displacement of the power and the displacer pistons, x_p, x_d, and the size of the cylinder volume, L_{cyl}, and the swept volumes, L_{hs}, L_{cs}, are given in Figure 5.3, with the definition of the piston rod angles. The position equations, x_p, and x_d, are derived in Appendix A.1.

Kinematic constraints should also be defined to avoid collisions between the pistons and their rods. The power piston should move between joints of the extension rod of the displacer piston. This movement can be satisfied by following constraints:

$$KC_1 = \frac{x_d - L_{d3} - L_d}{x_p - L_p} \,, \tag{5.1}$$

$$KC_2 = \frac{x_p}{x_d - L_d} \,. \tag{5.2}$$

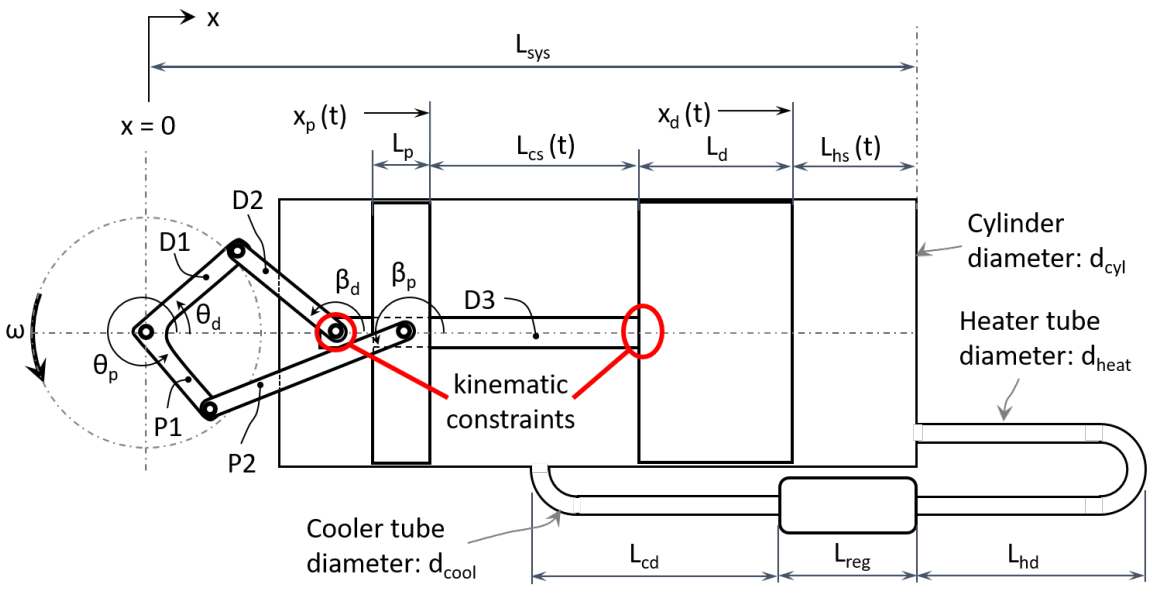


Figure 5.2. Kinematic parameters of Beta-type Stirling engine.

$$
\begin{aligned}
L_{sys} &= L_{d1} + L_{d2} + L_{d3} + L_d \\
x_p(t) &= L_{p1}\ \cos\theta_p - L_{p2}\ \cos\beta_p + L_p/2 \\
x_d(t) &= L_{d1}\ \cos\theta_d - L_{d2}\ \cos\beta_d + L_{d3} + L_d \\
L_{cyl}(t) &= L_{sys} - x_p(t) \\
L_{hs}(t) &= L_{sys} - x_d(t) \\
L_{cs}(t) &= x_d(t) - x_p(t) - L_d \\
L_{cd} &= L_{sys} - (L_{p1} + L_{p2} + L_p/2 + L_{reg}) \\
\theta_p(t) &= \omega_{cr}\, t \ \ , \ \ 0 \le \theta_p \le 2\pi \\
\theta_d(t) &= \theta_p + \Omega \ \ , \ \ 0 < \Omega < \pi \\
\beta_p(t) &= \arcsin(L_{p1}/L_{p2}\ \sin\theta_p) \ \ , \ \ \pi/2 < \beta_p < 3\pi/2 \\
\beta_d(t) &= \arcsin(L_{d1}/L_{d2}\ \sin\theta_d) \ \ , \ \ \pi/2 < \beta_d < 3\pi/2
\end{aligned}
$$

Figure 5.3. Kinematic equations.

Table 5.1. Non-dimensional parameters.

Power piston rod length	$\varphi_{p1} = L_{p1}/L_{sys}\ ,\ \varphi_{p2} = L_{p2}/L_{sys}$
Displacer piston rod length	$\varphi_{d1} = L_{d1}/L_{sys}\ ,\ \varphi_{d2} = L_{d2}/L_{sys}\ ,\ \varphi_{d3} = L_{d3}/L_{sys}$
Piston position	$\Phi_p = x_p/L_{sys}\ \ ,\ \ \Phi_d = x_d/L_{sys}$
Expansion vol. length	$\varphi_{hs} = L_{hs}/L_{sys}\ \ ,\ \ \varphi_{hd} = L_{hd}/L_{sys}$
Compression vol. length	$\varphi_{cs} = L_{cs}/L_{sys}\ \ ,\ \ \varphi_{cd} = L_{cd}/L_{sys}$
Regenerator vol. length	$\varphi_{reg} = L_{reg}/L_{sys}$
Piston thickness	$\varphi_p = L_p/L_{sys}\ \ ,\ \ \varphi_d = L_d/L_{sys}$
Section diameter	$\phi_{cyl} = d_{cyl}/L_{sys}\ \ ,\ \ \phi_h = d_{heat}/d_{cyl}\ \ ,\ \ \phi_c = d_{cool}/d_{cyl}$
Limits	$0 < \phi_{..} < 1 \quad , \quad 0 < \varphi_{..} < 1 \quad , \quad 0 < \Phi_{..} < 1$

The kinematic of the crank mechanism is restructured by replacing the parameters with their non-dimensional forms, which are obtained by taking each parameter's ratio to the system length, L_{sys} (Table 5.1). As all the parameters are less than L_{sys}, non-dimensional parameters can only take values between the lower limit of 0 and the upper limit of 1.

By substituting non-dimensional parameters, the displacement equations of the power and the displacer pistons can be rewritten as follows:

$$x_p(t) = L_{sys}\left[\varphi_{p1}\cos\theta_p - \varphi_{p2}\cos(\arcsin\left(\varphi_{p1}/\varphi_{p2}\ \sin\theta_p\ \right)) + \varphi_p/2\right]\ , \tag{5.3}$$

$$x_d(t) = L_{sys}\left[\varphi_{d1}\cos\theta_d - \varphi_{d2}\cos(\arcsin\left(\varphi_{d1}/\varphi_{d2}\ \sin\theta_d\right)) + \varphi_{d3} + \varphi_d\right]\ . \tag{5.4}$$

Velocity and acceleration equations for both pistons, derivations of which are given in Appendix A.2-A.3, are rewritten in terms of non-dimensional parameters as follows:

$$\dot{x}_p = -\ L_{sys}\ \varphi_{p1}\ \dot{\theta}_p\ \sin\theta_p \left[\ 1 - \frac{\varphi_{p1}}{\varphi_{p2}}\ \frac{\cos\theta_p}{K_p}\ \right]\ , \tag{5.5}$$

$$\dot{x}_d = -\ L_{sys}\ \varphi_{d1}\ \dot{\theta}_d\ \sin\theta_d \left[\ 1 - \frac{\varphi_{d1}}{\varphi_{d2}}\ \frac{\cos\theta_d}{K_d}\ \right]\ , \tag{5.6}$$

$$\begin{aligned}\ddot{x}_p = -\ L_{sys}\ \varphi_{p1}\ \Bigg\{ &\left(\ddot{\theta}_p\ \sin\theta_p + \dot{\theta}_p^2\ \cos\theta_p\right)\left(1 - \frac{\varphi_{p1}}{\varphi_{p2}}\ \frac{\cos\theta_p}{K_p}\ \right) \\ &+\ \frac{\varphi_{p1}}{\varphi_{p2}}\ \frac{\left(\dot{\theta}_p\ \sin\theta_p\right)^2}{K_p}\ \left[1 - \left(\frac{\varphi_{p1}}{\varphi_{p2}}\frac{\cos\theta_p}{K_p}\right)^2\right]\Bigg\}\ ,\end{aligned} \tag{5.7}$$

$$\begin{aligned}\ddot{x}_d = -\ L_{sys}\ \varphi_{d1}\ \Bigg\{ &\left(\ddot{\theta}_d\ \sin\theta_d + \dot{\theta}_d^2\ \cos\theta_d\right)\left(1 - \frac{\varphi_{d1}}{\varphi_{d2}}\ \frac{\cos\theta_d}{K_d}\ \right) \\ &+\ \frac{\varphi_{d1}}{\varphi_{d2}}\ \frac{\left(\dot{\theta}_d\ \sin\theta_d\right)^2}{K_d}\ \left[1 - \left(\frac{\varphi_{d1}}{\varphi_{d2}}\frac{\cos\theta_d}{K_d}\right)^2\right]\Bigg\}\ ,\end{aligned} \tag{5.8}$$

where, $K_p = \sqrt{1 - (\varphi_{p1}/\varphi_{p2}\sin\theta_p)^2}$, and $K_d = \sqrt{1 - (\varphi_{d1}/\varphi_{d2}\sin\theta_d)^2}$.

Kinematic constraints are rewritten in terms of non-dimensional parameters as below:

$$KC_1 = \frac{\Phi_d - \varphi_{d3} - \varphi_d}{\Phi_p - \varphi_p} \ , \tag{5.9}$$

$$KC_2 = \frac{\Phi_p}{\Phi_d - \varphi_d} \ . \tag{5.10}$$

5.3. Work and Power Equations

Indicated work and power are calculated, in terms of pressure and volume, as done for the first-order analysis:

$$W_{ind} = \oint P dV = \oint P \frac{\partial (Ax)}{\partial t} dt = A \oint P \ \dot{x} \ dt \ , \tag{5.11}$$

$$\mathcal{P}_{ind} = \frac{\partial W_{ind}}{\partial t} = A \ P \ \dot{x} \ . \tag{5.12}$$

Crank work and power are calculated as follows, in terms of angular velocity, ω, and torque created by forces on the piston rods due to pressure differences on both sides of the pistons, which are illustrated in Figure 5.4:

$$W_{cr} = \oint \vec{\mathcal{T}} \cdot d\vec{\theta} = \oint \vec{\mathcal{T}} \cdot \ \frac{\partial \vec{\theta}}{\partial t} \, dt = \oint \vec{\mathcal{T}} \cdot \vec{\omega} \, dt \ , \tag{5.13}$$

$$\mathcal{P}_{cr} = \frac{\partial W_{cr}}{\partial t} = \vec{\mathcal{T}} \cdot \vec{\omega} \ \ . \tag{5.14}$$

The crank work equation is rewritten as follows, by substituting piston torques, the derivation of which is given in Appendix B:

$$W_{cr} = \oint (\vec{\mathcal{T}}_p + \vec{\mathcal{T}}_d) \cdot d\vec{\theta} = \oint (\vec{\mathcal{T}}_p + \vec{\mathcal{T}}_d) \cdot \vec{\omega} \, dt \ . \tag{5.15}$$

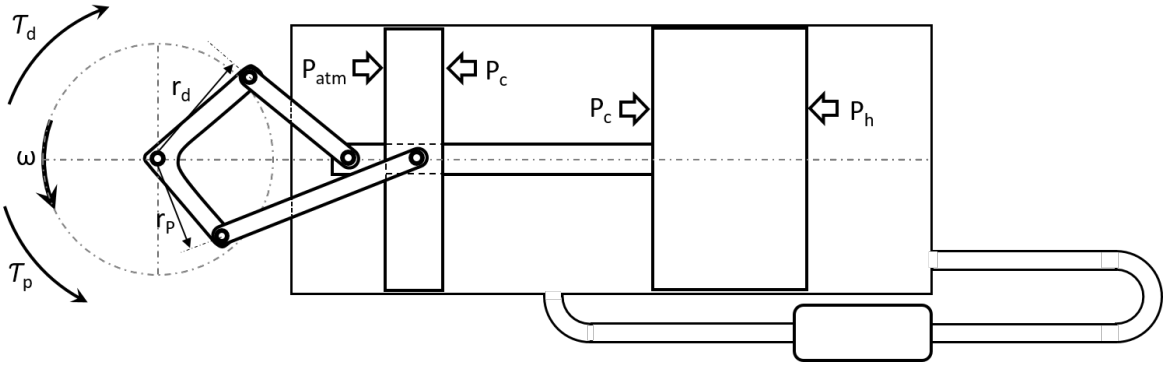


Figure 5.4. Torque on the crankshaft due to pressure difference on the pistons.

The piston torques, $\vec{\mathcal{T}}_p$, $\vec{\mathcal{T}}_d$, in Equation 5.15, and their terms, $\vec{F}_p$, $\vec{F}_d$, $\vec{r}_p$, and $\vec{r}_d$ are listed in Table 5.2. Derivation of the forces $\vec{F}_p$ and $\vec{F}_d$ are given in Appendix B.

Table 5.2. Torque equations.

Power piston torque	$\vec{\mathcal{T}}_p = \vec{r}_p \times \vec{F}_p$
Displacer piston torque	$\vec{\mathcal{T}}_d = \vec{r}_d \times \vec{F}_d$
Piston piston force	$\vec{F}_p(t) = (m_p\ \ddot{x}_p - A\ (P_{atm} - P_c))\ /\ \cos\beta_p$
Displacer piston force	$\vec{F}_d(t) = (m_d\ \ddot{x}_d - A\ (P_c - P_h))\ /\ \cos\beta_d$
Power piston moment arm	$\vec{r}_p(t) = L_{sys}\ \varphi_{p1}\ \sin\theta_p\ [(\varphi_{p1}/\varphi_{p2})\cos\theta_p - \cos\beta_p]$
Displacer piston moment arm	$\vec{r}_d(t) = L_{sys}\ \varphi_{d1}\ \sin\theta_d\ [(\varphi_{d1}/\varphi_{d2})\cos\theta_d - \cos\beta_d]$

5.4. Governing Equations for Calculating Work Output

The fundamental laws in Figure 5.5 govern differential equations to obtain three primary unknowns, pressure, temperature, and velocity vector. In this study, governing equations are applied on three control volumes:

- expansion volume, V_h: including expansion swept and dead volumes, V_{hs}, V_{hd},
- compression volume, V_c: including expansion swept and dead volumes, V_{cs}, V_{cd},
- regeneration volume, V_r: including gas volume in the regenerator.

Continuity Equation

$$\frac{\partial}{\partial t}\int_{cv} \rho \, dV + \int_{cs} \rho \, (\vec{u} \cdot \vec{n}) \, dA = 0$$

Momentum Equation

$$\sum \vec{F} = \frac{\partial}{\partial t}\int_{cv} \rho \, \vec{u} \, dV + \int_{cs} \vec{u} \, \rho \, (\vec{u} \cdot \vec{n}) \, dA$$

Energy Equation

$$\frac{\partial}{\partial t}\int_{cv} \rho \, e \, dV + \int_{cs} \rho \, h \, (\vec{u} \cdot \vec{n}) \, dA = \dot{Q} - \dot{W}$$

$$\rho = P \; / \; RT \quad , \quad e = c_V \, T \quad , \quad h = c_P \, T$$

Figure 5.5. Governing equations.

All control volumes are fixed in the reference coordinate system. Expansion and compression swept volumes are deforming due to the movement of the power and the displacer pistons, while all other volumes are non-deforming. The flow velocity of the working fluid, u_f, is positive in the +x direction. The flow's pressure and temperature at the control volumes' interfaces are determined as shown below:

$$u_f \geq 0: \qquad P_{hf} = P_r \qquad T_{hf} = T_r \qquad P_{cf} = P_c \qquad T_{cf} = T_c\,, \tag{5.16}$$

$$u_f < 0: \qquad P_{hf} = P_h \qquad T_{hf} = T_h \qquad P_{cf} = P_r \qquad T_{cf} = T_r\,, \tag{5.17}$$

where the subscript hf represents the interface between V_h and V_r, and cf represents the interface between V_c and V_r.

5.4.1. Continuity Equation

The continuity equation in Figure 5.5 is applied to all three control volumes (Figure 5.6). The total mass is conserved because the Stirling engine is a closed system.

Expansion volume

$$A\,\partial\left(\rho_h\,x_h\right)/\partial t - N_h\,\phi_h^2\,A\,\rho_{hf}\,u_f = 0$$

Compression volume

$$A\,\partial\left(\rho_c\,x_c\right)/\partial t + N_c\,\phi_c^2\,A\,\rho_{cf}\,u_f = 0$$

Regenerator volume

$$N_h\,\phi_h^2\,A\,\partial\left(\rho_r\,L_{reg}\right)/\partial t - N_c\,\phi_c^2\,A\,\rho_{cf}\,u_f + N_h\,\phi_h^2\,A\,\rho_{hf}\,u_f = 0$$

Figure 5.6. Continuity equations.

Substituting the ideal gas relation into equations in Figure 5.6 and simplifying (see Appendix C.1 for the details), one sets:

$$(\dot{P}_h\, T_h - P_h\, \dot{T}_h)(L_{hs} + N_h\, \phi_h^2\, 2L_{hd}) + P_h\, T_h\, \dot{L}_{hs} - N_h\, \phi_h^2\, P_{hf}\, \frac{T_h^2}{T_{hf}}\, u_f = 0\,, \qquad (5.18)$$

$$(\dot{P}_c\, T_c - P_c\, \dot{T}_c)(L_{cs} + N_c\, \phi_c^2\, L_{cd}) + P_c\, T_c\, \dot{L}_{cs} + N_c\, \phi_c^2\, P_{cf}\, \frac{T_c^2}{T_{cf}}\, u_f = 0\,, \qquad (5.19)$$

$$(\dot{P}_r\, T_r - P_r\, \dot{T}_r)\, L_{reg}\, N_h\, \phi_h^2 + u_f\, T_r^2 \left(-N_c\, \phi_c^2\, \frac{P_{cf}}{T_{cf}} + N_h\, \phi_h^2\, \frac{P_{hf}}{T_{hf}} \right) = 0\,. \qquad (5.20)$$

5.4.2. Momentum Equation

Flow velocity is assumed to be same at each control volume interface, and it is derived by applying the momentum equation in Figure 5.5 to the regenerator control volume (Figure 5.7).

Regenerator volume

$$\sum F_x = N_h\, \phi_h^2\, A\, (P_c - P_h)$$

$$\sum F_x = N_h\, \phi_h^2\, A\, \partial(\rho_r\, u_f\, L_{reg})/\partial t - N_c\, \phi_c^2\, A\, \rho_{cf}\, u_f^2 + N_h\, \phi_h^2\, A\, \rho_{hf}\, u_f^2$$

Figure 5.7. Momentum equations.

Substituting the ideal gas relation into equations in Figure 5.7 and simplifying (see Appendix C.2 for the details), one sets:

$$R\, T_r^2\, (P_c - P_h) = (\dot{P}_r\, T_r - P_r\, \dot{T}_r)\, u_f\, L_{reg} + P_r\, T_r\, u_f\, L_{reg} + T_r^2\, u_f^2 \left(-\frac{N_c\, \phi_c^2}{N_h\, \phi_h^2}\, \frac{P_{cf}}{T_{cf}} + \frac{P_{hf}}{T_{hf}} \right)\,. \qquad (5.21)$$

5.4.3. Energy Equation

Conservation of energy equations for each control volume, obtained by applying the energy equation in Figure 5.5 for calculating the pressure. Figure 5.8 gives heat transfer and work rate equations.

Expansion volume

$$A\,\partial(e_h\,\rho_h\,x_h)/\partial t - N_h\,\phi_h^2\,A\,h_{hf}\,\rho_{hf}\,u_f = \dot{Q}_h - \dot{W}_h$$
$$\dot{Q}_h = A\,h_{cv}\,(T_d - T_h) + N_h\,4A\,\phi_h\,2\varphi_{hd}\,U_h\,(T_{sh} - T_h)\,/\,\phi_{cyl}$$
$$\dot{W}_h = A\,P_h\,\dot{L}_{hs}$$

Compression volume

$$A\,\partial(e_c\,\rho_c\,x_c)/\partial t + N_c\,\phi_c^2\,A\,h_{cf}\,\rho_{cf}\,u_f = \dot{Q}_c - \dot{W}_c$$
$$\dot{Q}_c = A\,h_{cv}\,((T_d - T_c) + (T_p - T_c)) + N_c\,4A\,\phi_c\,\varphi_{cd}\,U_c\,(T_{sc} - T_c)\,/\,\phi_{cyl}$$
$$\dot{W}_c = A\,P_c\,\dot{L}_{cs}$$

Regenerator volume

$$N_h\,\phi_h^2\,A\,\partial(e_r\,\rho_r\,L_{reg})/\partial t - N_c\,\phi_c^2\,A\,h_{cf}\,\rho_{cf}\,u_f + N_h\,\phi_h^2\,A\,h_{hf}\,\rho_{hf}\,u_f = \dot{Q}_r - \dot{W}_r$$
$$\dot{Q}_r = N_h\,4A\,\phi_h\,\varphi_{reg}\,h_{cv}\,(T_{reg} - T_r)\,/\,\phi_{cyl}$$
$$\dot{W}_r = 0$$

Figure 5.8. Energy equations.

Substituting the ideal gas relation into the equations in Figure 5.8 and simplifying (see Appendix C.3 for the details), the following equations are obtained:

$$c_V\ \dot{P}_h\ (L_{hs} + N_h\ \phi_h^2\ 2L_{hd}) + (c_V + R)\ P_h\ L_{hs} - N_h\ \phi_h^2\ c_P\ P_{hf}\ u_f = R\left(h_{cv}\ (T_d - T_h) + 8\ N_h\ A\ \frac{\phi_h}{\phi_{cyl}}\ \varphi_{hd}\ U_h\ (T_{sh} - T_h)\right), \tag{5.22}$$

$$c_V\ \dot{P}_c(L_{cs} + N_c\ \phi_c^2\ L_{cd}) + (c_V + R)\ P_c\ \dot{L}_{cs} + N_c\ \phi_c^2\ c_P\ P_{cf}\ u_f = R\left(h_{cv}\ (T_d + T_p - 2T_c) + 4\ N_c\ A\ \frac{\phi_c}{\phi_{cyl}}\ \varphi_{cd}\ U_c\ (T_{sc} - T_c)\right), \tag{5.23}$$

$$c_V\ \dot{P}_r\ L_{reg} + c_P\ u_f\left(-\frac{N_c\ \phi_c^2}{N_h\ \phi_h^2} P_{cf} + P_{hf}\right) = 4R\ \frac{\varphi_{reg}}{\phi_{cyl}\ \phi_h}\ h_{cv}\ (T_{reg} - T_r)\,. \tag{5.24}$$

The energy balance for the pistons and the regenerator block are as follows:

$$c_d\ m_d\ \dot{T}_d = A\ h_{cv}\ ((T_h - T_d) + (T_c - T_d))\ , \tag{5.25}$$

$$c_p\ m_p\ \dot{T}_p = A\ h_{cv}\ (T_c - T_p)\,, \tag{5.26}$$

$$c_{reg}\ m_{reg}\ \dot{T}_{reg} = 4A\ h_{cv}\ \frac{\phi_h}{\phi_{cyl}}\ \varphi_{reg}\ (T_r - T_{reg})\,. \tag{5.27}$$

5.5. Output Variables and ODE's

The variables to be used for obtaining work output are calculated by the ordinary differential equations (ODE) in Figure 5.9, which are derived from a corresponding governing equation given in Section 5.4:

- Pressure of the control volumes from the energy equation,
- Temperature of the control volumes from the continuity equation,
- Temperature of the pistons and the regenerator block from the energy equation,
- Flow velocity from the momentum equation.

$$\dot{P}_h(t) = \frac{Rh_{cv}(T_d - T_h) + 8RN_h\phi_h\varphi_{hd}U_h(T_{sh} - T_h)/\phi_{cyl} - c_P(P_h\dot{L}_{hs} - N_h\phi_h^2 P_{hf}u_f)}{c_V(L_{hs} + N_h\phi_h^2\ 2L_{hd})}$$

$$\dot{P}_c(t) = \frac{Rh_{cv}(T_d + T_p - 2T_c) + 4RN_c\phi_c\varphi_{cd}U_c(T_{sc} - T_c)/\phi_{cyl} - c_P(P_c\dot{L}_{cs} + N_c\phi_c^2 P_{cf}u_f)}{c_V(L_{cs} + N_c\phi_c^2 L_{cd})}$$

$$\dot{P}_r(t) = \frac{4R\varphi_{reg}}{c_V L_{reg}\phi_{cyl}\phi_h}h_{cv}(T_{reg} - T_r) + \frac{c_P u_f}{c_V L_{reg}}\left(\frac{N_c\phi_c^2}{N_h\phi_h^2}P_{cf} - P_{hf}\right)$$

$$\dot{T}_h(t) = \frac{\dot{P}_h T_h}{P_h} + \frac{\dot{L}_{hs}T_h}{L_{hs} + N_h\phi_h^2\ 2L_{hd}} - \frac{P_{hf}}{P_h}\frac{T_h^2}{T_{hf}}\frac{N_h\phi_h^2 u_f}{L_{hs} + N_h\phi_h^2\ 2L_{hd}}$$

$$\dot{T}_c(t) = \frac{\dot{P}_c T_c}{P_c} + \frac{\dot{L}_{cs}T_c}{L_{cs} + N_c\phi_c^2 L_{cd}} + \frac{P_{cf}}{P_c}\frac{T_c^2}{T_{cf}}\frac{N_c\phi_c^2 u_f}{L_{cs} + N_c\phi_c^2 L_{cd}}$$

$$\dot{T}_r(t) = \frac{T_r}{P_r}\left[\dot{P}_r + \frac{u_f T_r}{L_{reg}}\left(-\frac{N_c\phi_c^2}{N_h\phi_h^2}\frac{P_{cf}}{T_{cf}} + \frac{P_{hf}}{T_{hf}}\right)\right]$$

$$\dot{T}_p(t) = \frac{Ah_{cv}}{c_p m_p}(T_c - T_p)$$

$$\dot{T}_d(t) = \frac{Ah_{cv}}{c_d m_d}(T_h + T_c - 2T_d)$$

$$\dot{T}_{reg}(t) = \frac{4Ah_{cv}}{c_{reg}m_{reg}}N_h\frac{\phi_h}{\phi_{cyl}}\varphi_{reg}(T_r - T_{reg})$$

$$\dot{u}_f(t) = \frac{1}{L_{reg}}\frac{T_r}{P_r}\left[R(P_c - P_h) + u_f^2\left(\frac{N_c\phi_c^2}{N_h\phi_h^2}\frac{P_{cf}}{T_{cf}} - \frac{P_{hf}}{T_{hf}}\right)\right] - u_f\left(\frac{\dot{P}_r}{P_r} - \frac{\dot{T}_r}{T_r}\right)$$

Figure 5.9. Ordinary differential equations.

5.6. Design Premises and Assumptions

This section investigates the effects of engine size, pressure, and engine speed and gives the design premises and the assumptions for the WHR system. Regarding engine size, the packaging is the primary constraint of the WHR system. Due to possible locations on the truck, which are mentioned in Chapter 3, the system length, L_{sys}, is limited to 500 mm, while the cylinder diameter, d_{cyl}, is limited to 250 mm when heat exchanger around the cylinder is considered. The most important factor affecting the efficiency of a Stirling engine is the heat transfer between the heat sources and the cylinder via exchangers. Therefore, the dimensions and number of heating and cooling tubes in the exchangers will be clarified next. In Chapter 2, heating and cooling tubes are called dead volumes. According to the results of the first-order analysis, dead volumes should be minimized to increase engine efficiency. However, on the other hand, they should be large enough to provide the necessary heat transfer. A balance between these two issues can be reached by second-order analysis. The heat transfer rate in a heat exchanger is given by;

$$\dot{Q} = U A_s \ \Delta T \,, \tag{5.28}$$

where $\dot{Q}$ is the heat transfer rate between the two fluids, U is the overall heat transfer coefficient, A_s is the heat transfer surface area and ΔT is the log mean temperature difference.

The overall heat transfer coefficient is calculated by;

$$U = \left[\frac{1}{h_{cv,source}} + \frac{t_{tube}}{k_{tube}} + \frac{1}{h_{cv,helium}} \right]^{-1} , \tag{5.29}$$

where $h_{cv,source}$ and $h_{cv,helium}$ are the convective heat transfer coefficients in the heat exchanger passages. The conduction resistance term can be neglected, as it is much smaller than the convective terms.

As higher efficiency can be achieved by a higher heat transfer rate, the overall heat transfer coefficient, accordingly convective heat transfer coefficients (h_{cv}) of the flow, should be maximized. Due to the specified flow rate of the sources, given in Chapter 3, h_{cv} of the exhaust gas and the cooling water flows can be increased by increasing the flow velocity, which can be achieved by decreasing hydraulic diameter of the heat exchanger. The limitation for the smaller hydraulic diameter is the number and size of the working fluid tubes, which means the tubes are needed to be downsized. Consequently, a less working fluid is required for an effective heat transfer, and correspondingly size of the Stirling engine gets smaller. In this case, cyclic work decreases, but on the other side, desired power output can be achieved by running the engine at a higher speed. Similarly, h_{cv} of the working fluid flow can be increased by increasing the flow velocity, u_f, with higher pressure or higher engine speed.

The effect of pressure on the Stirling engine's performance is illustrated in the piston torques in Figures 5.10 as an example. In the graphs, four values for initial system pressure are compared for a random case of kinematic parameters by calculating the torque created by both pistons under varying engine speeds, from 0 to 1500 rpm. Positive torque means that the working fluid exerts force; correspondingly, work is done by the engine during expansion. Negative torque means that external force is applied to compress the working fluid; work is done on the engine. The engine is supposed to create power if the net torque or work within a cycle is positive. Due to the graphs, the pressure difference between both sides of the displacer piston produces negligible torque, $\mathcal{T}_d$, which means pressures in the expansion and the compression volumes are almost the same, as assumed for first-order analysis. In all graphs, the net torque of the power piston, $\mathcal{T}_p$, decreases with increasing engine speed due to reduced heat transfer rate, and it becomes zero at a particular engine speed ($W = 0$ point), and no work is generated. Although the amplitude of $\mathcal{T}_p$ increases with increasing factor value, zero work output is reached at lower engine speed values. As a common point for all graphs, when indicated work at 250 rpm (black marked curve on the charts) is compared, it decreases with the pressure increase. The same behavior is observed for the engine size factors, the system length, and the diameter ratio.

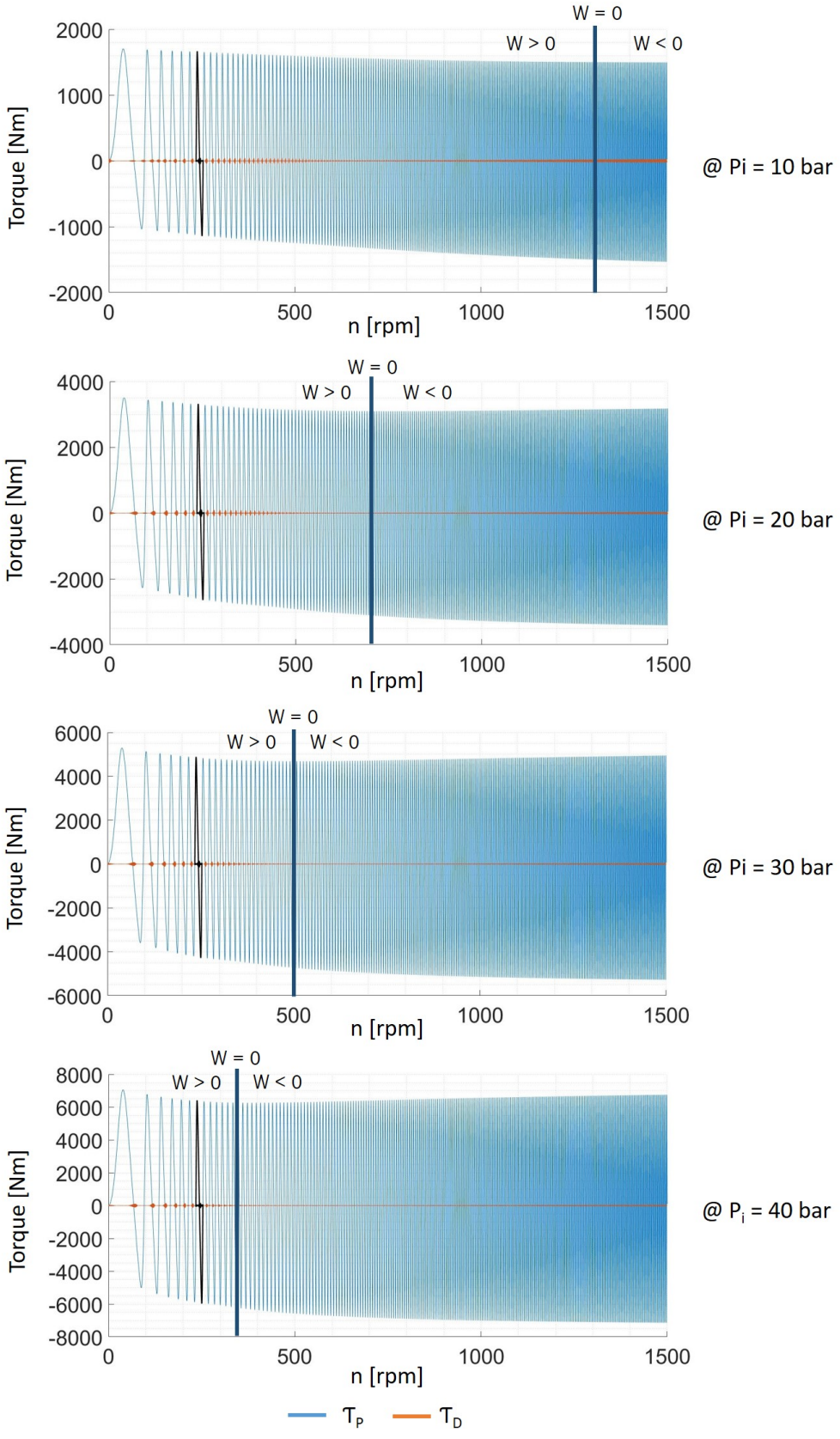


Figure 5.10. Effect of pressure and engine speed on piston torque.

5.6.1. Preliminary Analysis

A preliminary analysis is performed with two Stirling engine configurations given in Table 5.3 without any constraint on the heat exchanger size to understand the system's behavior. CONFIG-1 has a larger volume with a lower initial pressure and runs at a lower engine speed than CONFIG-2. The configurations are analyzed at low, medium, and high engine speeds. At each rate, heat transfer coefficients are defined with trial runs by estimating the flow velocity u_f. The analysis shows that both configurations can supply more than 2 kW power output without size constraints. The efficiencies are less than 10%, well below the theoretical values calculated in Chapter 3. Low efficiency requires a heat input of more than 25 kW, which is much higher than the maximum heat transfer rate from the exhaust gas in the EGR option (12.6 kW) or the tailpipe option (20.5 kW). As a result of the preliminary analysis, a maximum of 1 kW indicated power could be expected from the WHR system.

Due to the outputs of the preliminary analysis, the heat transfer coefficients can be adjusted according to the average temperatures of the control volumes in Figure 5.11. For the desired heat transfer rate, flow velocity, u_f, can reach a maximum value of 100 m/s, corresponding to a mean velocity of around 50 m/s. The convective heat transfer coefficient of Helium flow (gas properties from [44]) for updated temperature and flow velocity is given in Figure 5.12 for three control volumes. Diameters for the heater and the cooler tubes are selected as 1.5 and 1 mm. Flow inside the regenerator is also assumed as similar to the heater tube. Properties of heat source fluids are shown in Table 5.4 for the given temperature range, where k is thermal conductivity, μ, and ν are dynamic and kinematic viscosity.

Table 5.3. Preliminary analysis results.

	CONFIG-1			**CONFIG-2**		
L_{sys} $[mm]$	500			300		
ϕ_{cyl}	0.4			0.4		
P_i $[bar]$	12			30		
n $[rpm]$	250	500	750	750	1000	1250
u_f $[m/s]$	50	100	150	50	100	125
h_{cv} $[kW/m^2K]$	2	4	6	5	8.5	10
U_c $[kW/m^2K]$	1.20	1.75	2.00	2.80	3.60	3.80
U_h $[kW/m^2K]$	0.50	0.55	0.60	1.60	1.63	1.70
P_{mean} $[bar]$	14.5	14.3	14.2	37.3	36.8	36.9
W_{ind} $[kJ]$	0.57	0.33	0.17	0.18	0.14	0.09
Q_h $[kJ]$	5.97	4.97	4.32	2.75	2.56	2.37
η [%]	9.5	6.6	4.0	6.4	5.3	3.6
$\mathcal{P}_{ind}$ $[kW]$	2.36	2.72	2.16	2.20	2.27	1.79
$\dot{Q}_h$ $[kW]$	24.9	41.5	54.0	34.4	42.7	49.3

Table 5.4. Hot and cold source fluid properties.

	Exhaust gas (@ 673 K)	**Cooling water (@ 364 K)**
ρ $[kg/m^3]$	0.525	961.9
c_P $[J/kgK]$	1151	4210
μ $[Ns/m]2$	$3.17\,10^{-5}$	$2.96\,10^{-4}$
ν $[m^2/s]$	$6.04\,10^{-5}$	$3.09\,10^{-7}$
k $[W/mK]$	$5.25\,10^{-2}$	0.678

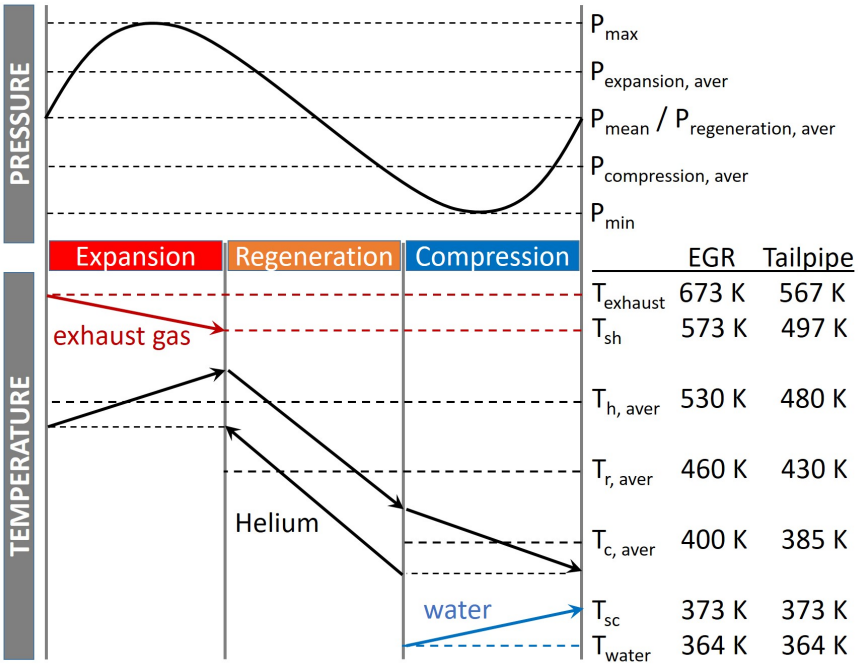


Figure 5.11. Temperature and pressure range of working fluid.

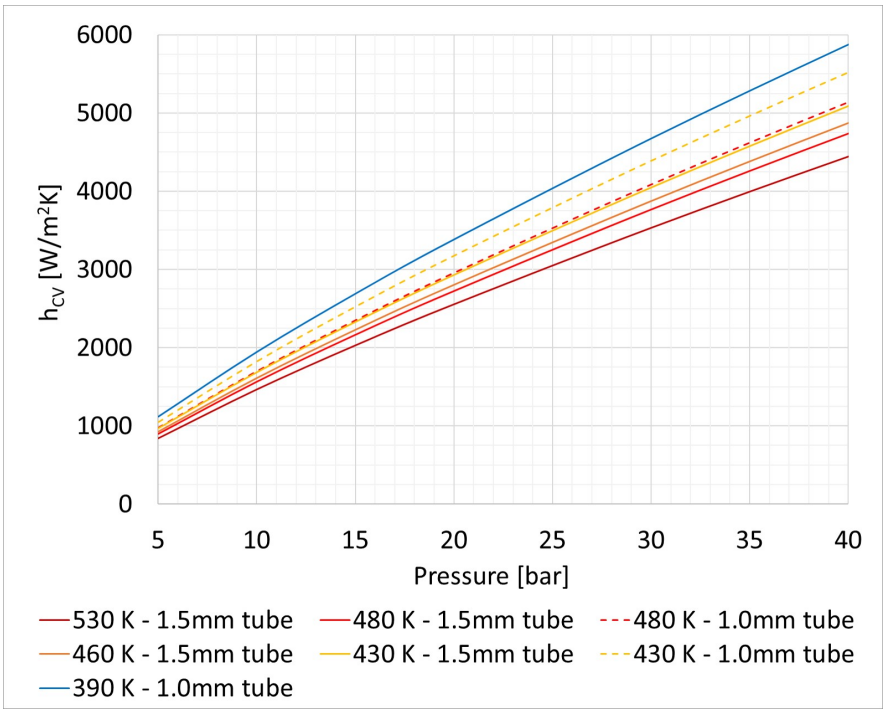


Figure 5.12. Convective heat transfer coefficient, h_{cv}, for tube flow @50m/s.

6. APPLICATION OF THE WHR SYSTEM TO A TRUCK

This chapter presents the design and implementation of a Beta-type Stirling engine for a heavy-duty truck. As a first step, the preliminary analysis is carried out with first-order analysis for estimating the engine size for the given power output target. In the second step, the power output range of the WHR system is investigated with second-order analysis.

6.1. Preliminary Analysis of Beta-Type Stirling Engine for WHR System

The analysis in Chapter 4 shows that the Beta-type Stirling engine can maintain the target power with less volume than the other two types due to overlap volume. Because of packaging limitations, the Beta-type is the best choice. In Table 6.1, the power output of the Beta-type configuration is shown at each operation point of the road measurement and the bench test, the details of which are given in Table 3.2. The exhaust gas mass and volume flow rate values in Table 3.1 show that exhaust gas contains more heat energy than the Stirling engine needs at any operation point. Thus the Stirling engine provides a maximum power output, which is more than 1% ICE power, with changing operating conditions of the ICE. The contribution of the WHR system on power output reduces fuel consumption by at least 1%.

To evaluate the WHR system on a truck, additional weight on the vehicle and increased back pressure in the exhaust line should be considered, as these effects increase fuel consumption. Although the thermal efficiency of Stirling engines is higher than the other alternative cycles, their most significant obstacle is the low power-to-weight ratio. With a ratio assumption of 30 kg/kW, the engine's weight is supposed to be 90 kg for the target of 3 kW power output. A weight reduction of 500 kg on this type of truck results in about 0.8% less fuel consumption: the additional weight of the WHR system will cause an increase of fuel consumption for less than 0.2%. The experiences show that back pressure increase in the exhaust line results in up to 0.2% increase in fuel consumption. Both effects result in 0.4% fuel consumption increase. The total con-

tribution of WHR to fuel consumption is supposed to be 0.4% reduction, which means the Stirling cycle might be an option for further WHR investigations. Increasing P_{mean} is a weight and volume reduction potential for the Stirling WHR system.

Table 6.1. Power output of Beta-type WHR system at various operation points.

Operation Point (OP)	Road Measurements					Bench Test
	1	2	3	4	5	
Temperature Ratio,τ	1.64	1.71	1.72	1.77	1.85	2.18
W_{ind} [J]	140.3	152.3	154.7	162.8	175.1	220.7
W_{shaft} [J]	94.8	105.7	108.0	115.1	126.3	165.8
Power [kW]	2.5	2.8	2.9	3.1	3.4	4.4
Power Ratio (WHR/ICE)	2.1%	5.2%	1.5%	1.2%	1.1%	1.4%

6.2. Application of the Second Order Analysis

This section presents the design and implementation of a Beta-type Stirling engine by comparing different configurations for two heat source options. The first option is the EGR system due to its high heat capacity (Figure 3.2). It is also advantageous because the space obtained by removing the EGR cooler can be used together with existing inlets and outlets (Figure 6.1). The modifications on the existing exhaust line and cooling water circuit can be minimized. The second option is the tailpipe because of the high mass flow rate (133% higher than the EGR option).

As packaging constraints limit the size of the heat exchangers, shell-and-tube type exchangers are used for heating and cooling (Figure 6.1). A multi-pass flow heat exchanger (one-shell pass & two-tube passes) is chosen on the heating side to achieve the necessary heat transfer rate with a minimum number of tubes. On the cooling side, a multi-pass flow (similar to the heating side) or cross-flow heat exchanger (one fluid mixed, the other unmixed) can be chosen, depending on the cooling rate.

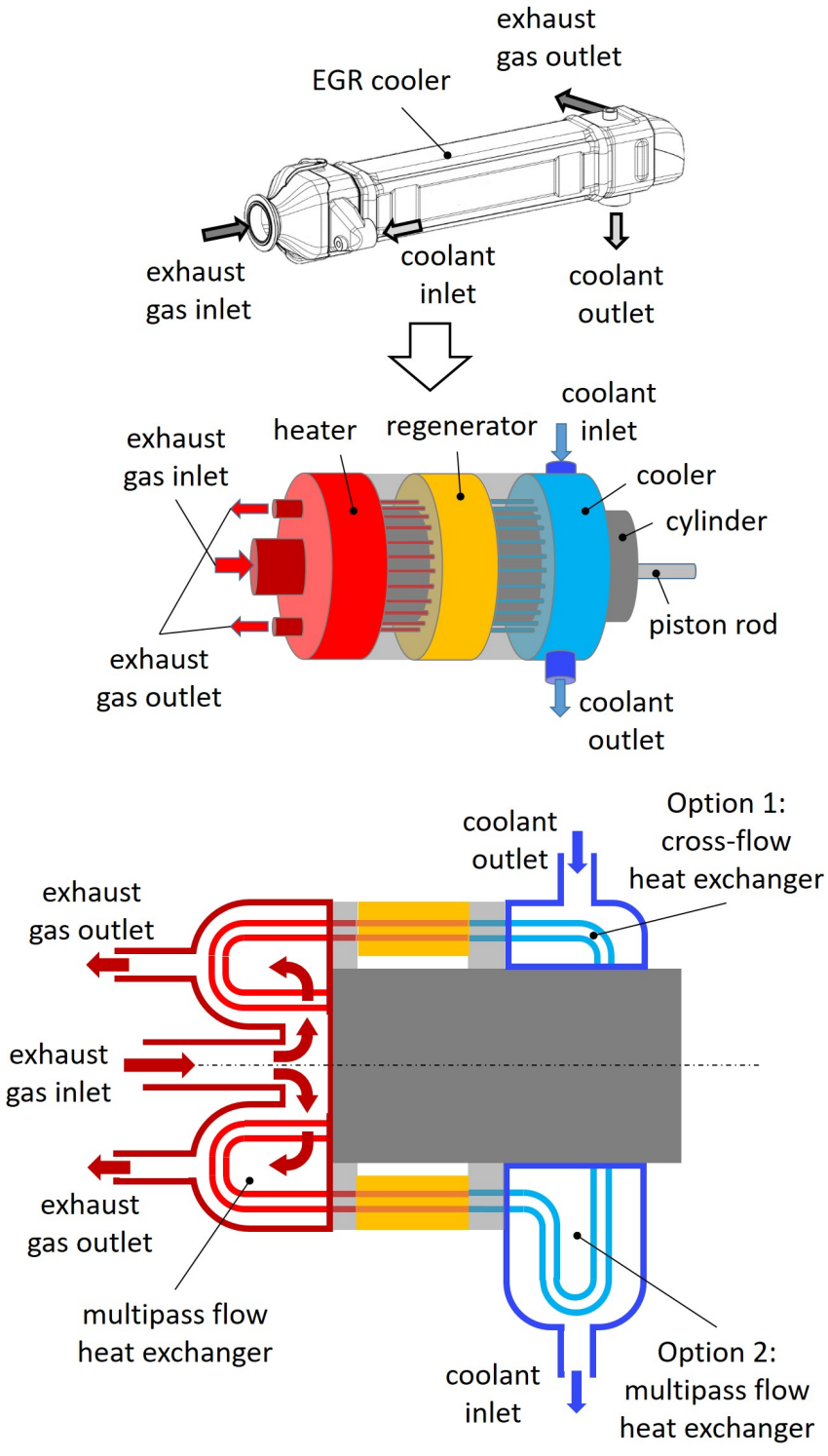


Figure 6.1. Layout of the heat exchangers used in the EGR option.

6.2.1. Stirling Engine Configurations

This section considers four different system lengths, L_{sys}, changing between 200-500 mm. The initial pressure, the size, and the number of the heater and the cooler tubes are defined accordingly to maintain the maximum heat transfer rate given in Section 3. Table 6.2 gives the four configurations for both heat source options.

6.2.2. Performance of the WHR System

The steady-state solutions of the ODEs in Figure 5.9 are obtained using the engine specifications in Table 6.2. The WHR system is supposed to be speeded up by an electric motor and continue to accelerate on its own (Figure 6.2). The flywheel, coupled to the crankshaft by a gearbox for a smooth drive, minimizes the oscillations of the engine speed. In addition, $\mathcal{T}_{use}$ is applied as a resistive torque on the crankshaft coupled to an auxiliary power generator. Temperatures of the control volumes and the regenerator block also reach steady-state (Figure 6.3), matching the assumptions made in Section 5.6.

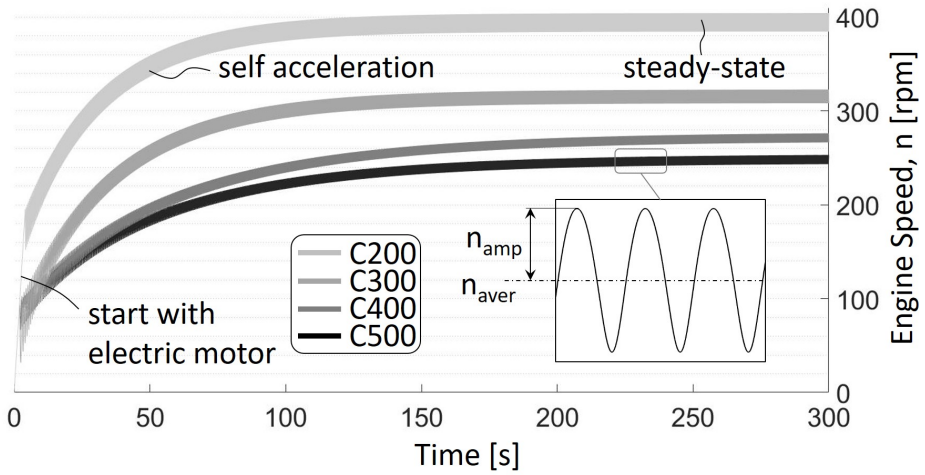


Figure 6.2. Engine speed vs. time, the EGR option.

Table 6.2. Specifications of the configurations.

	EGR Option				**Tailpipe Option**			
	C500	**C400**	**C300**	**C200**	**C500**	**C400**	**C300**	**C200**
$L_{sys}\ [mm]$	500	400	300	200	500	400	300	200
$L_{p1}\ [mm]$	40	32	24	16	40	32	24	16
$L_{p2}\ [mm]$	200	160	120	80	200	160	120	80
$L_{d1}\ [mm]$	59	47.2	35.4	23.6	59	47.2	35.4	23.6
$L_{d2}\ [mm]$	118	94.4	70.8	47.2	118	94.4	70.8	47.2
$L_{d3}\ [mm]$	167.5	134	100.5	67	167.5	134	100.5	67
$\Omega\ [deg]$	90	90	90	90	90	90	90	90
$\phi_{cyl}\ [mm]$	125	120	120	120	125	120	120	120
$\phi_h\ [mm]$	1.5	1.5	1.5	1.5	1.5	1.5	1.0	1.0
$\phi_c\ [mm]$	1.0	1.0	1.0	1.0	1.0	1.0	1.0	1.0
$L_{reg}\ [mm]$	100	80	60	40	100	80	60	40
ω_{fly}/ω_{cr}	250	250	250	250	250	250	250	250
$I_{fly}\ [kgm^2]$	0.147	0.120	0.061	0.048	0.147	0.120	0.120	0.078
$L_{hd}\ [mm]$	300	360	540	720	900	1140	720	960
$L_{cd}\ [mm]$	150	180	180	240	450	480	270	360
N_h	200	150	120	100	200	150	280	240
N_c	400	300	250	200	400	300	320	300
$V_{sw}\ [cc]$	2141	1579	1184	789	2141	1579	1184	789
$V_{cyl}\ [cc]$	2330	1738	1347	961	2636	2015	1424	1063
$P_i\ [bar]$	10	12	14	16	14	18	25	30
$m_{He}\ [g]$	1.879	1.696	1.568	1.337	3.228	3.240	3.069	2.930
$U_h\ [W/m^2K]$	630	630	615	610	695	690	690	675
$U_c\ [W/m^2K]$	1430	1720	1920	2020	1940	2375	2890	3100

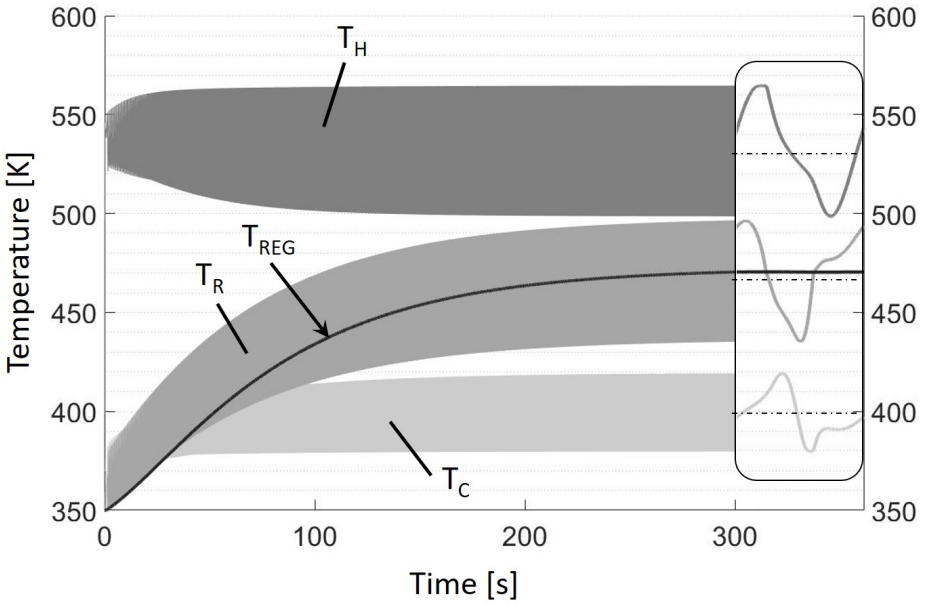


Figure 6.3. Temperature vs time, C500, the EGR option.

The output data of the EGR and the tailpipe options are given in Table 6.3. The power output, $\mathcal{P}_{use}$, is calculated as multiplication of $\mathcal{T}_{use}$ and ω_{cr}. When $\mathcal{P}_{use}$ is evaluated, all configurations supply similar power outputs. The power output of a small engine is compensated by increasing engine speed because the work output is low for a small engine size. The configurations' P-V and power piston torque diagrams are plotted in Figure 6.4 and 6.5, respectively. The useful power output is in the range of 405-455 W for the EGR option, and the efficiencies of the configurations are calculated in the range of 6.5-7.4%, which is well below the theoretical efficiency calculated in Chapter 3. As the performance of the configurations is similar, the packaging is one of the key factors for selecting the suitable engine configuration. System packaging includes the size of the cylinder, the number and length of the heater and the cooler tubes, and the flywheel size. Compared to the configuration C500, the configuration C200 has a 60% smaller volume runs about 60% faster, and the necessary moment of inertia of the flywheel is only 20%. As a result, C200 appears to be the leading configuration regarding the packaging criterion.

Despite the tailpipe option's higher heat rate, the configurations' efficiencies, which are in the range of 4.8-6.6%, are lower than the EGR option's due to the lower temperature ratio. All configurations generate indicated work output at the level of the EGR option but at a higher engine speed. This results in higher useful power output in the 450-550 W range at the expense of larger heat exchangers. Due to the increased number and length of the tubes, the dead volume of the tailpipe option corresponds to 1.5-3 times the EGR option's.

The strength of the components is also an important criterion to be considered. The forces on the pistons are directly proportional to the cylinder pressure, and C500 is advantageous because it operates under lower pressure when compared to the others. The maximum force on the power piston of C500 is about 16.3 kN in the EGR option, while the force on C200 reaches 42.6 kN in the tailpipe option.

Table 6.3. Output of the configurations.

	EGR Option				**Tailpipe Option**			
	C500	**C400**	**C300**	**C200**	**C500**	**C400**	**C300**	**C200**
$n_{aver}\,[rpm]$	248	270	321	387	302	320	346	429
$n_{amp}\,[rpm]$	5	5	7	5	5.5	6	6	6
$P_{mean}\,[bar]$	10.8	13.0	15.5	18.0	14.6	18.9	25.8	31.5
$F_p\,(max)\,[kN]$	16.3	18.1	21.4	24.7	21.3	25.4	35.6	42.6
$W_{ind}\,[kJ]$	0.11	0.094	0.08	0.06	0.11	0.09	0.07	0.06
$Q_h\,[kJ]$	1.48	1.32	1.19	0.96	1.68	1.61	1.52	1.26
$\eta\,(W_{ind}/Q_h)$	7.4 %	7.1 %	6.7 %	6.5 %	6.6 %	5.9 %	4.9 %	4.8 %
$\mathcal{T}_{use}\,[Nm]$	17.5	15	12.5	10	17.5	15	12.5	10
$\mathcal{P}_{use}\,[W]$	454	424	420	405	553	503	453	449

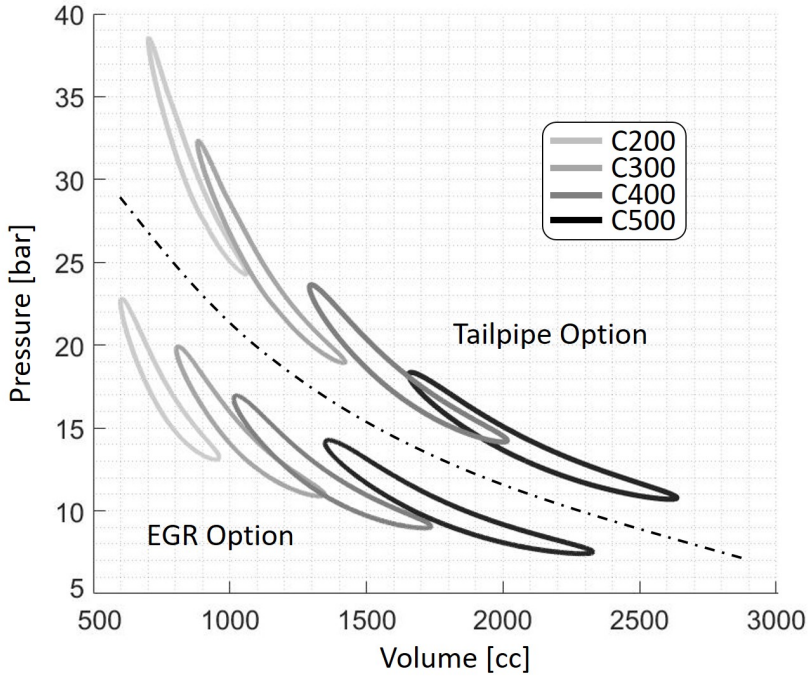


Figure 6.4. P-V diagrams.

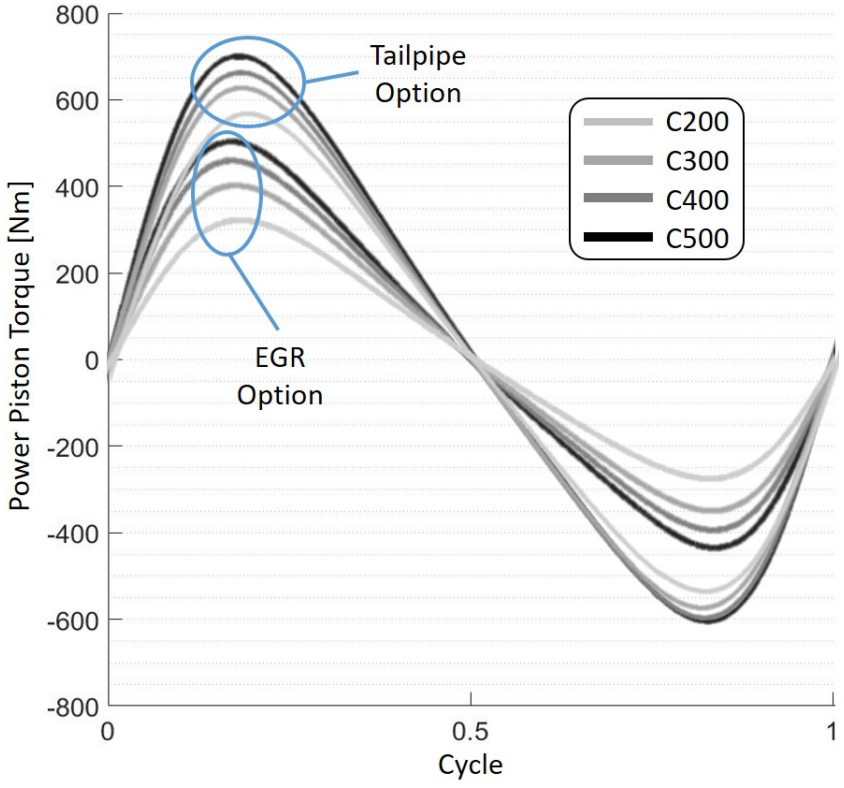


Figure 6.5. Power piston torque diagrams.

7. SUMMARY & CONCLUSIONS

In this thesis, the application of the Stirling engine for waste heat recovery (WHR) from a heavy-duty truck diesel engine is evaluated in two steps: In the first step, the theoretical non-dimensional shaft work ($\bar{W}_s$) is maximized by optimizing parameters in a first-order model with a new non-dimensionalization method for three types of Stirling engines. The optimum values of the phase angle Ω and the swept volume ratio R_{vs} are plotted for ideal and the feasible cases and for mechanism effectiveness, E range of 0.7-1.0. The results show that the Beta-type engine is the most suitable for the WHR application with its higher non-dimensional work output and moderate pressure ratio. The Beta-type achieves a higher work output because of its overlap volume, which increases the hot and cold swept volumes compared to the other types. Although the work generated by the Alpha-type is close to that produced by the Beta-type, larger total volume and pressure ratio are its disadvantages. The Gamma-type has a significantly lower non-dimensional work output and needs a greater volume, making it unfeasible to apply a WHR system on a truck. The results of the non-dimensional analysis are then used to demonstrate the preliminary application of the WHR system on a 40-ton truck without applying any constraint on the engine size. The exhaust gas is selected as the system's heat source due to its high thermal power. Three types of Stirling engines are proposed to achieve 3 kW mechanical power output, using exhaust gas temperature measurements from road tests and optimum parameter values corresponding to these temperatures. The Beta-type Stirling engine appears to be the best choice with a total packaging volume of 3525 cm^3. Although the diesel engine's power output may go from very low values of 55 kW to a high of 318 kW at the peak operating point during a typical operation mode, the exhaust temperatures do not change significantly and remain in the range of 530-600 K. Within this range. The designed Stirling engine can generate around 3 kW power output in its entire operation, corresponding to more than 1% of ICE power output. There is an additional weight and an increase in back pressure in the exhaust line, but the proposed WHR system reduces the fuel consumption by about 0.4%. This first analysis shows the Stirling engine as an option for WHR on the heavy-duty truck engines.

As a second attempt, a time-dependent analysis is carried out. The three primary unknowns of the WHR system, pressure, temperature, and velocity, are calculated from continuity, momentum, and energy equations. Four different Stirling engine configurations with different sizes, pressure, and speeds are studied. The maximum thermal power outputs of the exhaust gas at the EGR and the tailpipe are 12.6 kW and 20.5 kW, respectively. Higher heat input is available from the tailpipe. Still, there are three challenges: The first one is the lower temperature ratio (τ=1.33) than that of the EGR's, due to the average exhaust gas temperature of 567 K (Section 3). The second challenge is the change caused by back pressure and its effect on ATS. The WHR system needs to be robust not to disturb emissions during the truck's lifetime. The third challenge is a cooling system with the required capacity. The ICE cooling water can remove the heat needed from the WHR system in the case of the EGR option, with minor modifications to the cooling system. But in the case of the tailpipe, an extension of current cooling lines or a separate cooling system will be needed, which will result in additional cost. The cooling system will need at least 20 kW of cooling rate, close to the heat transfer rate of the exhaust gas.

Stirling engine power outputs for all configurations are in the range of 400-550 W, which amounts to about 0.2 % of the ICE's power. The efficiency of the configurations is between 4.8-7.4%, much lower than the theoretical values. The estimated saving for an average annual mileage of 130000 km in long-distance transport and consumption of 28.5 l/100 km is very low. There are difficulties in the application of the WHR system: The sizes of the heat exchangers used for the heat transfer from the source are larger than the size of the cylinder, and the allowed space on the vehicle may not be satisfactory. In addition, the manufacturing, assembly, and maintenance costs of the WHR system are high. As a result, this study shows that adding a Stirling engine to a heavy-duty truck for WHR is not feasible.

The results are compared to a reference engine, GPU-3 (Ground Power Unit) from General Motors Research Laboratories, which also uses helium. The ideal isothermal power output and efficiency are 7442 W and 70.5 %, corresponding to 178 J cyclic work output at 2500 rpm engine speed and 41.3 bar mean pressure [45]. The measured power output from their prototype is 3958 W, with an efficiency of 35 %. GPU-3 can generate such high power at high speed because its heat source is a fuel burner providing a much higher heat power than the exhaust gas. Their temperature ratio, τ, is 3.4 (T_h: 977 K, T_c: 288 K), much higher than the ratio of the WHR system used in this thesis.

REFERENCES

1. Dulac, J., "Global Transport Outlook to 2050, Targets and Scenarios for a Low-carbon Transport Sector", *International Energy Agency*, 2012.

2. "Global Transport Scenarios 2050", *World Energy Council*, 2011.

3. Keski-Hynnila, D., "Technology and Fuels for Economic Growth and Sustainability in the Heavy-Duty Sector", *5th International Environmentally Friendly Vehicle Conference*, Baltimore, USA, 2012.

4. Daimler, *The New Dimension in Economic Efficiency*, `http://new-actros.trucks-mercedes-benz.com/en/Economy/details.html`, accessed on July 31, 2018.

5. Daimler-Truck, *eActros LongHaul*, `https://www.mercedes-benz-trucks.com`, accessed on October 16, 2022.

6. Douadi, O., R. Ravi, M. Faqir and E. Essadiqi, "A Conceptual Framework for Waste Heat Recovery from Compression Ignition Engines: Technologies, Working Fluids Heat Exchangers", *Energy Conversion and Management: X*, Vol. 16, p. 100309, 2022.

7. Brown, A., "Technologies and Approaches to Reducing the Fuel Consumption of Medium- and Heavy-Duty Vehicles", *National Academies Press*, 2010.

8. Paanu, T., S. Niemi and P. Rantanen, "Waste Heat Recovery Bottoming Cycle Alternatives", *University of Vaasa*, 2012.

9. Erlandsson, O., T. Skare and A. Contet, "On Handling Waste Heat from Waste Heat Recovery Systems in Heavy-Duty Vehicles", *SAE Technical Paper*, Vol. 2015-01-2792, 2015.

10. Bianchi, M. and A. D. Pascale, "Bottoming Cycles for Electric Energy Generation: Parametric Investigation of Available and Innovative Solutions for the Exploitation of Low and Medium Temperature Heat Sources", *Applied Energy*, Vol. 88, pp. 1500–1509, 2011.

11. Cullen, B. and J. McGovern, "Energy System Feasibility Study of an Otto Cycle/Stirling Cycle Hybrid Automotive Engine", *Energy*, Vol. 35, pp. 1017–1023, 2010.

12. Liu, L., X. Zhang and X. Liu, "Analysis of Stirling Engine in Vehicle-mounted Exhaust Heat Recovery System", *3rd Joint International Conference on Modelling and Simulation*, Wuxi, PRC, 2010.

13. Alfarawi, S., M. Webb-Martin, S. Mahmoud and R. AL-Dadah, "Thermal Analysis of Stirling Engine to Power Automotive Alternator Using Heat from Exhaust Gases", *Energy Procedia*, Vol. 61, pp. 2395–2398, 2014.

14. Catapano, F., C. Perozziello and B. Vaglieco, "Heat Transfer of a Stirling Engine for Waste Heat Recovery Application from Internal Combustion Engines", *Applied Thermal Engineering*, Vol. 198-117492, pp. 1–12, 2021.

15. Martini, W., *Stirling Egine Design Manual*, Martini Engineering, 1983, prepared for NASA Lewis Research Center Under Grant NSG-3194.

16. Ahmadi, M., M. Ahmadi and F. Pourfayaz, "Thermal Models for Analysis of Performance of Stirling Engine: A Review", *Renewable and Sustainable Energy Reviews*, Vol. 68, pp. 168–184, 2017.

17. Hirata, K., "Schmidt Theory for Stirling Engines", *National Maritime Research Institute*, 1997.

18. Senft, J., "Optimum Stirling Engine Geometry", *Energy Research*, Vol. 26, pp. 1087–1101, 2002.

19. Cheng, C. and H. Yang, "Optimization of Geometrical Parameters for Stirling Engines Based on Theoretical Analysis", *Applied Energy*, Vol. 92, pp. 395–405, 2012.

20. Bert, J., D. Chrenko, T. Sophy, L. L. Moyne and F. Sirot, "Simulation, Experimental Validation and Kinematic Optimization of a Stirling Engine Using Air and Helium", *Energy*, Vol. 78, pp. 701–712, 2014.

21. Toghyani, S., A. Kasaeian and M. Ahmadi, "Multi-objective Optimization of Stirling Engine Using Non-ideal Adiabatic Method", *Energy Conversion and Management*, Vol. 80, pp. 54–62, 2014.

22. Toghyani, S., A. Kasaeian, S. Hashemabadi and M. Salimi, "Multi-objective Optimization of GPU3 Stirling Engine Using Third Order Analysis", *Energy Conversion and Management*, Vol. 87, pp. 521–529, 2014.

23. Hiang, T., M. Zainudin, T. Ali, R. Bakar and Y. Ali, "Study on the Phase Angle Effect for Alpha Type Stirling Engine Thermodynamics Behavior", *Engineering and Applied Sciences*, Vol. 10, pp. 7852–7855, 2015.

24. Araoz, J., M. Salomon, L. Alejo and T. Fransson, "Numerical Simulation for the Design Analysis of Kinematic Stirling Engines", *Applied Energy*, Vol. 159, pp. 633–650, 2015.

25. Ni, M., B. Shi, G. Xiao, H. Peng, U. Sultan, S. Wang, Z. Luo and K. Cen, "Improved Simple Analytical Model and Experimental Study of a 100W Beta-type Stirling Engine", *Applied Energy*, Vol. 169, pp. 768–787, 2016.

26. Alfarawi, S., R. AL-Dadah and S. Mahmoud, "Enhanced Thermodynamic Modelling of a Gamma-type Stirling Engine", *Applied Thermal Engineering*, Vol. 106, pp. 1380–1390, 2016.

27. Li, R., L. Grosu and D. Queiros-Conde, "Losses Effect on the Performance of a

Gamma Type Stirling Engine", *Energy Conversion and Management*, Vol. 114, pp. 28–37, 2016.

28. Ahmadi, M., M. Ahmadi, F. Pourfayaz, M. Bidi, H. Hosseinzade and M. Feidt, "Optimization of Powered Stirling Heat Engine with Finite Speed Thermodynamics", *Energy Conversion and Management*, Vol. 108, pp. 96–105, 2016.

29. Almajri, A., S. Mahmoud and R. Al-Dadah, "Modelling and Parametric Study of an Efficient Alpha Type Stirling Engine Performance Based on 3D CFD Analysis", *Energy Conversion and Management*, Vol. 145, pp. 93–106, 2017.

30. Xiao, G., U. Sultan, M. Ni, H. Peng, X. Zhou, S. Wang and Z. Luo, "Design Optimization with Computational Fluid Dynamic Analysis of Beta-type Stirling Engine", *Applied Thermal Engineering*, Vol. 113, pp. 87–102, 2017.

31. Shendage, D., S. Kedare and S. Bapat, "Cyclic Analysis and Optimization of Design Parameters for Beta-configuration Stirling Engine Using Rhombic Drive", *Applied Thermal Engineering*, Vol. 124, pp. 595–615, 2017.

32. Abuelyamen, A., R. Ben-Mansour, H. Abualhamayel and E. Mokheimer, "Parametric Study on Beta-type Stirling Engine", *Energy Conversion and Management*, Vol. 145, pp. 53–63, 2017.

33. Cheng, C. and Y. Chen, "Numerical Simulation of Thermal and Flow Fields Inside a 1-kW Beta-type Stirling Engine", *Applied Thermal Engineering*, Vol. 121, pp. 554–561, 2017.

34. Cheng, C. and H. Yang, "Development of a Beta-type Stirling Engine with Rhombic-drive Mechanism Using a Modified Non-ideal Adiabatic Model", *Applied Energy*, Vol. 200, pp. 62–72, 2017.

35. Aksoy, F., H. Solmaz, C. Cinar and H. Karabulut, "1.2kW Beta Type Stirling Engine with Rhombic Drive Mechanism", *Energy Research*, Vol. 41, pp. 1310–

1321, 2017.

36. Cinar, C., F. Aksoy, H. Solmaz, E. Yilmaz and A. Uyumaz, "Manufacturing and Testing of an Alpha-type Stirling Engine", *Applied Thermal Engineering*, Vol. 130, pp. 1373–1379, 2018.

37. Kirkley, D., "Determination of the Optimum Configuration for a Stirling Engine", *Mechanical Engineering Science*, Vol. 4, pp. 204–212, 1962.

38. Walker, G., "An Optimization of the Principal Design Parameters of Stirling Cycle Machines", *Mechanical Engineering Science*, Vol. 4, pp. 226–240, 1962.

39. Senft, J., "Extended Mechanical Efficiency Theorems for Engines and Heat Pumps", *Energy Research*, Vol. 24, pp. 679–693, 2000.

40. Senft, J., *Mechanical Efficiency of Heat Engines*, Cambridge University Press, 2007.

41. Cheng, C., H. Yang and L. Keong, "Theoretical and experimental study of a 300-W beta-type Stirling engine", *Energy*, Vol. 59, pp. 590–599, 2013.

42. Cheng, C. and H. Yang, "Optimization of Rhombic Drive Mechanism Used in Beta-type Stirling Engine Based on Dimensionless Analysis", *Energy*, Vol. 64, pp. 970–978, 2014.

43. Wang, K., S. Sanders, S. Dubey, F. Choo and F. Duan, "Stirling Cycle Engines for Recovering Low and Moderate Temperature Heat: A Review", *Renewable and Sustainable Energy Reviews*, Vol. 62, pp. 89–108, 2016.

44. Peterson, H., *The Properties of Helium: Density, Specific Heats, Viscosity, and Thermal Conductivity at Pressures from 1 to 100 bar and from Room Temperature to about 1800 K*, Danish Atomic Energy Commission Research Establishment Rise Engineering Department Section of Experimental Technology, Roskilde, Denmark,

1970.

45. Urieli, I. and D. Berchowitz, *Stirling Cycle Engine Analysis*, Adam Hilger, United Kingdom, 1984.

46. Soylemez, E., *Mechanisms*, METU Publ., Middle East Technical University, 2009.

APPENDIX A: KINEMATIC ANALYSIS

This chapter presents a kinematic analysis of the Beta-type Stirling engine by the vector method [46]. Position, velocity, and acceleration analyses of the mechanism considered are carried out.

A.1. Position Analysis of the Mechanism

For the position of each link of the mechanism, the number of independent parameters, which is equal to the degree of freedom (dof) of the mechanism, must be determined by the general dof equation;

$$DOF = \lambda(\zeta - j - 1) + \sum_{i=1}^{j} f_i \ , \tag{A.1}$$

where λ refers to the dof of space, ζ, and j represent the number of links and joints in the mechanism, respectively, f_i the dof of the i'th joint in the mechanism, and DOF is the dof of the mechanism. It is assumed that the Beta-type engine moves in 2-D space; that is to say, it is a planar mechanism, so λ is considered 3. As shown in Figure A.1, the planar mechanism has 6 links and 7 joints. In addition, there are 5 revolute joints and 2 prismatic joints, each with 1 dof ($f_i = 1$), so the second term in Equation A.1 is equal to 7. By substituting each value, Equation A.1 yields 1.

On the other hand, one can write vector loop equations of the mechanism, which corresponds to L, known as the number of independent loops. L is found to be 2 by using Euler's polyhedron formula [46] below:

$$L = j - \zeta + 1 \ . \tag{A.2}$$

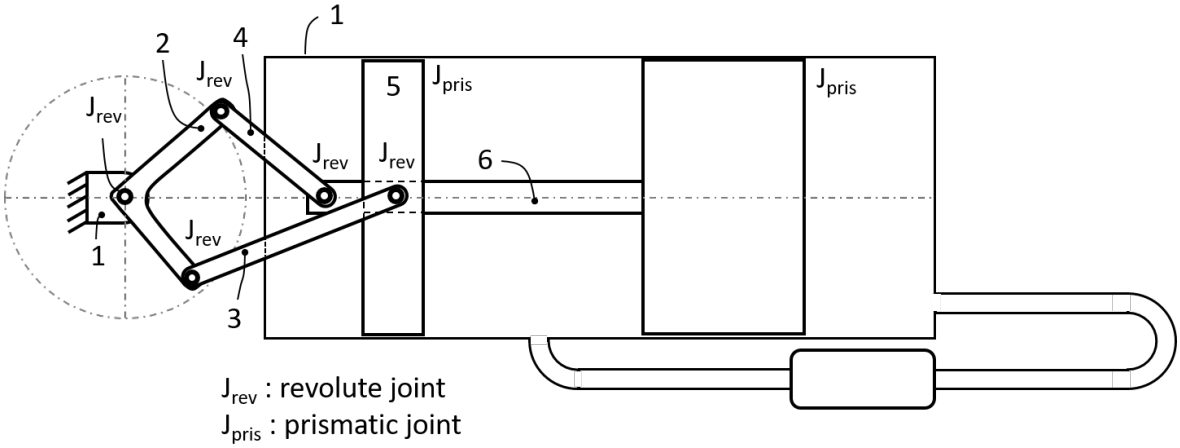


Figure A.1. The links and the joints in the mechanism.

After obtaining DOF and L, there should be $2L + DOF$ parameters to be defined to obtain a kinematically determined mechanism. Then, other unknown position parameters (dependent parameters) can be calculated for each independent parameter. For the planar mechanism considered, $2L + DOF$ is equal to 5. The 5 parameters are θ_p, β_p, β_d, x_{15}, and x_{16} (Figure A.2). Noted that, θ_p and θ_d are dependent to each other, $\theta_d = \theta_p + \Omega$, and Ω refers to the phase angle.

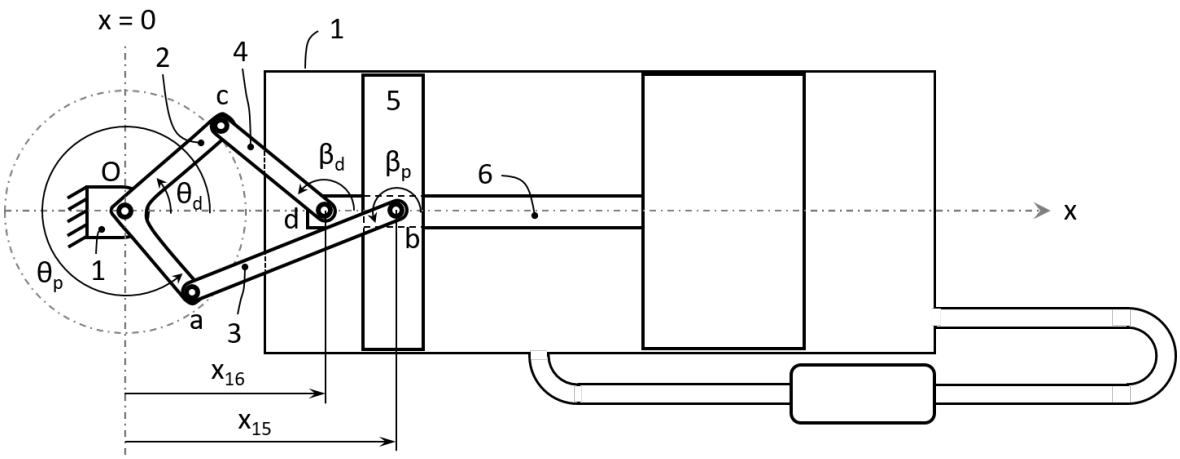


Figure A.2. The position parameters and the vectors in the vector loop equations.

Equations of the two vector loops, shown in Figure A.2 are given as follows;

$$\vec{oa} = \vec{ob} + \vec{ba} \ , \tag{A.3}$$

$$\vec{oc} = \vec{od} + \vec{dc} \ . \tag{A.4}$$

The vector loop equations can be written by using complex numbers;

$$L_{p1} \ e^{i\theta_p} = x_{15} + L_{p2} \ e^{i\beta_p} \ , \tag{A.5}$$

$$L_{d1} \ e^{i\theta_d} = x_{16} + L_{d2} \ e^{i\beta_d} \ , \tag{A.6}$$

where, $L_{p1} =\mid \vec{oa} \mid$, and $L_{p2} =\mid \vec{ba} \mid$, $L_{d1} =\mid \vec{oc} \mid$, $L_{d2} =\mid \vec{dc} \mid$, which are the constant link dimensions. Real and imaginary components (x and y components) of Equation A.5 can be rewritten as follows;

$$L_{p1} \ \cos\theta_p = x_{15} + L_{p2} \ \cos\beta_p \ , \tag{A.7}$$

$$L_{p1} \ \sin\theta_p = L_{p2} \ \sin\beta_p \ . \tag{A.8}$$

The two unknowns in the Equation A.7-A.8, namely β_p and x_{15} for a given θ_p, which are the input joint parameters in the input link 2, are obtained as follows;

$$\beta_p = \arcsin\left(L_{p1}/L_{p2} \ \sin\theta_p\right) \ , \tag{A.9}$$

$$x_{15} = L_{p1} \ \cos\theta_p - L_{p2} \ \cos\beta_p \ . \tag{A.10}$$

In a similar way, real and imaginary components (x and y components) of Equation A.6 can be rewritten as follows;

$$L_{d1}\ \cos\theta_d = x_{16} + L_{d2}\ \cos\beta_d\ , \tag{A.11}$$

$$L_{d1}\ \sin\theta_d = L_{d2}\ \sin\beta_d\ . \tag{A.12}$$

The two unknowns in the Equation A.11-A.12, namely β_d and x_{16} for a given θ_d, are obtained as follows;

$$\beta_d = \arcsin\left(L_{d1}/L_{d2}\ \sin\theta_d\right)\ , \tag{A.13}$$

$$x_{16} = L_{d1}\ \cos\theta_d - L_{d2}\ \cos\beta_d\ . \tag{A.14}$$

The positions of the power and the displacer pistons, x_p and x_d with the help of Figure 5.2 and A.2 can be written as;

$$x_p = x_{15}\ +\ L_p/2\ , \tag{A.15}$$

$$x_d = x_{16}\ +\ L_{d3}\ +\ L_d\ . \tag{A.16}$$

So, the final form of x_p and x_d are obtained as follows, by substituting β_p, β_d, x_{15}, and x_{16} in Equation A.15-A.16, respectively;

$$x_p = L_{p1}\ \cos\theta_p - L_{p2}\ \cos\left(\arcsin\left(L_{p1}/L_{p2}\ \sin\theta_p\right)\right) + L_p/2\ , \tag{A.17}$$

$$x_d = L_{d1}\ \cos\theta_d - L_{d2}\ \cos\left(\arcsin\left(L_{d1}/L_{d2}\ \sin\theta_d\right)\right) + L_{d3} + L_d\ . \tag{A.18}$$

A.2. Velocity Analysis of the Mechanism

The velocity equations are derived from position equations by substituting β_p and β_d in Equation A.10 and A.14 and taking their derivatives with respect to time;

$$\dot{x}_{15} = \frac{\partial x_{15}}{\partial t} = -\ L_{p1}\ \dot{\theta}_p\ \sin\theta_p + L_{p1}^2/L_{p2}\ \sin\theta_p\ \cos\theta_p\ \dot{\theta}_p\ /\ K_p\ , \tag{A.19}$$

$$\dot{x}_{16} = \frac{\partial x_{16}}{\partial t} = -\ L_{d1}\ \dot{\theta}_d\ \sin\theta_d + L_{d1}^2/L_{d2}\ \sin\theta_d\ \cos\theta_d\ \dot{\theta}_d\ /\ K_d\ , \tag{A.20}$$

where $\dot{\theta}_p$ and $\dot{\theta}_d$ are ω_{cr}, $K_p = \sqrt{1-(L_{p1}/L_{p2}\sin\theta_p)^2}$, and $K_d = \sqrt{1-(L_{d1}/L_{d2}\sin\theta_d)^2}$.

The velocities of the power and the displacer pistons, $\dot{x}_p$ and $\dot{x}_d$, are obtained by simplifying Equation A.19-A.20;

$$\dot{x}_p = \dot{x}_{15} = -\ L_{p1}\ \dot{\theta}_p\ \sin\theta_p\ [\ 1 - L_{p1}/L_{p2}\ \cos\theta_p\ /\ K_p\ ]\ , \tag{A.21}$$

$$\dot{x}_d = \dot{x}_{16} = -\ L_{d1}\ \dot{\theta}_d\ \sin\theta_d\ [\ 1 - L_{d1}/L_{d2}\ \cos\theta_d\ /\ K_d\ ]\ . \tag{A.22}$$

A.3. Acceleration Analysis of the Mechanism

The acceleration equations are derived from velocity equations by taking derivatives of Equation A.19-A.20 with respect to time;

$$\begin{aligned}\ddot{x}_{15} = \frac{\partial \dot{x}_{15}}{\partial t} = -\ & L_{p1}\left\{\left(\ddot{\theta}_p\ \sin\theta_p + \dot{\theta}_p^2\ \cos\theta_p\right)\left(\ 1 - \frac{L_{p1}}{L_{p2}}\ \frac{\cos\theta_p}{K_p}\ \right)\right. \\ & \left. +\ \frac{L_{p1}}{L_{p2}}\ \dot{\theta}_p\ \sin\theta_p\ \left(\frac{\dot{\theta}_p\ \sin\theta_p}{K_p} + \frac{\cos\theta_p\ \dot{K}_p}{K_p^2}\right)\right\}\ ,\end{aligned} \tag{A.23}$$

$$\begin{aligned}\ddot{x}_{16} = \frac{\partial \dot{x}_{16}}{\partial t} = -\ & L_{d1}\left\{\left(\ddot{\theta}_d\ \sin\theta_d + \dot{\theta}_d^2\ \cos\theta_d\right)\left(\ 1 - \frac{L_{d1}}{L_{d2}}\ \frac{\cos\theta_d}{K_d}\ \right)\right. \\ & \left. +\ \frac{L_{d1}}{L_{d2}}\ \dot{\theta}_d\ \sin\theta_d\ \left(\frac{\dot{\theta}_d\ \sin\theta_d}{K_d} + \frac{\cos\theta_d\ \dot{K}_d}{K_d^2}\right)\right\}\ ,\end{aligned} \tag{A.24}$$

where, $\dot{K}_p = -\left(L_{p1}/L_{p2}\right)^2\ \sin\theta_p\ \cos\theta_p\ \dot{\theta}_p/K_p$, $\dot{K}_d = -\left(L_{d1}/L_{d2}\right)^2\ \sin\theta_d\ \cos\theta_d\ \dot{\theta}_d/K_d$, $\ddot{\theta}_p$ and $\ddot{\theta}_d$ are α_{cr}.

The accelerations of the power and the displacer pistons, $\ddot{x}_p$ and $\ddot{x}_d$, are obtained by substituting $\dot{K}_p$ and $\dot{K}_d$ and simplifying Equation A.23-A.24;

$$\begin{aligned}\ddot{x}_p = &- L_{p1}\left\{\left(\ddot{\theta}_p \sin\theta_p + \dot{\theta}_p^2 \cos\theta_p\right)\left(1 - \frac{L_{p1}}{L_{p2}}\frac{\cos\theta_p}{K_p}\right)\right. \\ &\left. + \frac{L_{p1}}{L_{p2}}\frac{\left(\dot{\theta}_p \sin\theta_p\right)^2}{K_p}\left[1 - \left(\frac{L_{p1}}{L_{p2}}\frac{\cos\theta_p}{K_p}\right)^2\right]\right\}, \qquad \text{(A.25)} \\ \ddot{x}_d = &- L_{d1}\left\{\left(\ddot{\theta}_d \sin\theta_d + \dot{\theta}_d^2 \cos\theta_d\right)\left(1 - \frac{L_{d1}}{L_{d2}}\frac{\cos\theta_d}{K_d}\right)\right. \\ &\left. + \frac{L_{d1}}{L_{d2}}\frac{\left(\dot{\theta}_d \sin\theta_d\right)^2}{K_d}\left[1 - \left(\frac{L_{d1}}{L_{d2}}\frac{\cos\theta_d}{K_d}\right)^2\right]\right\}. \qquad \text{(A.26)}\end{aligned}$$

APPENDIX B: KINETIC ANALYSIS

In this chapter, the forces acting on the mechanism links are investigated for calculating the applied torque on the crankshaft by the mechanism, shown in Figure A.2. The free-body diagram of the mechanism is shown in Figure B.1. It should be noted that the links' weight and friction are neglected.

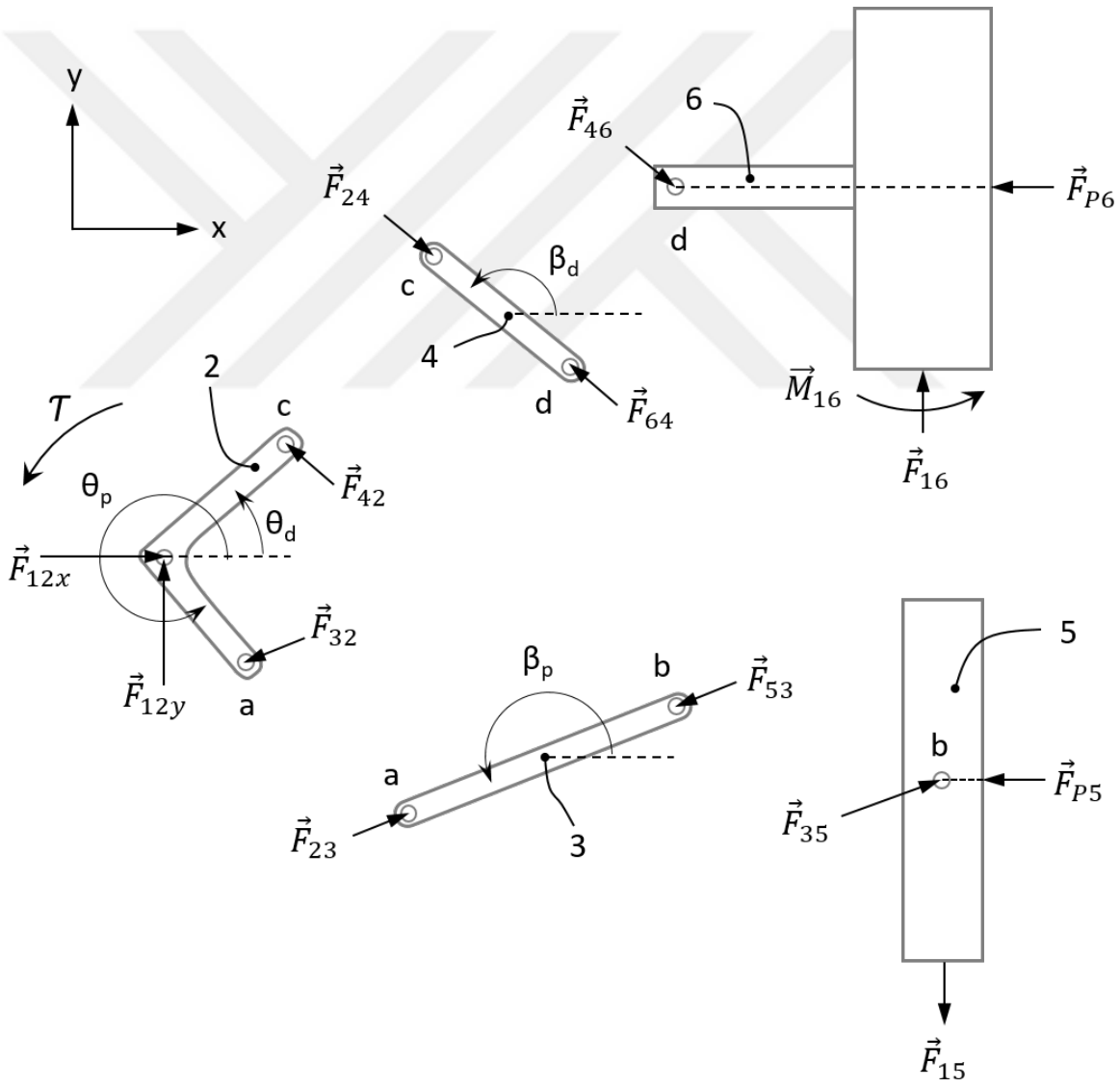


Figure B.1. Free-body diagram of the mechanism.

In Figure B.1, $\vec{F_{P5}}$ and $\vec{F_{P6}}$ are the net forces due to pressure, acting on both sides of the pistons. According to the pressure distribution in Figure 5.4, $\vec{F_{P5}} = (P_{atm} - P_c)$, and $\vec{F_{P6}} = (P_c - P_h)$.

The links 3 and 4 are two-force members, $\vec{F_{23}} = -\vec{F_{53}}$ and $\vec{F_{24}} = -\vec{F_{64}}$. In addition, considering Newton's third law, the following force equalities are obtained;

$$\vec{F_{32}} = -\vec{F_{23}} = \vec{F_{53}} = -\vec{F_{35}} \;\; and \;\; |\,\vec{F_{32}}\,| = |\,\vec{F_{23}}\,| = |\,\vec{F_{53}}\,| = |\,\vec{F_{35}}\,| = F_1\ , \tag{B.1}$$

$$\vec{F_{42}} = -\vec{F_{24}} = \vec{F_{64}} = -\vec{F_{46}} \;\; and \;\; |\,\vec{F_{42}}\,| = |\,\vec{F_{24}}\,| = |\,\vec{F_{64}}\,| = |\,\vec{F_{46}}\,| = F_2\ . \tag{B.2}$$

There are 8 unknowns in free-body diagrams shown in Figure B.1. These are G_{12x}, G_{12y}, F_1, F_2, G_{15}, G_{16}, M_{16}, and $\mathcal{T}$. On the other hand, there are 8 equilibrium equations, which are 3 (2 force, 1 moment) equations for each of links 2 and 6, and 2 force equilibrium equations for link 5.

The forces $\vec{F_{32}}$ and $\vec{F_{42}}$, which create torque on the crankshaft and generate work output, are obtained from $\vec{F_{35}}$ and $\vec{F_{46}}$. The equations for $\vec{F_{35}}$ and $\vec{F_{46}}$ are written using the Newton's second law of motion for the pistons (Figure B.2), as follows;

$$\vec{F_{35}} = (m_p\ddot{x}_p - A(P_{atm} - P_c)) \;/\; \cos(\pi - \beta_p)\ , \tag{B.3}$$

$$\vec{F_{46}} = (m_d\ddot{x}_d - A(P_c - P_h)) \;/\; \cos(\pi - \beta_d)\ . \tag{B.4}$$

The forces $\vec{F_{32}}$ and $\vec{F_{42}}$ are named as $\vec{F_p}$ and $\vec{F_d}$ respectively, and calculated from Equation B.1-B.4 as follows;

$$\vec{F_p} = (m_p\ddot{x}_p - A(P_{atm} - P_c)) \;/\; \cos\beta_p\ , \tag{B.5}$$

$$\vec{F_d} = (m_d\ddot{x}_d - A(P_c - P_h)) \;/\; \cos\beta_d\ . \tag{B.6}$$

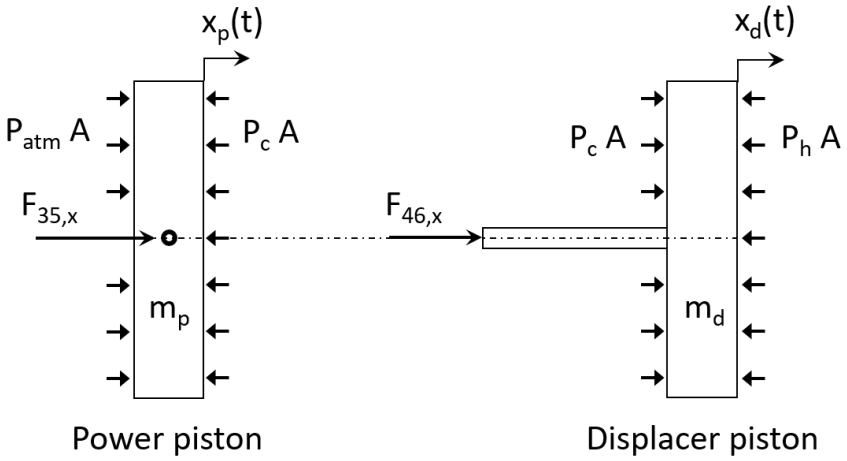


Figure B.2. Forces in x-direction acting on the pistons.

APPENDIX C: GOVERNING EQUATIONS

In this chapter, the ODEs in Figure 5.9 for calculating the work and the power outputs are derived by applying the governing equations in Figure 5.5 to three control volumes of the Stirling engine, shown in Figure 5.1, and two control surfaces between them. The control volumes are;

- The expansion control volume, V_h, consists of the expansion swept, V_{hs}, and dead, V_{hd}, volumes,
- The compression control volume, V_c, consists of the compression swept, V_{cs}, and dead, V_{cd}, volumes,
- The regenerator control volume, V_r.

C.1. Continuity Equation

The continuity equation in Figure 5.6 is applied to the three control volumes for obtaining the temperature functions.

C.1.1. Expansion Volume

The expansion volume is a fixed and deforming control volume. The time rate of mass in the swept and the dead expansion volumes equals the net mass flow rate through the control surface between the dead expansion and the regenerator volumes, as given in the following equations;

$$A \frac{\partial}{\partial t} (\rho_h \, x_h) - N_h \, \phi_h^2 \, A \, \rho_{hf} \, u_f = 0 \, , \tag{C.1}$$

$$\dot{\rho}_h \left(L_{hs} + N_h \, \phi_h^2 \, 2L_{hd} \right) + \rho_h \, \dot{L}_{hs} - N_h \, \phi_h^2 \, \rho_{hf} \, u_f = 0 \, . \tag{C.2}$$

By substituting PT/R for ρ from the ideal gas equation and simplifying, one gets;

$$\frac{\left(\dot{P}_h\, T_h - P_h\, \dot{T}_h\right)}{R\, T_h^2}\left(L_{hs} + N_h\, \phi_h^2\, 2L_{hd}\right) + \frac{P_h}{R\, T_h}\dot{L}_{hs} - N_h\, \phi_h^2\, \frac{P_{hf}}{R\, T_{hf}}\, u_f = 0\ , \quad \text{(C.3)}$$

$$\left(\dot{P}_h\, T_h - P_h\, \dot{T}_h\right)\left(L_{hs} + N_h\, \phi_h^2\, 2L_{hd}\right) + P_h\, T_h\, \dot{L}_{hs} - N_h\, \phi_h^2\, P_{hf}\, \frac{T_h^2}{T_{hf}}\, u_f = 0\ . \quad \text{(C.4)}$$

From Equation C.4, $\dot{T}_h$ is derived as;

$$\dot{T}_h(t) = \frac{\dot{P}_h\, T_h}{P_h} + \frac{\dot{L}_{hs}\, T_h}{L_{hs} + N_h\, \phi_h^2\ \ 2L_{hd}} - \frac{P_{hf}}{P_h}\ \frac{T_h^2}{T_{hf}}\ \frac{N_h\, \phi_h^2\, u_f}{L_{hs} + N_h\, \phi_h^2\ \ 2L_{hd}}\ . \quad \text{(C.5)}$$

C.1.2. Compression Volume

The compression volume is a moving and deforming control volume. The time rate of mass in the swept and the dead compression volumes equals the net mass flow rate through the control surface between the dead compression and the regenerator volumes, as given in the following equations;

$$A\, \frac{\partial}{\partial t}\left(\rho_c\, x_c\right) + N_c\, \phi_c^2\, A\, \rho_{cf}\, u_f = 0\ , \quad \text{(C.6)}$$

$$\dot{\rho}_c\left(L_{cs} + N_c\, \phi_c^2\, L_{cd}\right) + \rho_c\, \dot{L}_{cs} + N_c\, \phi_c^2\, \rho_{cf}\, u_f = 0\ . \quad \text{(C.7)}$$

By substituting PT/R for ρ from the ideal gas equation and simplifying, one gets;

$$\frac{\left(\dot{P}_c\, T_c - P_c\, \dot{T}_c\right)}{R\, T_c^2}\left(L_{cs} + N_c\, \phi_c^2\, L_{cd}\right) + \frac{P_c}{R\, T_c}\dot{L}_{cs} + N_c\, \phi_c^2\, \frac{P_{cf}}{R\, T_{cf}} u_f = 0\ , \quad \text{(C.8)}$$

$$\left(\dot{P}_c\, T_c - P_c\, \dot{T}_c\right)\left(L_{cs} + N_c\, \phi_c^2\, L_{cd}\right) + P_c\, T_c\, \dot{L}_{cs} + N_c\, \phi_c^2\, P_{cf}\, \frac{T_c^2}{T_{cf}}\, u_f = 0\ . \quad \text{(C.9)}$$

From Equation C.9, $\dot{T}_c$ is derived as;

$$\dot{T}_c(t) = \frac{\dot{P}_c\, T_c}{P_c} + \frac{\dot{L}_{cs}\, T_c}{L_{cs} + N_c\, \phi_c^2\, L_{cd}} + \frac{P_{cf}}{P_c}\, \frac{T_c^2}{T_{cf}}\, \frac{N_c\, \phi_c^2\, u_f}{L_{cs} + N_c\, \phi_c^2\, L_{cd}} \,. \tag{C.10}$$

C.1.3. Regenerator Volume

The regenerator volume is a fixed and non-deforming control volume. The time rate of mass in the regenerator volume equals the net mass flow rate through the control surfaces between the dead expansion, the dead compression, and the regenerator volumes, as given in the following equations;

$$N_h\, \phi_h^2\, A\, \frac{\partial}{\partial t}\left(\rho_r\, L_{reg}\right) - N_c\, \phi_c^2\, A\, \rho_{cf}\, u_f + N_h\, \phi_h^2\, A\, \rho_{hf}\, u_f = 0 \,, \tag{C.11}$$

$$N_h\, \phi_h^2\, \dot{\rho}_r\, L_{reg} + u_f \left(-N_c\, \phi_c^2\, \rho_{cf} + N_h\, \phi_h^2\, \rho_{hf}\right) = 0 \,. \tag{C.12}$$

By substituting PT/R for ρ from the ideal gas equation and simplifying, one gets;

$$N_h\, \phi_h^2\, \frac{\left(\dot{P}_r\, T_r - P_r\, \dot{T}_r\right)}{T_r^2}\, L_{reg} + u_f \left(-N_c\, \phi_c^2\, \frac{P_{cf}}{T_{cf}} + N_h\, \phi_h^2\, \frac{P_{hf}}{T_{hf}}\right) = 0 \,, \tag{C.13}$$

$$N_h\, \phi_h^2 \left(\dot{P}_r\, T_r - P_r\, \dot{T}_r\right) L_{reg} + u_f\, T_r^2 \left(-N_c\, \phi_c^2\, \frac{P_{cf}}{T_{cf}} + N_h\, \phi_h^2\, \frac{P_{hf}}{T_{hf}}\right) = 0 \,. \tag{C.14}$$

From Equation C.14, $\dot{T}_r$ is derived as;

$$\dot{T}_r(t) = \frac{T_r}{P_r}\left[\dot{P}_r + \frac{u_f\, T_r}{L_{reg}} \left(-\frac{N_c\, \phi_c^2}{N_h\, \phi_h^2}\, \frac{P_{cf}}{T_{cf}} + \frac{P_{hf}}{T_{hf}}\right)\right] \,. \tag{C.15}$$

C.2. Momentum Equation

The momentum equation in Figure 5.7 is applied to the regenerator control volume for obtaining the flow velocity function.

C.2.1. Regenerator Volume

The sum of the forces acting on the fluid in the regenerator volume is written as;

$$\sum F_x = N_h\ \phi_h^2\ A\ \frac{\partial}{\partial t}\left(\rho_r\ u_f\ L_{reg}\right) - N_c\ \phi_c^2\ A\ \rho_{cf}\ u_f^2 + N_h\ \phi_h^2\ A\ \rho_{hf}\ u_f^2\ , \tag{C.16}$$

$$\frac{\sum F_x}{N_h\ \phi_h^2\ A} = \frac{\left(\dot{P}_r\ T_r - P_r\ \dot{T}_r\right)}{R\ T_r^2}\ u_f\ L_{reg} + \frac{P_r}{R\ T_r}\ \dot{u}_f\ L_{reg} - \frac{N_c\ \phi_c^2}{N_h\ \phi_h^2}\ \frac{P_{cf}}{R\ T_{cf}} u_f^2 + \frac{P_{hf}}{R\ T_{hf}}\ u_f^2\ , \tag{C.17}$$

$$\sum F_x = N_h\ \phi_h^2\ A\ \left(P_c - P_h\right)\ . \tag{C.18}$$

By equating Equation C.17-C.18 and simplifying, following equation is obtained;

$$R\ T_r^2\left(P_c - P_h\right) = \left(\dot{P}_r\ T_r - P_r\ \dot{T}_r\right) u_f\ L_{reg} + P_r\ T_r\ \dot{u}_f\ L_{reg} + T_r^2\ u_f^2\left(-\frac{N_c\ \phi_c^2}{N_h\ \phi_h^2}\ \frac{P_{cf}}{T_{cf}} + \frac{P_{hf}}{T_{hf}}\right)\ . \tag{C.19}$$

From Equation C.19, $\dot{u}_f$ is derived as;

$$\dot{u}_f(t) = \frac{1}{L_{reg}}\ \frac{T_r}{P_r}\left[R\left(P_c - P_h\right) + u_f^2\left(\frac{N_c\ \phi_c^2}{N_h\ \phi_h^2}\ \frac{P_{cf}}{T_{cf}} - \frac{P_{hf}}{T_{hf}}\right)\right] - u_f\left(\frac{\dot{P}_r}{P_r} - \frac{\dot{T}_r}{T_r}\right). \tag{C.20}$$

C.3. Energy Equation

The energy equation in Figure 5.8 is applied to the three control volumes for obtaining the pressure functions.

C.3.1. Expansion Volume

The energy balance for the expansion volume is written as below, in terms of the time rate of internal energy of the working fluid in the swept and dead volumes, and heat added and work done;

$$A \frac{\partial}{\partial t}\left(e_h \, \rho_h \, x_h\right) - N_h \, \phi_h^2 \, A \, h_{hf} \, \rho_{hf} \, u_f = \dot{Q}_h - \dot{W}_h \, , \tag{C.21}$$

where, $e_h = c_V \, T_h$, and $h_{hf} = c_P \, T_{hf}$. The heat and work rates are given below;

$$\dot{Q}_h = A \, h_{cv} \, \left(T_d - T_h\right) + N_h \, 4A \, \frac{\phi_h}{\phi_{cyl}} \, 2\varphi_{hd} \, U_h \left(T_{sh} - T_h\right) \, , \tag{C.22}$$

$$\dot{W}_h = A \, P_h \, \dot{L}_{hs} \, . \tag{C.23}$$

The energy balance equation is rewritten by substituting e_h, h_{hf}, $\dot{Q}_h$, and $\dot{W}_h$ in Equation C.21, as below;

$$\begin{aligned} A \, c_V \, \frac{\partial}{\partial t}\left(\rho_h \, T_h \, x_h\right) - N_h \, \phi_h^2 \, A \, c_P \, T_{hf} \, \rho_{hf} \, u_f = \\ A \left[h_{cv} \left(T_d - T_h\right) + N_h \, 8 \frac{\phi_h}{\phi_{cyl}} \, \varphi_{hd} \, U_h \left(T_{sh} - T_h\right) \right] - A \, P_h \, \dot{L}_{hs} \, . \end{aligned} \tag{C.24}$$

By substituting PT/R for ρ from the ideal gas equation and simplifying, one gets;

$$\frac{c_V}{R}\,\frac{\partial}{\partial t}\left(P_h\left(L_{hs}+N_h\,\phi_h^2\,2L_{hd}\right)\right)-N_h\,\phi_h^2\,\frac{c_P}{R}\,u_f\,P_{hf}= h_{cv}\,(T_d-T_h)+N_h\,8\frac{\phi_h}{\phi_{cyl}}\,\varphi_{hd}\,U_h\,(T_{sh}-T_h)-P_h\,\dot{L}_{hs}\,, \tag{C.25}$$

$$\frac{c_V}{R}\left(\dot{P}_h\left(L_{hs}+N_h\,\phi_h^2\,2L_{hd}\right)+P_h\,\dot{L}_{hs}\right)-N_h\,\phi_h^2\,\frac{c_P}{R}\,P_{hf}\,u_f= h_{cv}\,(T_d-T_h)+N_h\,8\frac{\phi_h}{\phi_{cyl}}\,\varphi_{hd}\,U_h\,(T_{sh}-T_h)-P_h\,\dot{L}_{hs}\,, \tag{C.26}$$

$$c_V\,\dot{P}_h\left(L_{hs}+N_h\,\phi_h^2\,2L_{hd}\right)+(c_V+R)\,P_h\,\dot{L}_{hs}-N_h\,\phi_h^2\,c_P\,P_{hf}\,u_f= R\left[h_{cv}\,(T_d-T_h)+N_h\,8\frac{\phi_h}{\phi_{cyl}}\,\varphi_{hd}\,U_h\,(T_{sh}-T_h)\right]. \tag{C.27}$$

The equation for the pressure rate, $\dot{P}_h$, is obtained as follows;

$$\dot{P}_h(t)=[R\,h_{cv}(T_d-T_h)+8R\,N_h\,\phi_h\,\varphi_{hd}\,U_h\,(T_{sh}-T_h)\,/\,\phi_{cyl} - c_P\,(P_h\,\dot{L}_{hs}-N_h\,\phi_h^2\,P_{hf}\,u_f)]\,/\,[c_V(L_{hs}+N_h\,\phi_h^2\,2L_{hd})]\,. \tag{C.28}$$

C.3.2. Compression Volume

The energy balance for the compression volume is written as below, in terms of the time rate of internal energy of the working fluid in the swept and dead volumes, and heat added and work done;

$$A\,\frac{\partial}{\partial t}\,(e_c\,\rho_c\,x_c)+N_c\,\phi_c^2\,A\,h_{cf}\,\rho_{cf}\,u_f=\dot{Q}_c-\dot{W}_c\,, \tag{C.29}$$

where, $e_c=c_V\,T_c$, and $h_{cf}=c_P\,T_{cf}$. The heat and work rates are given as below;

$$\dot{Q}_c=A\,h_{cv}\,[(T_d-T_c)+(T_p-T_c)]+N_c\,4A\,\frac{\phi_c}{\phi_{cyl}}\,\varphi_{cd}\,U_c\,(T_{sc}-T_c)\,, \tag{C.30}$$

$$\dot{W}_c=A\,P_c\,\dot{L}_{cs}\,. \tag{C.31}$$

The energy balance equation is rewritten by substituting e_c, h_{cf}, $\dot{Q}_c$, and $\dot{W}_c$ in Equation C.29, as below;

$$A\, c_V\, \frac{\partial}{\partial t}\left(\rho_c\, T_c\, x_c\right) + N_c\, \phi_c^2\, A\, c_P\, T_{cf}\, \rho_{cf}\, u_f = A\left[h_{cv}\left(T_d + T_p - 2T_c\right) + C\, 4\frac{\phi_c}{\phi_{cyl}}\, \varphi_{cd}\, U_c\left(T_{sc} - T_c\right)\right] - A\, P_c\, \dot{L}_{cs}\,. \tag{C.32}$$

By substituting PT/R for ρ from the ideal gas equation and simplifying, one gets;

$$\frac{c_V}{R}\, \frac{\partial}{\partial t}\left(P_c\left(L_{cs} + N_c\, \phi_c^2\, L_{cd}\right)\right) + N_c\, \phi_c^2\, \frac{c_P}{R}\, u_f\, P_{cf} = h_{cv}\left(T_d + T_p - 2T_c\right) + N_c\, 4\frac{\phi_c}{\phi_{cyl}}\, \varphi_{cd}\, U_c\left(T_{sc} - T_c\right) - P_c\, \dot{L}_{cs}\,, \tag{C.33}$$

$$\frac{c_V}{R}\left(\dot{P}_c\left(L_{cs} + N_c\, \phi_c^2\, L_{cd}\right) + P_c\, \dot{L}_{cs}\right) + N_c\, \phi_c^2\, \frac{c_P}{R} P_{cf}\, u_f = h_{cv}\left(T_d + T_p - 2T_c\right) + N_c\, 4\frac{\phi_c}{\phi_{cyl}}\, \varphi_{cd}\, U_c\left(T_{sc} - T_c\right) - P_c\, \dot{L}_{cs}\,, \tag{C.34}$$

$$c_V\, \dot{P}_c\left(L_{cs} + N_c\, \phi_c^2\, L_{cd}\right) + \left(c_V + R\right) P_c\, \dot{L}_{cs} + N_c\, \phi_c^2\, c_P\, P_{cf}\, u_f = R\left[h_{cv}\left(T_d + T_p - 2T_c\right) + N_c\, 4\frac{\phi_c}{\phi_{cyl}}\, \varphi_{cd}\, U_c\left(T_{sc} - T_c\right)\right]. \tag{C.35}$$

The equation for the pressure rate, $\dot{P}_c$, is obtained as follows;

$$\dot{P}_c(t) = \left[R\, h_{cv}(T_d + T_p - 2T_c) + 4R\, N_c\, \phi_c\, \varphi_{cd}\, U_c\, (T_{sc} - T_c)\, /\, \phi_{cyl} - c_P\, (P_c\, \dot{L}_{cs} + N_c\, \phi_c^2\, P_{cf}\, u_f)\right] /\, \left[c_V\, (L_{cs} + N_c\, \phi_c^2\, L_{cd})\right]. \tag{C.36}$$

C.3.3. Regenerator Volume

The energy balance for the regenerator volume is written below in terms of the time rate of internal energy of the working fluid, heat added, and work done;

$$N_h\ \phi_h^2\ A\ \frac{\partial}{\partial t}\left(e_r\ \rho_r\ L_{reg}\right) - N_c\ \phi_c^2\ A\ h_{cf}\ \rho_{cf}\ u_f + N_h\ \phi_h^2\ A\ h_{hf}\ \rho_{hf}\ u_f = \dot{Q}_r - \dot{W}_r\ , \tag{C.37}$$

where, $e_r = c_V\ T_r$, $h_{cf} = c_P\ T_{cf}$, and $h_{hf} = c_P\ T_{hf}$. As the regenerator volume is non-deforming, the work rate, $\dot{W}_r$, is zero. The heat rate is given below;

$$\dot{Q}_r = N_h\ 4A\ \frac{\phi_h}{\phi_{cyl}}\ \varphi_{reg}\ h_{cv}\left(T_{reg} - T_r\right)\ . \tag{C.38}$$

The energy balance equation is rewritten by substituting e_h, h_{cf}, h_{hf}, $\dot{Q}_r$, and $\dot{W}_r$ in Equation C.37;

$$N_h\ \phi_h^2\ A\left[c_V\ \frac{\partial}{\partial t}\left(\rho_r\ T_r\ L_{reg}\right) - \frac{N_c\ \phi_c^2}{N_h\ \phi_h^2}\ c_P\ T_{cf}\ \rho_{cf}\ u_f + c_P\ T_{hf}\ \rho_{hf}\ u_f\right] = N_h\ 4A\ \frac{\phi_h}{\phi_{cyl}}\ \varphi_{reg}\ h_{cv}\left(T_{reg} - T_r\right)\ . \tag{C.39}$$

By substituting PT/R for ρ from the ideal gas equation and simplifying, one gets;

$$\frac{c_V}{R}\ \frac{\partial}{\partial t}\left(P_r\ L_{reg}\right) - \frac{N_c\ \phi_c^2}{N_h\ \phi_h^2}\ \frac{c_P}{R}\ P_{cf} u_f + \frac{c_P}{R}\ P_{hf}\ u_f = 4\ \frac{\varphi_{reg}}{\phi_{cyl}\ \phi_h}\ h_{cv}\left(T_{reg} - T_r\right)\ , \tag{C.40}$$

$$c_V\ \dot{P}_r\ L_{reg} + c_P\ u_f\left(-\frac{N_c\ \phi_c^2}{N_h\ \phi_h^2}\ P_{cf} + P_{hf}\right) = 4\ \frac{\varphi_{reg}}{\phi_{cyl}\ \phi_h}\ h_{cv}\left(T_{reg} - T_r\right)\ . \tag{C.41}$$

The equation for the pressure rate, $\dot{P}_r$, is obtained as follows;

$$\dot{P}_r(t) = \frac{4\ R\ \varphi_{reg}}{c_V\ L_{reg}\ \phi_{cyl}\ \phi_h}\ h_{cv}\left(T_{reg} - T_r\right) + \frac{c_P\ u_f}{c_V\ L_{reg}}\left(\frac{N_c\ \phi_c^2}{N_h\ \phi_h^2}\ P_{cf} - P_{hf}\right)\ . \tag{C.42}$$